Fakultät Mathematik und Naturwissenschaften
Technische Universität Dresden
Leibniz-Institut für Festkörper- und Werkstoffforschung

Metallic Ground State of Functionalized Carbon Nanotubes

Dissertation
zur Erlangung des akademischen Grades
Doctor rerum naturalium

vorgelegt von
Hendrik Rauf
geboren am 03. September 1975 in Osnabrück

Dresden 2007

Eingereicht am 22. Dezember 2006

1. Gutachter: Prof. Dr. B. Büchner

2. Gutachter: ______________________________

3. Gutachter: ______________________________

Verteidigt am ___________________

Contents

1 Motivation

Carbon nanostructures

Carbon is presumably the most diverse and important element in the periodic table. The carbon atom has a high affinity to bond with other atoms. Together with its small size, which enables the formation of multiple bonds, this leads to a great variety of compounds which can be formed. And indeed, with over ten million known compounds, carbon appears in the vast majority of all chemical compounds, granting carbon an important standing in biology and organic chemistry and, of course, physics. Carbon is the sixth element of the periodic table with the electronic configuration $1s^2\,2s^2\,2p^2$. Even when only bonding with other carbon atoms, a great number of compounds is possible. Fig. 1.1 depicts some examples of carbon allotropes. The electronic configuration gives rise to three possible hybridizations of the atomic orbitals of carbon: sp hybridization is found eg. in acetylene, graphite is the most common example for sp^2 hybridization, and sp^3 bonding is responsible for the extraordinary hardness of diamond. The materials formed can be either insulating (diamond), semiconducting (fullerenes and nanotubes), semimetallic (graphite), or metallic (nanotubes). The sp^2 bonding configuration is of particular interest because of its combination of strong and stiff σ bonds which covalently couple the carbon atoms and the π orbitals which are directed perpendicular to the σ bond network and determine the electronic properties of the compound.

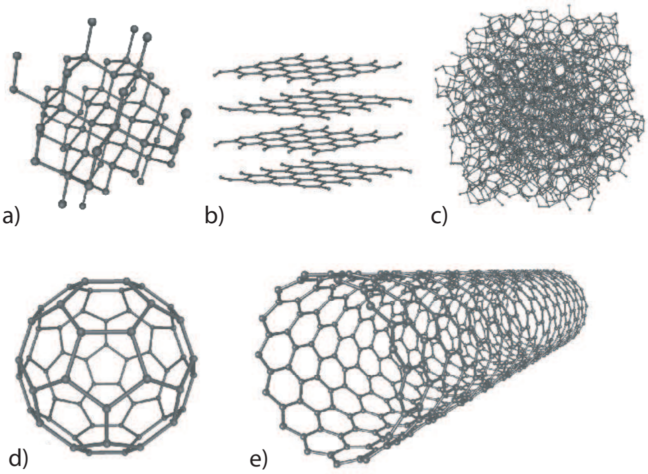

Figure 1.1: Different allotropes of carbon. a) Diamond b) Graphite c) Amorphous graphite d) C_{60} e) SWCNT

The discovery of fullerenes in 1985 established a new family of sp^2 bonded allotropes [1] and earned Robert F. Curl jr., Harold W. Kroto and Richard E. Smalley the Nobel prize in chemistry in 1992 for their role in the discovery of these highly symmetric carbon molecules [2]. In 1991, a new member of this family of carbon nanostructures appeared on the landscape. Iijima observed tubular structures in high-resolution TEM and identified them as multi-wall carbon nanotubes (MWCNTs) [3]. Shortly after that, the successful synthesis of single-wall carbon nanotubes (SWCNT) was reported [4, 5]. In contrast to MWCNTs, SWCNTs consist of only one carbon shell, making them remarkable one-dimensional objects.

Carbon nanotubes exhibit outstanding characteristics. In terms of mechanical properties they are among the strongest and most resilient materials known to exist. MWCNTs as well as SWCNTs exhibit an unrivalled high elastic modulus at very low weight. They are predicted to be the strongest fibers that can be made [6]. Their tensile strength is about a hundred times higher than that of steel, yet they are very flexible. The electronic properties of SWCNTs are highly dependent on their structure. Depending on their chirality they can be either metallic or semiconducting [7, 8]. These properties have sparked a great interest in the application of nanotubes. First large scale applications use MWCNTs to increase the strength and modulus of composite materials and for improving the lifetime and performance of lithium-ion batteries. In addition, the possibility of contacting individual nanotubes [9] enables their application in microtechnology as transistors or metallic interconnects [10]. The transport properties of semiconducting SWCNTs surpass those of silicon in terms of current density and charge carrier mobility [11]. Individual field effect transistors perform remarkably well [12] and device functions (AND and NOR gates, etc.) have been fabricated [13]. Furthermore, nanotubes have been proven suitable as light-emitting diodes for displays [14] and can be used as sensors on a microscopic scale. Among the challenges which have to be overcome to ensure a wider range of applications are the controlled synthesis of defined chiralities, the separation of individual nanotubes with defined properties and an efficient controlled spatial deposition and ordering of tubes [15].

Carbon nanotubes are also of great interest from the perspective of fundamental research. Because of their particular structure SWCNTs are thought of as perfect one-dimensional systems and, as such, exhibit peculiar electronic properties. This was demonstrated eg. by the existence of so-called van-Hove singularities (vHs) which are a fingerprint of one-dimensional systems. They determine the optical properties of SWCNTs and lead to resonance effects which motivated extensive studies using optical absorption spectroscopy, Raman spectroscopy and photoluminescence spectroscopy [16, 17]. Furthermore, the ballistic transport of one-dimensional systems with a conductivity $G = 2e^2/h$, i.e. independent of length and scattering, is predicted [18] and observed over a length scale of several microns [19].

On the other hand, correlation effects also play an important role in SWCNTs. This was demonstrated e.g. through the Coulomb blockade in transport experiments [20]. In addition, the existence of excitons in SWCNTs was recently proven experimentally [21, 22]. The extraordinary high exciton binding energy which was found is an indication of a significant interaction between charge carriers. Correlation effects also greatly influence the metallic ground state of materials. In classical three-dimensional metals electron-electron interaction mainly leads to a renormalization of the charge carrier properties (eg. effective mass), as described in Landau's Fermi liquid theory. One-dimensional metals are influenced to a greater extent by interactions. In fact, the Landau-quasiparticle picture breaks down due to the Peierls instability. Instead, one-dimensional metals are described by Tomonaga-Luttinger liquid (TLL) theory which predicts unusual properties such as spin-charge separation and non-universal power laws in some physical properties such as the electronic density of states. Such a behavior is also predicted for SWCNTs and indeed, transport experiments could be interpreted in terms of tunneling into or between TLL [23–26]. However, in the interpretation of these experiments uncertainties remained due to the contacting and the small energy scale. In this regard, photoemission spectroscopy appears to be a useful tool to resolve these uncertainties.

Aim of this thesis

In this thesis the metallic ground state of one-dimensional and three-dimensional systems and the transition between these dimensionalities is studied. Metallic SWCNTs represent a paradigm of a one-dimensional metal. In realistic systems they are embedded in a three-dimensional structure: SWCNTs tend to form bundles. This makes them an interesting and promising subject for such studies. SWCNTs will be studied in the pristine state and upon functionalization with doping, filling with C_{60} molecules and a combination of these two. In particular, it will be investigated how a controlled modification of the SWCNTs influences the one-dimensional character of the system.

In the pristine state the Tomonaga-Luttinger liquid behavior of SWCNTs will be investigated by photoemission spectroscopy. This method promises to overcome the limitations concerning energy scale and contacting of previous transport experiments which dealt with this topic. It will be shown that SWCNTs are indeed one-dimensional objects from the electronic point of view, although they are embedded in the three-dimensional bundle structure.

Using chemical doping, the electronic structure of the system can be manipulated and the character of the SWCNTs can be changed by rendering the semiconducting tubes metallic. The influence of this process on the dimensionality of the system will be investigated and the results will be discussed in terms of a transition from a Tomonaga-Luttinger liquid to a Fermi liquid.

Further interesting topics arise if the band structure is modified by introducing new electronic states into the system. This is carried out by filling the SWCNTs with C_{60} molecules. In these so-called C_{60} peapods, the molecular orbitals derived from C_{60} add new components to the electronic system. This is especially interesting since the quantitative manifestation of TLL behavior depends on the number of conduction channels in the system. The role of the additional bands can be studied in more detail by also doping the C_{60} peapods. The transition from a Tomonaga-Luttinger liquid to a Fermi liquid is discussed with regard to the role of the contribution of the C_{60} filling.

In order to present a complete and conclusive picture, Chapter 2 will give an introduction into the field of carbon nanotubes with emphasis on the electronic properties. The experimental methods will be presented in Chapter 3, followed by an introduction to the metallic ground states of one- and three-dimensional systems and their distinctly different properties in Chapter 4. Chapter 5 is devoted to the electronic properties of pristine SWCNTs as they are obtained from photoemission spectroscopy. In Chapter 6, a detailed doping experiment will be carried out and discussed regarding the influence on the dimensionality of the SWCNT bundle. The investigation of the influence of the C_{60} filling on the metallic ground state of C_{60} peapods is presented in Chapter 7, a doping series similar to that in Chapter 6 is carried out. Finally, the results of this thesis are summarized in Chapter 8.

2 Carbon nanotubes

In many solid state materials, the electronic properties are closely related to their geometric structure. Nevertheless single-wall carbon nanotubes (SWCNT) form a special species in this regard. Although SWCNTs can always be envisaged as a rolled-up graphene sheet, the possible varying rolling directions of this sheet lead to different fundamental electronic properties. The aim of this chapter is to discuss the structural and electronic properties of carbon nanotubes with special regard to their interplay. In the last section of this chapter, the different ways of modifying the electronic and structural properties of SWCNTs by functionalization will be discussed.

2.1 Graphite and Graphene

A graphite crystal is formed by a layered hexagonal lattice of carbon (C) atoms. The two-dimensional layers are called graphene or two-dimensional graphite. Graphene can be regarded as a starting point for both, the structure and the electronic properties of carbon nanotubes. Its properties can be approximated well by those of graphite since the inter-layer spacing of 3.35 Å is much larger than the in-plane C-C bond length and thus the inter-plane interaction is weak.

The origin of the hexagonal structure is the C-C bond configuration as it results from the hybridization of the valence band electrons. In carbon, these valence band electrons are the two $2s$ and two $2p$ orbitals[1] which can mix in different ways. The type of hybridization determines the bonding configuration in the large family of carbon structures. Diamond is an example of sp^3 hybridization and is characterized by four σ bonds per carbon atom in a three-dimensional arrangement. In graphite – and consequently carbon nanotubes as well – sp^2 hybridization is present, i.e. two p-orbitals hybridize with one s-orbital . This results in three strong covalent σ-bonds per carbon atom which lie in a plane and form angles of 120° between them and π orbitals perpendicular to this plane. Fig. 2.1 depicts a graphene sheet of this kind. With respect to the basis shown in the figure, the directions of the primitive vectors of the honeycomb lattice $\vec{a_1}$ and $\vec{a_2}$ can be expressed as

$$\vec{a_1} = (\sqrt{3}a/2, a/2) \qquad\qquad \vec{a_2} = (\sqrt{3}a/2, -a/2). \tag{2.1}$$

The graphene honeycomb lattice – as opposed to the hexagonal lattice – is not a Bravais lattice, its unit cells contain two carbon atoms at non-equivalent positions.

The electronic structure of graphene can be obtained in a simple nearest-neighbor tight-binding model. The energy dispersion – in this case for the π bands – is given as a function of the transfer integral γ_0 and the overlap integral s [27]:

---

[1] The two $1s$ electrons form the so-called core level states and are strongly localized.

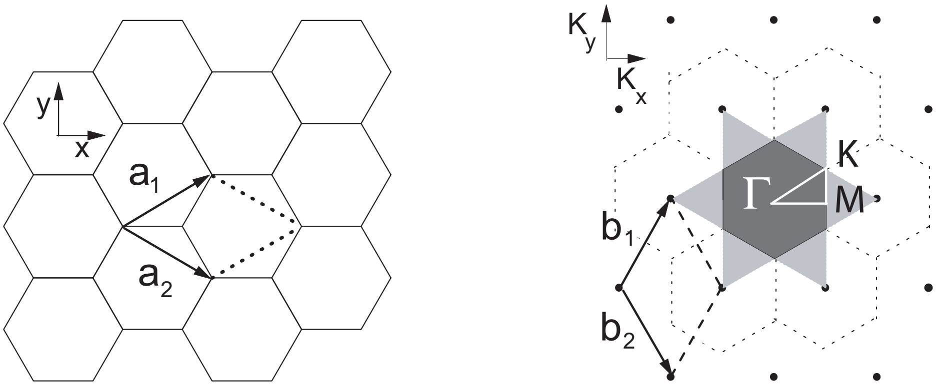

Figure 2.1: Left panel: Hexagonal lattice of a graphene sheet. The unit cell defined by $\mathbf{a_1}$ and $\mathbf{a_2}$ is marked. **Right panel:** Reciprocal lattice (dashed) with lattice vectors $\mathbf{b_1}$ and $\mathbf{b_2}$ corresponding to the real lattice defined by $\mathbf{a_1}$ and $\mathbf{a_2}$. The first Brillouin zone is indicated in dark gray, the second in light gray. The high symmetry points ΓKM are indicated by the white triangle.

$$E^{\pm}_{g2D}(k) = \frac{\epsilon_{2p} \pm \gamma_0 \omega(k)}{1 \mp s\omega(k)} \ , \tag{2.2}$$

where ϵ_{2p} is the orbital energy of the $2p$ level. The ± signs correspond to the bonding and anti-bonding bands. The function ω is given by [27]:

$$\omega(k) = \sqrt{1 + 4\cos\left(\frac{\sqrt{3}k_x a}{2}\right)\cos\left(\frac{k_y a}{2}\right) + 4\cos^2\left(\frac{k_y a}{2}\right)}, \tag{2.3}$$

where k_x and k_y are the components of the $\vec{k}$-vector. In a first approximation, only the π and $\pi^\star$ bands are considered. The Slater-Koster scheme where the overlap integral s between two neighboring atoms is neglected is used. In this case the resulting energy dispersion is given by

$$E_{g2D}(k_x, k_y) = \pm\gamma_0 \sqrt{1 + 4\cos\left(\frac{3k_x a}{2}\right)\cos\left(\frac{\sqrt{3}k_y a}{2}\right) + 4\cos^2\left(\frac{\sqrt{3}k_y a}{2}\right)} \ . \tag{2.4}$$

In the right panel of Fig. 2.2, this dispersion is plotted for $s = 0$ (dashed line) and $s = 0.129$ (solid line) along the directions of high symmetry. The left panel depicts the dispersion of the π and $\pi^\star$ bands over the whole Brillouin zone. One important point is that the valence band and the conduction band touch at the K point. However, the density of states at the Fermi level is zero. Graphene is thus called a zero-gap semiconductor.

2.2 Geometric structure of single-wall carbon nanotubes

2.2.1 Real space description

The nanotube structure is obtained by rolling up a defined section of a graphene sheet. Such a setting is depicted in Fig. 2.3. In the following some definitions concerning the geometric structure will be given.

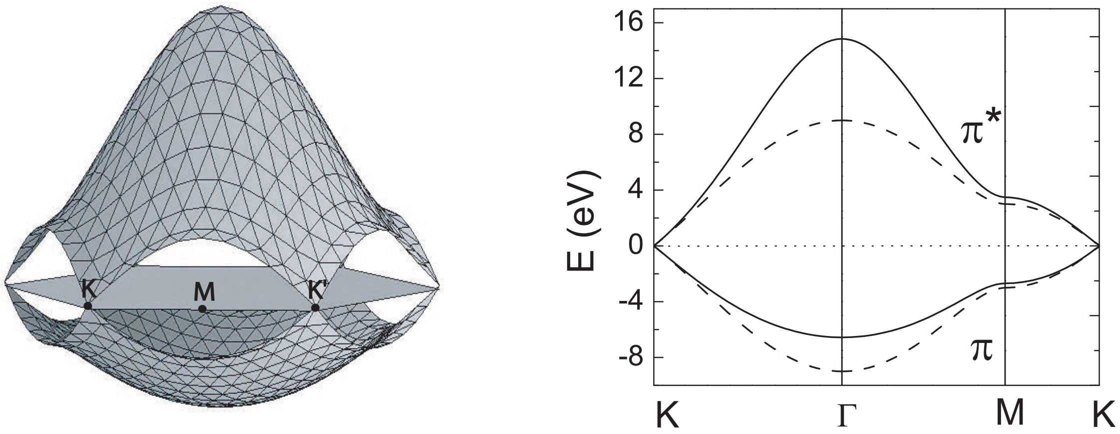

Figure 2.2: Left panel: The π band dispersion of graphite over the whole Brillouin zone as it results from a simple tight-binding model including the overlap integral. **Right panel:** Energy dispersion of graphite along the high-symmetry directions of the Brillouin zone including the overlap integral ($s = 0.129$, solid line) and in the Slater-Koster scheme ($s = 0$, dashed line).

Chiral vector

Although SWCNTs are not actually produced in this way, the easiest way to visualize the geometric structure of SWCNTs is by imagining a rectangular section of a graphene sheet. The nanotube is then formed by rolling up this graphene sheet section. This section and thus the structure of the SWCNT is specified by the vector $\overrightarrow{AB}$ in Fig. 2.3 which starts and ends at a lattice point. This vector, also written as $\vec{C_h}$, defines the circumference of the nanotube and is called *chiral vector* or *Hamada vector.* It can be expressed by the real space unit vectors of the honeycomb lattice, $\vec{a_1}$ and $\vec{a_2}$:

$$\vec{C_h} = n\vec{a_1} + m\vec{a_2} := (n, m) \qquad (n, m \in \mathbb{Z}). \tag{2.5}$$

Because of the sixfold symmetry of the honeycomb lattice, the range of n and m is restricted to $0 \leq |m| \leq |n|$. The absolute value of the chiral vector

$$|\vec{C_h}| = \sqrt{3}a_0\sqrt{n^2 + m^2 + nm}, \tag{2.6}$$

is equal to the circumference of the nanotube which is formed by the graphene section. The diameter d of the nanotube is then given by

$$d = |\vec{C_h}|/\pi = \sqrt{3}\,a_0\sqrt{n^2 + m^2 + nm}/\pi, \tag{2.7}$$

where $a_0 = 1.42$ Å is the nearest-neighbor C-C distance.

Chiral angle

Another useful value is the so-called chiral angle θ, which is the angle between $\vec{a_1}$ and $\vec{C_h}$. It can be expressed as

$$\cos\theta = \frac{\vec{C_h} \cdot \vec{a_1}}{|\vec{C_h}||\vec{a_1}|} = \frac{2n + m}{2\sqrt{n^2 + m^2 + nm}}. \tag{2.8}$$

Due to the hexagonal symmetry of the honeycomb lattice, its values are in the range $0 \leq |\theta| \leq 30°$. θ also denotes the tilt of the angle of the hexagons with respect to the direction of the nanotube axis. SWCNTs can be classified by the index pair (n, m).

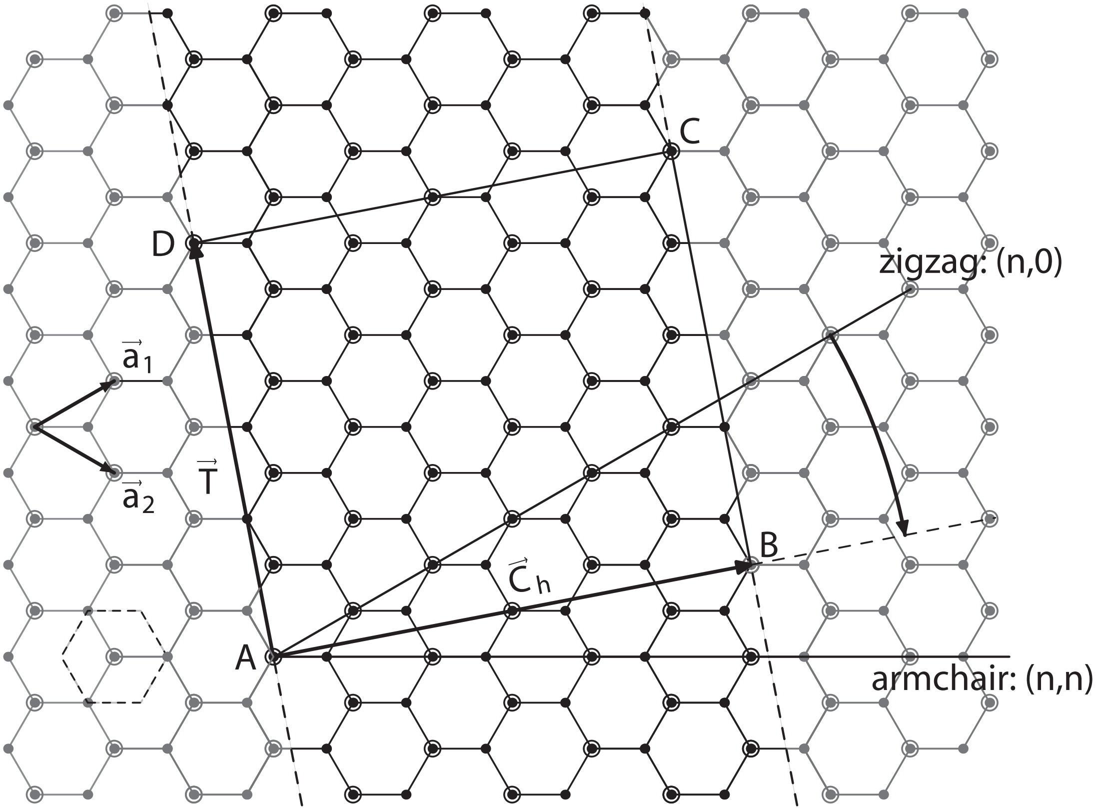

Figure 2.3: Schematic honeycomb structure of a graphene sheet. Carbon atoms are at the vertices. SWCNTs $(4, 2)$ can be formed by folding the sheet along lattice vectors. The two basis vectors are $\vec{a_1}$ and $\vec{a_2}$ [27]. Figure after [28].

SWCNTs are called

- **armchair** nanotubes if $n = m$. This means that $\vec{C_h} = (n, n)$ and $\theta = 30°$;
- **zigzag** nanotubes if $m = 0$. This means that $\vec{C_h} = (n, 0)$ and $\theta = 0°$;
- **chiral** nanotubes in all other cases.

Examples for this classification are given in Fig. 2.4.

Translational vector

The translational vector

$$\vec{T} = t_1\vec{a_1} + t_2\vec{a_2} := (t_1, t_2) \quad (t_1, t_2 \text{ are integers, } 0 \leq |m| \leq |n|) \tag{2.9}$$

is defined as the unit vector of a 1D carbon nanotube. It is parallel to the nanotube axis and normal to the chiral vector $\vec{C_h}$ in the unrolled graphene lattice. It extends from the origin of $\vec{C_h}$ to the first lattice point on the line perpendicular to $\vec{C_h}$. Using $\vec{C_h} \cdot \vec{T} = 0$, t_1 and t_2 can be expressed as a function of the indices n and m as

$$t_1 = \frac{2n + m}{d_R} \quad \text{and} \quad t_2 = \frac{2m + n}{d_R}, \tag{2.10}$$

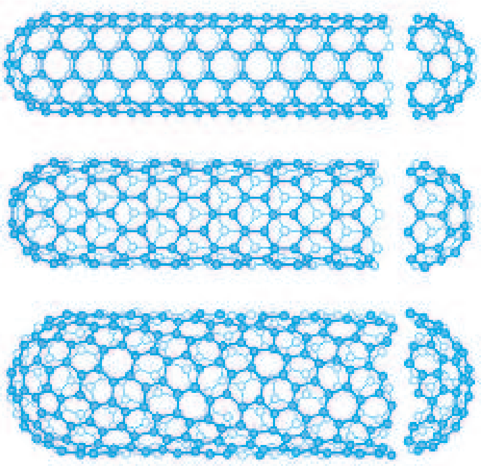

Figure 2.4: Schematic honeycomb structure of three types of SWCNTs. From top to bottom: A (5,5) armchair tube,a (9,0) zigzag tube, and a (10,5) chiral tube [27].

where d_R is the greatest common divisor of $(2n+m)$ and $(2m+n)$. The one-dimensional unit cell is now the rolled-up rectangle spanned by $\vec{C_h}$ and $\vec{T}$. This allows us to derive the number of hexagons per unit cell N, which is important for the determination of the number of electronic and phononic bands in SWCNTs. The number of hexagons in one unit cell is given by the area of the rectangle spanned by $\vec{C_h}$ and $\vec{T}$ divided by the area of one hexagon. This value N' results as

$$N' = \frac{2(m^2+mn+n^2)}{d_R}. \tag{2.11}$$

Since every hexagon contains two carbon atoms, the number of carbon atoms in a SWCNT unit cell results as

$$N = 2N' = \frac{4(m^2+mn+n^2)}{d_R}. \tag{2.12}$$

2.2.2 Reciprocal lattice and Brillouin zone

The reciprocal lattice is defined by the relation $\vec{R_i} \cdot \vec{K_i} = 2\pi\delta_{ij}$. $\vec{R_i}$ are the lattice vectors of the one-dimensional real space unit cell $\vec{T}$ and the circumferential vector $\vec{C_h}$. $\vec{K_i}$ are the reciprocal lattice vectors. The Brillouin zone of SWCNTs is calculated from these resulting relations:

$$\vec{C_h} \cdot \vec{K_1} = 2\pi, \quad \vec{T} \cdot \vec{K_1} = 0, \quad \vec{C_h} \cdot \vec{K_2} = 0, \quad \vec{T} \cdot \vec{K_2} = 2\pi \tag{2.13}$$

The reciprocal lattice vectors can now be expressed as a function of the reciprocal lattice vectors of the hexagonal graphene lattice, $\vec{b_1}$ and $\vec{b_2}$ (as depicted in Fig. 2.1):

$$\vec{K_1} = (-t_2\vec{b_1} + t1\vec{b_2})/N \quad and \quad \vec{K_2} = (m\vec{b_1} - n\vec{b_2})/N. \tag{2.14}$$

The resulting Brillouin zone is now a system of parallel lines with a length of $|\vec{K_2}|$ and a spacing of $|\vec{K_1}|$. It is depicted in Fig. 2.5 for a zigzag and an armchair nanotube with respect to the reciprocal lattice of two-dimensional graphite. The length of the parallel lines is given by $2\pi/|\vec{T}|$.

Two wave vectors which differ by $N\vec{K_1} = (-t_2\vec{b_1} + t_1\vec{b_2})$ are equivalent because this vector corresponds to a reciprocal lattice vector of two-dimensional graphite. The $N-1$ wave vectors which differ by $\mu\vec{K_1}$ with $\mu = 1, 2, ..., N-1$ are not equivalent as t_1 and t_2 do

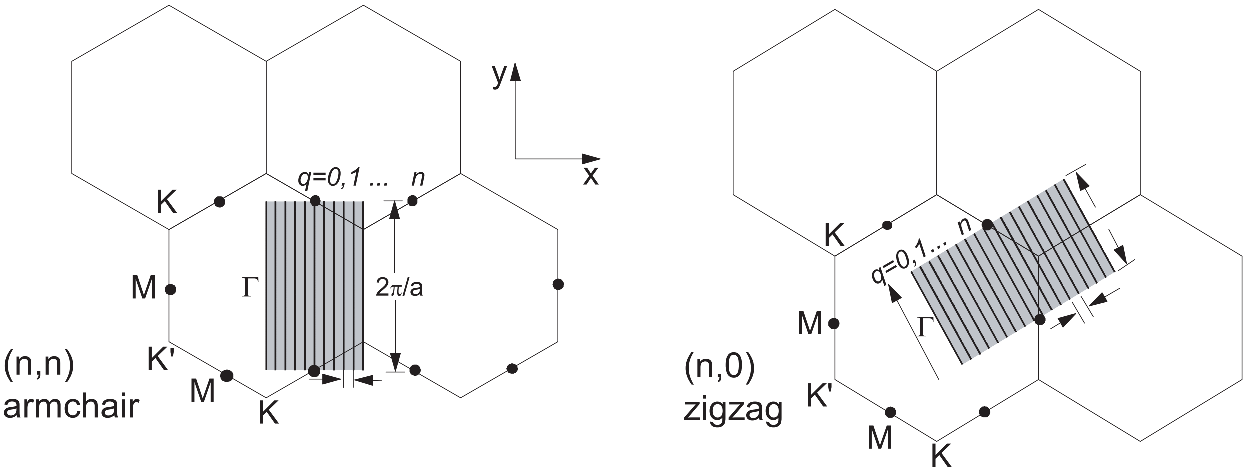

Figure 2.5: The first Brillouin zones for an armchair tube (n, n) [e.g. (10,10)] (a) and a zigzag $(n, 0)$ [e.g. (17,0)] (b). The reciprocal lattice vectors $\vec{K}_1$ and $\vec{K}_2$ corresponding to the real space unit cell of these tubes as defined by $\vec{C}_h$ and $\vec{T}$, respectively. The periodic boundary conditions along the circumference of the tube result in allowed $\vec{K}_1$ values as indicated by the n vertical lines marked $q = 0$ through n.

not have a common divisor except unity. The reciprocal lattice vector can thus be expressed as

$$\vec{K} = k\frac{\vec{K}_2}{|\vec{K}_2|} + \mu\vec{K}_1, \qquad \mu = 0, 1, ..., N-1 \text{ and } -\pi/|\vec{T}| < k < \pi/|\vec{T}| \tag{2.15}$$

As a result of the periodic boundary conditions along the circumference, N discrete k vectors perpendicular to the nanotube axis are obtained. Continuous wave vectors are allowed along the axis provided an infinite length of the nanotube is assumed.

2.3 Electronic band structure of SWCNT

Zone folding and band structure

Due to the close relation between graphene and SWCNTs, it is relatively easy to obtain the SWCNT electronic band structure from that of graphene. As seen in the previous section, the periodic boundary conditions along the circumferential direction permit only discrete wave vectors. Thus the SWCNT energy bands consist of N one-dimensional energy dispersion relations which fulfill the condition for the allowed states in Eq. 2.15. These lines are cross sections of those for two-dimensional graphene and are obtained by simply replacing the wave vector k in the graphite energy dispersion from Eq. (2.4) with the allowed wave vectors:

$$E_\mu(k) = E_{g2D}(k\frac{\vec{K}_2}{|\vec{K}_2|} + \mu\vec{K}_1), \qquad \mu = 0, 1, ..., N-1 \text{ and } -\pi/|\vec{T}| < k < \pi/|\vec{T}| \tag{2.16}$$

This method is called zone-folding. The position and direction of the allowed SWCNT k states with respect to the graphene Brillouin zone now depend on the direction in which the nanotube is rolled up, i.e. the chirality. In this light it is easily conceivable that different SWCNT chiralities have different electronic band structures. One important condition is whether the cutting lines cross the K-point of the graphene Brillouin zone because the K-point is the only point where the graphite π band crosses the Fermi level. If a cutting line now crosses the K-point, the resulting SWCNT band structure also contains a band which crosses the Fermi level, the resulting nanotube is thus metallic. If the line does not cross the K-point, a gap appears in the SWCNT band structure. The resulting nanotube is a semiconductor. A simple rule is obtained from zone-folding considerations: A SWCNT is metallic if $m - n \in 3\mathbb{Z}$. Hence, all armchair nanotubes ($n = m$) are metallic. Fig. 2.5 illustrates this further: The allowed wave vectors are given with respect to the Γ point. In the case of an armchair tube this means that the wave vector cutting the Γ point automatically also crosses the K point, resulting in a metallic nanotube.

Fig. 2.6 shows the SWCNT band structure resulting from the zone folding method of the graphite band structure as obtained from the tight-binding model for a metallic (10,10) tube and a semiconducting (17,0) tube. The metallic tube has eleven bands in the valence and conduction band, respectively. One of these bands crosses the Fermi level. The other bands are separated by at least 1.8 eV and thus do not contribute to the conductivity. There is obviously no subband crossing the Fermi level in the case of the semiconducting tube. Instead, a direct gap of approximately 0.8 eV can be observed.

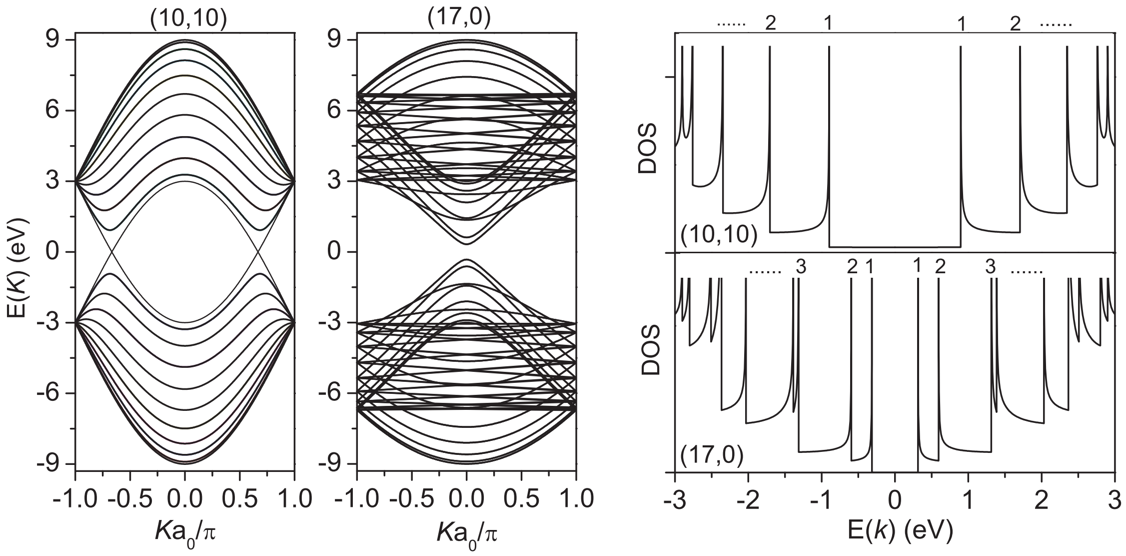

Figure 2.6: Left panel: Dispersion relations for a metallic (10,10) and a semiconducting (17,0) tube as they result from a simple tight-binding approximation. **Right panel:** Density of states of the same tubes as results from Eq. (2.17). The numbers indicate the vHs from the corresponding subbands.

Starting from the band structure, the electronic density of states (DOS) can be calculated using

$$D(E) = \frac{T}{2\pi N} \sum_{\pm} \sum_{\mu=1}^{N} \int \frac{1}{\left|\frac{dE_\mu^\pm(k)}{dk}\right|} \delta[E_\mu^\pm(k) - E] dE \ , \tag{2.17}$$

where the summation is taken for the N one-dimensional conduction (+ sign) and valence (- sign) bands, respectively [29]. The right panel of Fig. 2.6 depicts the resulting DOS from the two band structures shown in the left panel. The most striking features are the spikes in the DOS, the so-called van-Hove singularities (vHs). The vHs are of great importance for the spectroscopic investigation and characterization of SWCNTs since they define the optical properties. In this regard, their most important property is that the gap between corresponding vHs scales with the inverse diameter. The allowed k-vectors in a SWCNT are the cutting lines of the graphite band structure. If a SWCNT is large enough, these cutting lines are close enough to assume that the dispersion of graphite is linear between them. The cutting lines, and consequently the positions where the bands are flat and lead to vHs in the DOS, are thus equidistant in energy. The transition energies between corresponding vHs are then given by

$$E_{ii} = \frac{2ia_0\gamma_0}{d} \; , \tag{2.18}$$

where those transitions where i is a multiple of three belong to metallic tubes, the others to the semiconducting tubes. This relation between diameter and transition energy is crucial for the optical investigation of SWCNTs by e.g. optical absorption or Raman spectroscopy, although Eq. (2.18) can rarely be used for advanced experiments in its simple form.

For more sophisticated experiments, i.e. the assignment of individual peaks in Raman or photoluminescence spectroscopy to specific chiralities, a more accurate calculation of the transition energies is needed. It can be achieved e.g. by third-neighbor tight-binding [30],*ab initio* calculations or by a symmetry-adapted non-orthogonal tight-binding model, where curvature effects are included [31]. Considerable refinements occur as a result of the trigonal warping effect [32]. These refinements become larger with decreasing tube diameter and are usually illustrated in the so-called Kataura plot [33]. In addition, for smaller SWCNTs with diameters d $\lessapprox$ 1 nm curvature effects lead to discernible deviations from this relation [31] which can be categorized in a family pattern [34, 35] where all SWCNTs with $(2n + m) = l$ form a family l. The SWCNTs are further classified as semiconducting type I (SI) if $(2n+m) \mod 3 = 1$, semiconducting type II (SII) if $(2n+m) \mod 3 = 2$, and metallic (M) if $(2n+m) \mod 3 = 0$. For tubes with diameters as those used in this thesis however, these confinements play a less important role and the quantitative properties of the sample can be adequately described by the simple tight-binding model.

2.4 Synthesis and characterization of SWCNT

2.4.1 SWCNT synthesis

There is a variety of methods of producing carbon nanotubes, each with their own advantages and disadvantages. The method of production and the parameters used greatly influence the properties of the nanotubes grown, such as mean diameter or purity. SWCNTs can only be grown with the aid of catalysts. Without the use of catalysts, mainly MWCNTs are grown. Today, SWCNTs can be grown with diameters from 0.8 to 3 nm. The synthesis methods are furthermore classified by their yield, i.e. the amount of SWCNTs in the soot. The remainder of the soot consists of fullerenes, graphitic carbon and catalyst particles. In order to obtain high purity samples, a lot of work is required on post-production purification.

Due to the unfortunate fact that the structural energy depends only weakly on the chirality of a nanotube it is to date not possible to control exactly which chiralities are grown. Therefore, every macroscopic sample contains a distribution of nanotube diameters with both semiconducting and metallic nanotubes in the sample. There are three common ways to produce carbon nanotubes. In the laser ablation and arc discharge methods, a

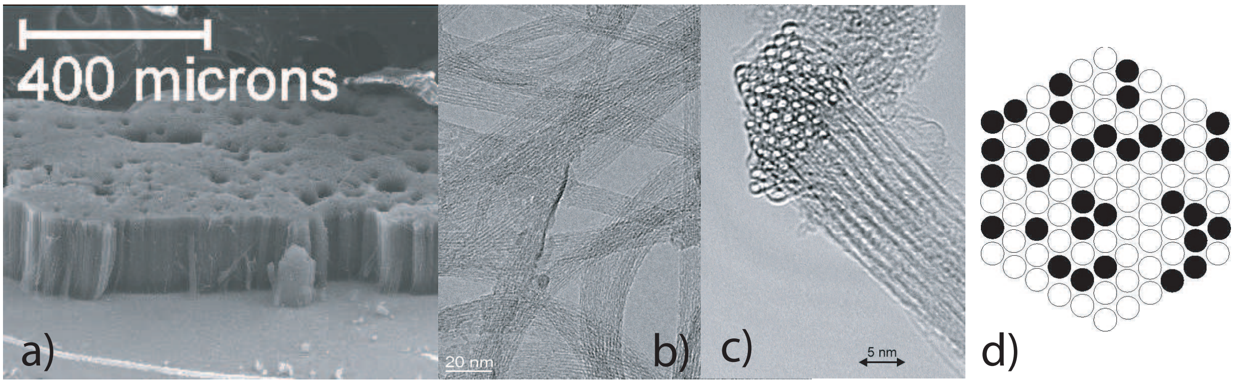

Figure 2.7: a) Aligned SWCNTs on substrate produced by CVD. b) SWCNT bundles made by laser ablation. c) Top view of a SWCNT bundle with the typical hexagonal arrangement. d) Schematic representation of a SWCNT bundle. Open circles represent semiconducting tubes, filled circles are metallic SWCNTs.

carbon target is vaporized while the chemical vapor deposition (CVD) relies on the catalytic decomposition of a carbon source. These methods are now briefly introduced.

- **Laser ablation:** In the laser ablation method, a target consisting of graphite mixed with some atom-% of catalyst particles is vaporized by a powerful laser in a furnace at approximately 1200°C. The SWCNTs form in the gas phase and are transported to a cooled copper collector by a flow of an inert gas [36]. As in the other synthesis techniques, the most common catalyst materials are Ni, Co and Fe. Most of the time He or Ar is used as the inert gas. For the vaporization, pulsed [37, 38] or continuous wave (cw) lasers [39, 40] can be used.

  The SWCNTs produced by this method are typically rather short ($\approx 0.1\,\mathrm{mm}$) and, depending on the synthesis conditions, SWCNTs with a mean diameter between 1.0 and 1.6 nm are obtained. Using laser ablation, samples with a very narrow diameter distribution (variance $\approx 0.3\,\mathrm{nm}$) can be produced. This makes samples produced with this method especially useful for the studies presented in this work. Consequently, the samples investigated were produced by laser ablation. Furthermore, the SWCNTs obtained using this method are usually arranged in bundles [41].

- **Arc discharge:** This method was originally used for the synthesis of C_{60} fullerenes [1]. The first observed MWCNTs [3] and SWCNTs [4, 5] were also produced using this method. The method is very similar to laser ablation, except that the graphite is vaporized by a discharge between two carbon rods caused by a direct current of 50 to 100 A driven by approximately 20 V [42]. Again, if the target rod contains small amounts of catalyst particles, SWCNTs can be grown.

- **Chemical vapor deposition (CVD):**

  Chemical vapor deposition (CVD) relies on the decomposition of a gaseous hydrocarbon carbon source using heat or plasma and, in the case of SWCNTs, with the aid of (molten) catalyst particles. The catalyst particles absorb the carbon, eventually leading to an oversaturation of carbon in the particle. This leads to the formation of carbon structures at the surface of the particle which tend to grow into tubes. In the perfect case, one nanotube grows from one catalyst particle [43]. This allows spatial positioning of a nanotube by arranging the catalyst particles in a controlled way, e.g. using lithography techniques [44]. Furthermore, CVD allows the synthesis of vertically aligned nanotubes [45–48] and of extraordinarily long nanotubes [49]. The method can easily be upscaled for production of larger amounts of nanotube materials.

2.4.2 Determining the electronic and optical properties of SWCNT

There are several well-established methods available for the characterization of SWCNTs. They can roughly be divided into methods probing the optical properties and methods probing the electronic properties, both either on a bulk or local scale. The optical properties are mainly determined by transitions between corresponding vHs. As the energy of these transitions is inversely proportional to the SWCNT diameter, optical measurements provide a direct access to the structural properties of the SWCNTs, or more precisely, the diameter and diameter distribution. In optical absorption spectroscopy (OAS) strong absorptions can be assigned to transitions between corresponding vHs and the width and energy position of these absorptions allow the sample properties to be determined. The optical properties are also probed in resonant Raman spectroscopy where the response is greatly enhanced if the laser excitation energy matches a transition energy. By varying the resonance conditions with different laser energies, transitions of all tubes present in the sample can be probed. Since the radial breathing mode of SWCNTs is equally inversely proportional to the tube diameter, the sample properties can be determined. Photoluminescence spectroscopy can be applied to individualized semiconducting SWCNTs. The combinations of excitation and fluorescence wavelengths can be assigned to particular chiralities of the semiconducting, making this method likewise useful for the characterization of SWCNT samples.

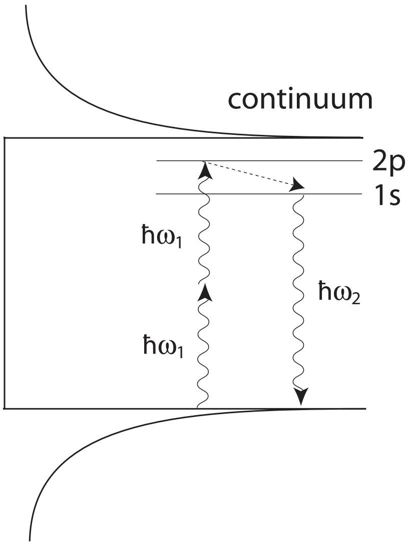

Figure 2.8: Schematic illustration of the SWCNT band structure and the 1s and 2p exciton states. The two-photon excitation process is indicated by the two photons with energy $\hbar\omega_1$. In the exciton picture the 1s exciton state is forbidden upon two-photon excitation. The 2p exciton states relax to the 1s exciton state and decay under fluorescence, i.e. the emission of a photon with energy $\hbar\omega_2$

Nevertheless, in these optical methods, correlation effects – in particular excitonic effects – have to be taken into account. In general, excitons are electron-hole pairs which form correlated entities due to their mutual Coulomb interaction. The energy states of this quasiparticle are situated in the gap of the semiconductor. In the case of a localized exciton, they can be treated very similarly to the hydrogen atom since such a system can be regarded as a localized hole with the electron in an orbital around this hole. The energy states thus result in close analogy to the Rydberg series with the exciton binding energies given with respect to the corresponding electronic state. The excitonic state with the highest binding energy is the 1s state, followed by the 2s singlet and the 2p triplet state [50]. This scheme is depicted in Fig. 2.8 for the case of SWCNTs. It becomes clear that transitions involving exciton states are lower than those between the actual bands. Although the existence of excitons in SWCNTs was suspected for a long time [51], the experimental verification was only recently carried out. The exciton binding energy in SWCNTs can directly be determined by two-photon excitation spectroscopy [21]. Due to the electric-dipole selection rules one-photon processes can only lead to an excitation into the 1s exciton state. For the excitation into the 2p state, the simultaneous absorption of two photons of energy $\hbar\omega_1$ is necessary. Such an excitation is depicted in Fig. 2.8. The excited state created in this way now relaxes rapidly into the 1s exciton state [52]. From there, fluorescence through a one-photon process takes place where the photon has the energy $\hbar\omega_2$. The energy difference between the exciton 1s and 2p states is now

$$E_{2\mathrm{p}} - E_{1\mathrm{s}} = 2 \cdot \hbar\omega_1 - \hbar\omega_2 \ . \tag{2.19}$$

The obtained value can now be used to calculate the exciton binding energy with respect to the band edge. An exciton binding energy of 420 meV results for SWCNTs with 0.8 nm diameter [21]. The exciton binding energy thus constitutes an important part of the gap energy which in this case is 1.3 eV. For larger diameter nanotubes such as those used in this thesis the exciton binding energy is lower, but with a binding energy of $\approx$ 240 meV far from negligible [53, 54]. It is a good estimate of the strength of other correlation effects such as the electron-electron interaction. Although the excitonic effects themselves play only a minor role in this thesis, they are a good measure for the energy scale of the electron-electron interactions as is discussed below.

Direct probes of the band structure of bulk samples are provided by photoemission spectroscopy (PES), inverse photoemission spectroscopy (IPES), x-ray absorption spectroscopy (XAS) and electron energy loss spectroscopy (EELS). But here, too, correlation effects play an important role, since the final state is different from the ground state due to the removal (PES, XAS, EELS) or addition (IPES) of an electron. Direct determination of the transition energies between vHs with these techniques has proven rather difficult. In photoemission-inverse photoemission experiments, one would have to identify the vHs in valence and conduction band respectively. Whereas the vHs were already observed in PES experiments [55], the resolution and signal of inverse photoemission are too low to also observe the vHs from the conduction band [56]. On a local scale, the electronic properties can be probed by scanning tunneling spectroscopy (STS) or transport experiments. However, the accuracy of STS measurements on individual SWCNT suffers from charging and screening effects from the conducting substrate. In order to interpret the results in the tight-binding model, an unrealistic value for the transfer integral of $\gamma_0 = 2.5\,\mathrm{eV}$ has to be used [57].

Notwithstanding the drawbacks due to correlation effects, all these optical and electronic methods have proven to be very powerful in the investigation of SWCNTs and related compounds and have led to a profound understanding of their properties. Furthermore, the general trends can be understood within the tight-binding model and for larger tubes ($\geq$ 1.3 nm), where confinements in the TB model and due to correlations play a less important role, quantitative information on the sample properties can also easily be obtained.

2.5 Functionalization

Single-wall carbon nanotubes are the subject of intense research, not only because of their peculiar structural and electronic properties, but also because of their application potential. This potential is augmented by the fact that SWCNTs can be modified in a variety of ways. One such possible functionalization is doping with electron acceptors or donors. This technique allows the electronic structure to be changed by inducing a charge transfer to or from the nanotube. A term used synonymously for this technique is intercalation, since the doping in carbon nanostructures often takes place in certain lattice spaces, where it "intercalates". Another way of functionalizing nanotubes is by using the nanospace inside the tubes as a container and fill the tubes. This has been performed with a variety of organic molecules such as TCNQ or anthracene [58]. One of the most popular procedures is filling with fullerenes, and particulary C_{60} molecules, to form so-called C_{60} peapods [59].

2.5.1 Intercalation

Doping of materials with either electron donors or electron acceptors is a widely used method in solid state physics. Doping with electron donors is called n-type doping while the doping with electron acceptors is called p-type doping. Surely the best-known example is doping of semiconducting materials such as silicon, which allows the creation of p-n junctions needed e.g. for transistors or diodes. It has also been studied extensively for graphite intercalation compounds (GICs) [60] and fullerene intercalation compounds (FICs) [61]. The term "intercalation" stems from the fact that the doping atom is situated in preferential sites inside the lattice of these compounds. In the studies of graphite and carbon nanostructures generally the alkali metals from the first group of the periodic system such as lithium (Li), sodium (Na), potassium (K), rubidium (Rb) and cesium (Cs) are used for n-type doping. P-type doping can be achieved using e.g. iron-trichloride ($FeCl_3$), bromine (Br_2) or iodine (I_2).

Structural effects of doping

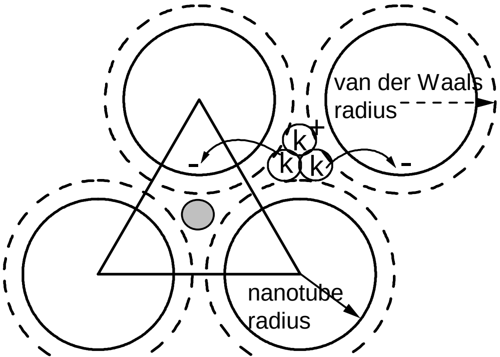

Figure 2.9: Simple model for an alkali metal-intercalated (10,10) nanotube: (1) Low doping: K ions are at the center of the interstitial voids (grey ball). (2) Saturation doping: three K per cavity are situated at the extremities of the triangular cavities (empty circles). The dashed line is the nanotube radius plus the van der Waals distance (about 1.6 Å). Figure adapted from [62].

In a macroscopic sample of SWCNTs, the tubes are arranged in a hexagonal lattice. The tubes are only weakly bonded by van der Waals interaction. The lattice constant can be determined by electron diffraction. In intercalated SWCNT bundles, this lattice constant increases with the dopant concentration. This shows that the dopant resides in the triangular channels between the tubes, the so-called interstitial sites [63]. Fig. 2.9 schematically depicts the sites where the dopant resides and how a certain amount of doping atoms leads to the expansion of the lattice. In the case of potassium doping, the expansion can amount to up to 10%. In addition, at least for C_{60} peapods, it has also been shown that the dopant can move into the SWCNT cage if the tubes are opened by post-synthesis oxidation [64].

Rigid band shift model

In general, doping with electron donors or acceptors leads to a shift of the Fermi level. In the case of SWCNTs, the band structure is only very weakly modified by doping [65] and the current state of the electronic system is obtained by varying the Fermi level in the band structure. Recent calculations within an extended tight-binding model predicted a change in the SWCNT gap energy, i.e. the position of the vHs upon p-type doping [66]. The effect was estimated to amount to approximately 10 meV upon removal of 0.04 e^- per carbon atom. Whether the doping leads to an increase or decrease of the gap energy depends on the chirality of the respective tubes. This would mean that a simple rigid band shift model would no longer be applicable. However, the effect is small compared to the shift of the Fermi level. Upon a charge transfer of 0.04 e^- per carbon atom, corresponding to a C/K = 25, the Fermi level shift usually approaches 1 eV for SWCNTs. The effect of a band structure modification by doping can thus be considered negligible and the band structure of the doped compound can be obtained by simply shifting the Fermi level in the band structure of the pristine compound. This picture is called rigid band-shift model. It has already been successfully used in the graphite intercalation compounds (GICs) [60]. Nevertheless, the model does not apply to all carbon nanostructures equally. In fullerene intercalation compounds (FICs), such as intercalated C_{60}, the so-called line phases exhibit distinctly different electronic structures of the different doping phases [61].

Free charge carriers in doped SWCNT

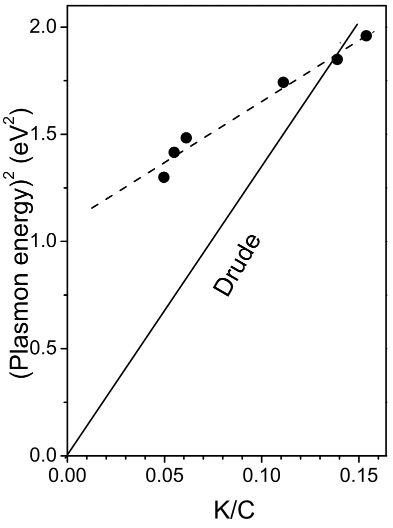

Figure 2.10: Square of the charge-carrier plasmon energy of doped SWCNTs as a function of the dopant concentration obtained by EELS. The dashed line indicates the doping dependence as it follows from the measured points. The solid line describes the behavior as it follows from the Drude model (see Eq. (2.20)). The figure is taken from [62]

The shift of the Fermi level leads to a loss of the optical transitions as can be monitored by optical absorption and Raman spectroscopy where a filling or depletion of the vHs between which the resonant optical transition takes place, leads to a resonance loss and thus to a dramatic decrease of the response intensity [67]. EELS measurements revealed the emergence of a new feature in the loss function upon doping [68] which could not be ascribed to interband transitions. It is assigned to a collective mode of the conduction electrons, the so-called charge-carrier or Drude plasmon. The squared plasmon energy E_{P}^2 depends on the charge carrier density n and the effective mass $m^\star$ as

$$E_{\mathrm{P}}^2 = \frac{\hbar n e^2}{m^\star \varepsilon_\infty \varepsilon_0} \ . \tag{2.20}$$

ε_∞ is the background dielectric constant. Fig. 2.10 shows the squared plasmon energy position as a function of the dopant concentration. The plasmon energy also increases with increasing doping, as it is expected for an increasing charge carrier density. However, the plasmon energy cannot be extrapolated to zero as it would be expected from the model, indicating that the effective mass $m^\star$ is also doping-dependent [62, 68].

The plasmon observed here is an indication of free charge carriers. Since it does not appear in the pristine state and at low doping steps, it could be an indication of a qualitative change of the electronic properties upon doping. A further study of this crossover promises to reveal interesting properties and will therefore be a subject of detailed investigation in this thesis.

2.5.2 Structure and fabrication of C_{60} peapods

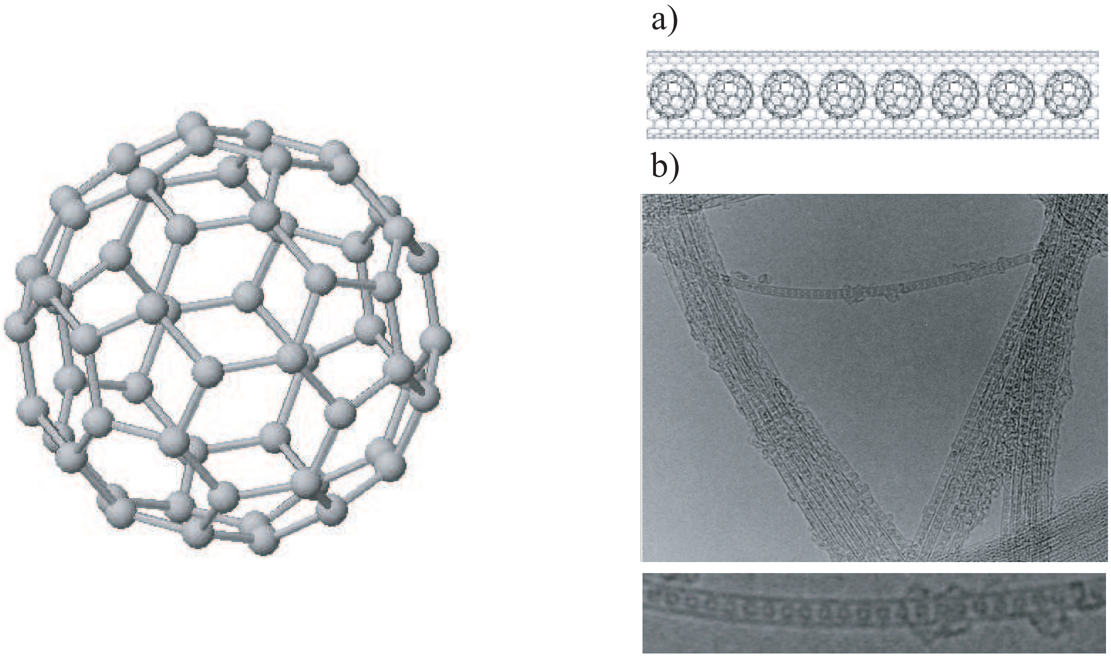

Figure 2.11: Left panel: Schematic illustration of a C_{60} fullerene molecule. **Right panel: a)** Schematic illustration of C_{60} peapods: C_{60} molecules are situated inside a SWCNTs. **b)** Transmission electron microscopy images of C_{60} peapods. The upper panel shows an overview of bundles of C_{60} peapods, the lower panel shows an individual SWCNTs in which the C_{60} molecules can clearly be identified. It is also shown that the filling ratio of this sample is very high.

C_{60} peapods are a compound formed by filling SWCNTs with C_{60} molecules. The fullerene C_{60} is a molecule consisting of 60 carbon atoms which form a cage consisting of hexagons and pentagons (see left panel of Fig. 2.11) with a diameter of 0.7 Å. Inside the SWCNTs, C_{60} forms a one-dimensional chain as opposed to the fcc crystal structure of pure solid C_{60} [69]. The right panel of Fig. 2.11 shows a computer-simulated image as well as high-resolution transmission electron microscopy (TEM) images of C_{60} peapods. The term *peapods* is clearly derived from the similarity to peas which grow in pods. X-ray and electron diffraction showed that the distance between neighboring C_{60} molecules in optimally filled C_{60} peapods is about 0.97 Å [70,71], which is slightly smaller than in the face-centered cubic (fcc) C_{60} crystal [6] but much bigger than that in polymerized C_{60}.

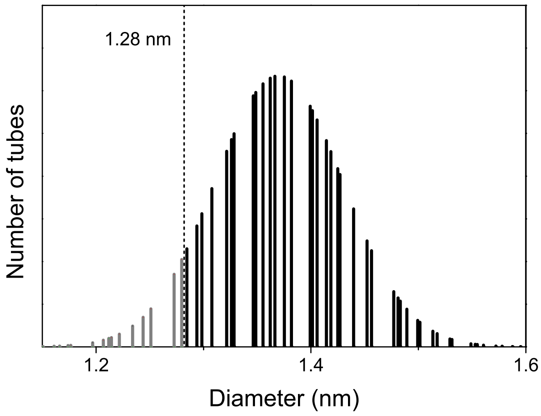

Figure 2.12: Tube distribution of an SWCNT sample with 1.37 nm mean diameter and a standard deviation of the distribution of $\Gamma_d = 0.06$ nm. The dashed vertical line at 1.28 nm denotes the minimum diameter where SWCNTs can be filled with C_{60}. The black lines thus represent tubes which have a sufficiently large diameter to be filled with C_{60}, the grey lines represent tubes which cannot be filled with C_{60}.

Obviously, SWCNTs with a diameter below a certain threshold diameter cannot be filled with C_{60} since there is not enough space inside the tube. Simple geometric considerations about the van der Waals interaction between fullerenes and C_{60} suggest that the minimum diameter for C_{60} encapsulation is 1.29 nm and the optimum diameter for filling is 1.36 nm. Theory also predicts that the C_{60} encapsulation is exothermic above a SWCNT diameter of 1.28 Å [72], below this diameter it is no longer energetically favored. As a consequence, not all tubes in a macroscopic sample of SWCNTs can be filled with C_{60} even if their mean diameter is above the filling threshold. Due to the finite distribution width, a number of tubes is too small to be filled. Fig. 2.12 illustrates this fact on the basis of the sample parameters of the SWCNTs used in this work. Approximately 85 % of all tubes can theoretically encapsulate C_{60} molecules in our case. The filling ratio can be obtained using EELS by comparing the spectra of unfilled SWCNTs with those of the peapods [73]. Here it was shown that these maximum filling ratios can indeed be reached i.e., that those tubes which can accommodate C_{60} can be filled such that their filling ratio is very close to 100%.

There are a variety of ways to fill SWCNTs with C_{60} molecules. Usually the SWCNT buckypaper is sealed and then heated in a quartz ampoule together with fullerene powder [74]. Another method is low temperature filling from C_{60} in a solvent [75]. In this thesis, the C_{60} was evaporated directly on a SWCNT film in UHV as will be described below in detail. This method allows the fabrication of C_{60} peapod samples under UHV conditions and produces clean samples with a very high filling ratio .

2.5.3 Electronic structure of C_{60} peapods

The electronic structures of both C_{60} fullerenes and SWCNTs have been a subject of intense studies over the recent years and are reasonably well understood. However, uncertainties remain regarding their combination and interplay upon the formation of C_{60} peapods. In particular the adjustment of the Fermi level will be important. This plays an important role even when only regarding a mixture of metallic and semiconducting SWCNTs. With the addition of C_{60}– which is semiconducting in the isolated form – the situation becomes more complex. Concerning the TLL behavior, the doping role of the lowest unoccupied molecular orbital has to be considered carefully. Below, theoretical and experimental results on the electronic structure of C_{60} peapods are discussed in order to reach a starting point for the discussion of the photoemission experiments.

The electronic structure of the C_{60} fullerene

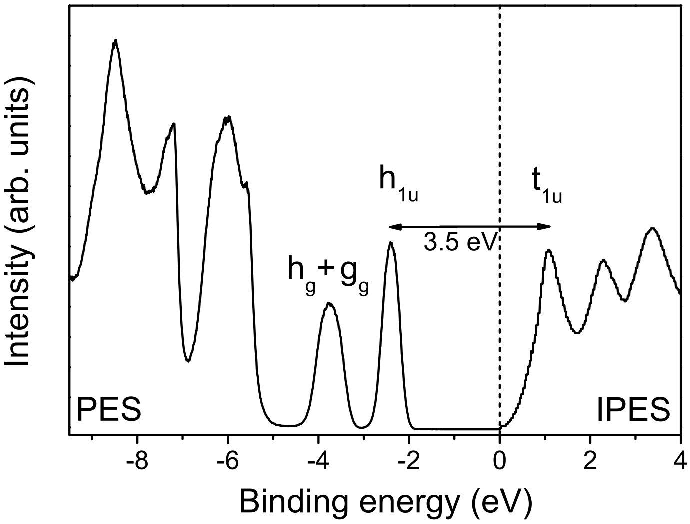

Figure 2.13: Valence band and conduction band spectra of C_{60} taken by PES and inverse PES respectively. The molecular orbitals are labelled according to their symmetry. The spectra are taken from Ref. [76] (PES) and Ref. [77] (IPES).

C_{60} is a semiconducting material. Its electronic structure is given by molecular orbitals [78], where the two highest occupied molecular orbitals – labelled according to their symmetry[2] – are the h_u and h_g+g_g bands. The orbitals closest to the Fermi level are the occupied h_u band and the unoccupied t_{1u} band. They form a gap width a width of 3.5 eV (maximum-maximum) [77, 79]. Photoemission experiments reveal a binding energy of the occupied h_u band of 2.3 eV. Its bandwidth was found to be approximately 0.4 eV [80] as it was suggested by theory [81]. Fig. 2.13 shows a photoemission spectrum of solid C_{60} taken

---

[2] In the literature they are often referred to as HOMO (highest occupied molecular orbital) and HOMO-1,2. In this notation, the lowest unoccupied molecular orbital, which has t_{1u} symmetry, is called LUMO. In this thesis, the molecular orbitals will be labelled according to their symmetry notation.

from Ref. [76]. In accordance with the other studies mentioned above, the h_u and h_g+g_g bands are found at 2.3 and 3.7 eV binding energy respectively. This figure also shows the unoccupied molecular orbitals as obtained from inverse PES. Inverse PES measurements yield an onset of the t_{1u} band between 0.2 eV [77] and 0.8 eV [82] above the chemical potential.

The electronic structure of C_{60} peapods

One important question concerning the electronic properties is how the electronic states of C_{60} and the encapsulating tubes interact and whether they hybridize. From scanning tunneling spectroscopy experiments it was concluded that the π states of the two constituents strongly hybridize [83]. However, this was not supported by theoretical calculations, where a significant interaction between the C_{60} filling and the tube walls was only predicted for cases with a small diameter difference between filling and tube, i.e. in a case where C_{60} usually does not enter a tube at all [72, 84, 85]. EELS measurements revealed that the electronic and optical properties of C_{60} inside SWCNTs are very close to those of solid C_{60}, leading to the conclusion that the states only weakly hybridize [71].

The position of the lowest unoccupied molecular orbital, the t_{1u} band, is crucial for the analysis of doping experiments. LDA calculations for metallic [72] and zigzag [86] predict a downshift of the C_{60} bands due to hybridization with so-called nearly-free electron states [87]. For the example of a metallic (10,10) tubes the t_{1u} band was found to cross the Fermi level, leading to the prediction of multicarrier states where four bands cross the Fermi level, two from the SWCNT host and two from the C_{60}. In the case of semiconducting tubes, the t_{1u} band was always pinned at the Fermi level for sufficiently large host tubes. Similar results were found in DFT calculations [85]. In metallic host tubes, the t_{1u} band was always found close to the Fermi level and between 0.2 and 0.4 eV above the Fermi level in semiconducting host tubes. However, one important difference remained compared to the LDA calculations: The t_{1u} band always remained above the Fermi level and never crossed it. This was supported by Raman spectroscopy where it was reported that the t_{1u} level of C_{60} in C_{60} peapods does not lie close to the Fermi level. Also scanning tunneling spectroscopy experiments on C_{60} peapods [83] revealed characteristics in the spectrum originating from the C_{60} filling in the conduction band but not in the valence band. Kane et al. used a tight-binding approach in order to explain these results [88]. The gap, i.e. the distance between the t_{1u} and the h_u band, was retained in their simulation and the C_{60} bands were shifted rigidly through the SWCNT band structure in order to account for the experimental spectra. A good agreement was reached with the t_{1u} band more than 1 eV above the Fermi level, i.e. in total contradiction to the two previously discussed calculations.

Also in C_{60} peapods, doping with electron acceptors or donors can be carried out. Raman measurements on potassium-intercalated C_{60} peapods revealed that, in addition to a charge transfer to the SWCNT pods, the C_{60} peas are also charged up to $C_{60}{}^{-6}$ and form a metallic one-dimensional polymer at high doping levels [89]. In contrast to fullerene intercalation compounds with its line phases, a continuous charge transfer to the SWCNTs and the C_{60} peas as a function of dopant concentration is observed at intermediate doping levels, [90]. The photoemission experiments carried out in Chapter 7 provide an ideal tool to resolve questions concerning the adjustment of the chemical potential and hybridization and will provide an insight into the combined valence band structure of this hybrid compound in the pristine state and upon doping.

3 Experimental methods

Solid-state spectroscopy covers a wide range of techniques and processes owing to the large amount of probe particles available. Photons, electrons, neutrons, positrons, muons as well as neutral and charged atoms can all be used as probes with applications depending on the respective properties of the particle [91]. Most of these particles can also be used in a wide energy range. For instance electromagnetic radiation covers an energy scale between radio frequencies up to γ radiation.

The spectroscopic methods used in the context of this work are among those which are characterized as high-energy spectroscopy. This term is loosely used for spectroscopy with particles at or above the energy of ultraviolet light ($\approx 20\,\mathrm{eV}$) and includes methods such as photoemission spectroscopy, x-ray absorption spectroscopy and electron energy loss spectroscopy. These methods have proven to be extremely useful in a variety of scientific fields but are not very commonly used in the nanotube community, partly because of their high sample quality requirements. The exception is EELS, which contributed significantly to the investigation of structural and electronic properties of pristine and doped SWCNTs and peapods [92–94]. Instead, optical methods such as Raman spectroscopy, optical absorption spectroscopy and photoluminescence spectroscopy dominate carbon nanotube spectroscopy. Their usefulness originates from the close correspondence between the nanotube structure and its electronic properties, in particular their diameter-dependent electronic structure, best expressed in the diameter-dependent gap width between corresponding van Hove-singularities. However, all these methods have drawbacks, e.g. photoluminescence can only be carried out on isolated semiconducting SWCNTs and Raman spectroscopy requires a wide range of laser energies due to the narrow resonance window. It should not be omitted that other characterization methods such as high-resolution TEM and transport measurements play an important role in the nanotube field, the latter especially since individual nanotubes were successfully contacted with electrodes [9]. Some of these transport results will be discussed later.

Recently, the fabrication of high-quality samples allowed the application of well-established high-resolution PES techniques to SWCNTs, resolving the SWCNT fine structure as well as the electron-electron interaction-induced renormalization of the spectral weight at the chemical potential [55]. These advances motivate a further use of photoemission spectroscopy in association with carbon nanotubes. In this chapter, the two high-energy spectroscopy methods used in this thesis – photoemission and x-ray absorption spectroscopy – are introduced on a theoretical and experimental level. They are both based on the interaction of light with the material and imply the emission of electrons. The characteristics of the emitted electrons are ultimately the measure of the sample properties.

3.1 Interaction between light and solid

The basic principle of all spectroscopic methods used for this work is the interaction of solids with light, or more precisely, the interaction of an incoming photon with an electron or phonon in the solid. The different techniques are characterized by the respective process of interaction which can be either elastic or inelastic. Elastic scattering of a photon can excite an electron into the vacuum - the process used for photoemission spectroscopy (PES) - or into unoccupied states - the process used for x-ray absorption spectroscopy (XAS). In both cases, the process starts with the excitation of an electron by a photon emitted from an external light source. In the approximation of first order perturbation theory, i.e. if the perturbation of the system caused by the electromagnetic field of the incoming light is small, this process can be described by Fermi's golden rule as a transition of an electron with transition probability $\mathrm{W_{fi}}$ between the N-particle ground state Ψ_i^N and the N-particle final state Ψ_f^N:

$$W_{fi} \sim \frac{2\pi}{\hbar} \mid \langle \Psi_f^N \mid H^{int} \mid \Psi_i^N \rangle \mid^2 \cdot \delta(E_f^N - E_i^N - \hbar\omega) \tag{3.1}$$

The δ-function signifies energy conservation with the initial and final state energies of the system E_i^N and E_f^N. The probability of a transition between given initial and final states is thus determined by the interaction-Hamiltonian $\mathrm{H^{int}}$, the so-called matrix element. The Hamiltonian of the system in presence of an electromagnetic field can be written as

$$\begin{aligned} H &= \frac{1}{2m}\left(\vec{p} + e\vec{A}(\vec{r},t)\right)^2 + V(\vec{r}) & (3.2)\\ &= \frac{1}{2m}\left(\vec{p}^2 + e\vec{p}\vec{A}(\vec{r},t) + e\vec{A}(\vec{r},t)\vec{p} + e^2\vec{A}^2(\vec{r},t)\right) + V(\vec{r}) \;, & (3.3)\end{aligned}$$

where $\vec{A}(\vec{r},t)$ is the vector potential. With the Hamiltonian of an unperturbed electron $H_0 = p^2/2m + V(\vec{r})$, the Hamiltonian can be written as

$$H = H_0 + H_{\text{int}} \tag{3.4}$$

with

$$H_{\text{int}} = \frac{e}{2m}\left(\vec{p}\vec{A}(\vec{r},t) + \vec{A}(\vec{r},t)\vec{p} + e^2\vec{A}^2(\vec{r},t)\right) \;. \tag{3.5}$$

The term quadratic in the vectorpotential can be neglected if the perturbation is small. Furthermore the dipole approximation can be used. It is assumed that the distance over which the electromagnetic field varies is large compared to the excited volume. In this case

$$\vec{p}\vec{A} \sim \frac{\partial}{\partial\vec{r}}\vec{A} \approx 0 \;, \tag{3.6}$$

so that H_{int} simplifies to

$$H_{\text{int}} \sim \vec{A}\cdot\vec{p} \sim \vec{e}\cdot\vec{r} \;, \tag{3.7}$$

where $\vec{e}$ is the unit vector along the polarization direction. The resulting transition probability is therefore

$$W_{fi} \sim \frac{2\pi}{\hbar} \mid \langle \Psi_f^N \mid \vec{e}\cdot\vec{r} \mid \Psi_{\mathrm{i}}^{\mathrm{N}} \rangle \mid^2 \cdot \delta(\mathrm{E_f^N} - \mathrm{E_i^N} - \hbar\omega) \;. \tag{3.8}$$

The key difference between photoemission and x-ray absorption spectroscopy is in the final state. In PES, the final state is situated above the vacuum level and the electron has the parabolic free-electron dispersion, while in XAS, the final state is a conduction band state with the dispersion given by the actual band structure.

3.2 Photoemission spectroscopy

3.2.1 Theoretical description

Basic principle

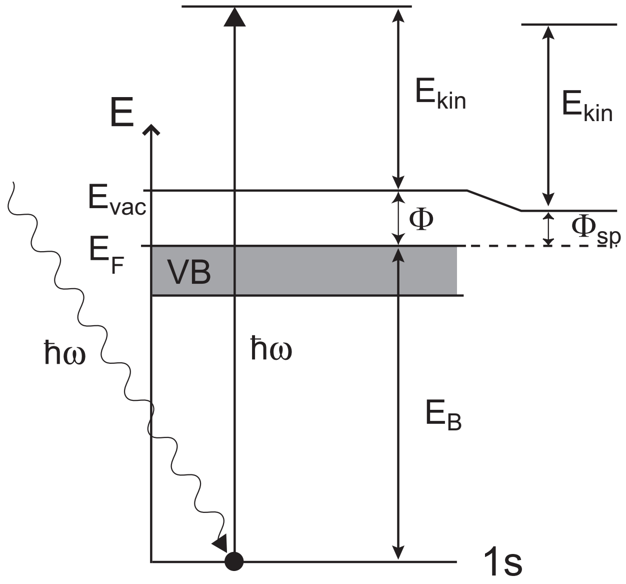

Figure 3.1: Schematic representation of the photoemission process. Left: Excitation of an electron into vacuum. Right: Energy scheme.

Photoemission spectroscopy (PES) is based on the photoelectric effect discovered by Hertz in 1887 [95] and explained by Einstein in 1905 [96]. When a photon impinges a solid it can transfer its energy $\hbar\omega$ to an electron in the solid. If the energy of the incoming photon is high enough, the electron leaves the solid. Such an electron is called photoelectron. Fig. 3.1 illustrates this effect. The important attribute of this process is that the kinetic energy of the escaping electron only depends on its binding energy E_B in the sample. The resulting kinetic energy E_{kin} is

$$E_{\text{kin}} = \hbar\omega - E_B - \Phi, \tag{3.9}$$

where $\hbar\omega$ is the energy of the incoming photon and Φ is the work function, i.e. the difference between the Fermi energy and the vacuum level. In a real photoemission experiment the electron has to enter an analyzer where its kinetic energy is measured. Therefore it has to overcome a contact potential $\Phi_{\text{sp}} - \Phi$, where Φ_{sp} is the work function of the analyzer as is depicted on the right hand side of Fig. 3.1. If one subtracts $\Phi_{\text{sp}} - \Phi$ from Eq. 3.9 the formula remains the same but with Φ_{sp} in the place of Φ.

The system is excited with monochromatic light so that the photon energy $\hbar\omega$ is known. The work function Φ can be determined by measuring the Fermi edge of a metal. Thus, with $\hbar\omega$ and Φ known, the kinetic energy of the photoelectron depends solely on its binding energy in the sample and the binding energy can easily be obtained by applying equation 3.9. Simply speaking, the distribution of kinetic energies of the electrons which leave the sample corresponds directly to the electronic density of states in the sample. This is illustrated in Fig. 3.2. The actual response is also weighted with the transition probabilities as will be explained below.

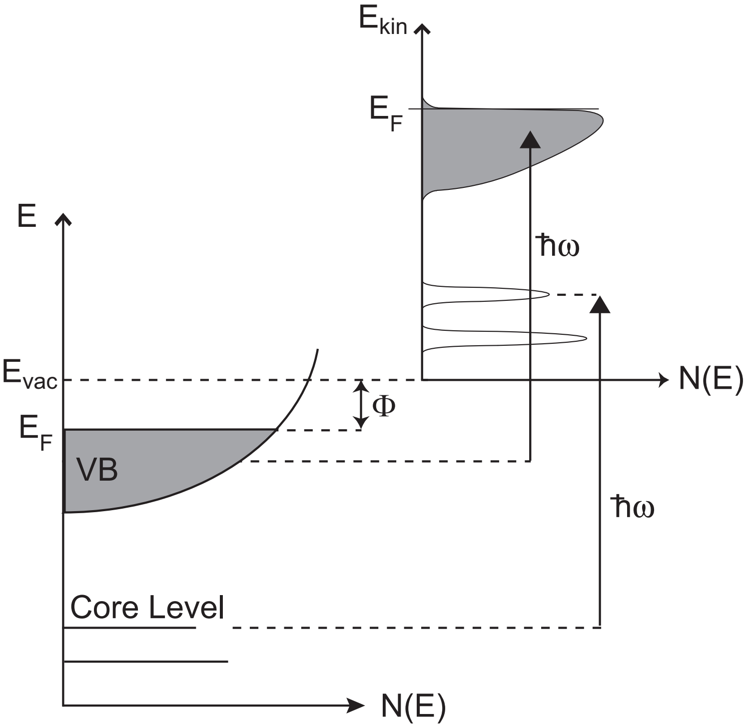

Figure 3.2: Illustration of how the electronic density of states in the sample is projected on the kinetic energy distribution of the photoelectrons. Electrons in the occupied states (shaded area) become detectable if they are excited above the vacuum level with electrons at energy $\hbar\omega$.

Three-step model

The three-step model is commonly used to describe the photoemission process [97]. The model is purely phenomenological but has nonetheless proven successful. The model divides the complicated photoemission process into three steps each, of which can be treated individually:

1.) Optical excitation

A bound electron absorbs a photon and is optically excited from an occupied state into an unoccupied state above the Fermi level. This process happens either without momentum transfer or with a momentum transfer equal to a reciprocal lattice vector which is represented by a vertical transition in the reduced zone scheme of the band structure. The momentum of the photon is neglected here. For instance, the momentum transfer for a photon with the energy $\hbar\omega = 20$ eV, is 0.01 Å^{-1}, which is small compared to the first Brillouin zone of SWCNTs. This step contains all information about the intrinsic electronic structure of the material.

2.) Travel to the surface

After being excited into an unoccupied state above the Fermi level the electron has to travel to the sample surface. While travelling it can undergo scattering processes, mainly with other electrons or phonons. The number of scattering events which occur before the surface is reached is determined by the distance to the surface and the mean free path. The mean free path of electrons is very small, only a few Å for electrons with kinetic energies in the range of interest, i.e. between about 10 and 1500 eV. Thus only electrons which come from within a few Å of the surface can leave the sample without additional scattering.

The electrons which undergo scattering processes either do not leave the sample at all or contribute to the background. Only in a few cases can additional information be obtained from such electrons. The so-called satellites which can be observed in XPS are one example. They are related to energy losses of electrons upon leaving the sample, eg. through the excitation of a plasmon. Such effects in the photoemission spectrum of the C1s core level of SWCNTs are discussed below.

2.) Escape of the electron into vacuum

Finally the electrons have to overcome the potential barrier at the surface manifested by the work function. They can leave the sample if their momentum perpendicular to the surface is large enough, otherwise they are reflected back into the sample. Outside the sample the electron energy dispersion is that of a free electron and is given by the parabola $E = p^2/2m$. Equation 3.9 represents the energy conservation law of the photoemission process. But naturally momentum conservation also applies to the photoemission process. Due to the potential barrier, the momentum perpendicular to the surface is not conserved while the momentum parallel to the sample surface is conserved. This fact is used in angle-resolved photoemission spectroscopy (ARPES), where not only the kinetic energy but also its emission angle to the surface, i.e. its momentum, is measured. In principle, it is possible to obtain the complete band structure of the occupied states with ARPES and the method is widely used e.g. in the investigation of the electronic structure of high-T_C superconductors with their two-dimensional structure. For such structures, the momentum parallel to the surface corresponds to the wavenumber of the initial state $k_\parallel$ of the electron:

$$k_\parallel = \frac{1}{\hbar} p_\parallel = \sqrt{\frac{2m_e E_{kin}}{\hbar^2}} \cdot \sin\theta \tag{3.10}$$

Although the instrumentation used in this work would allow such investigations, ARPES cannot be applied to carbon nanotubes as to date macroscopic samples of the purity required always consist of randomly oriented tubes rendering a direction-dependent investigation impossible. However, new developments in nanotube fabrication by CVD led to the successful growth of macroscopically aligned SWCNTs. Growth of such samples with high purity and a narrow diameter distribution could make angle-resolved PES on SWCNTs possible.

Theoretical description

It was shown above that under certain approximations the transition probability between an N-particle initial state and an N-particle final state is given by Fermi's golden rule and an interaction Hamiltonian $H_{int} \sim \vec{e} \cdot \vec{r}$ (see Eq. (3.8)). In photoemission spectroscopy, the initial and final state are given by $E_i^N = E_i^{N-1} + E_B$ and $E_f^N = E_f^{N-1} + E_{kin}$ respectively. The quantity accessible in PES experiments is the photoemission intensity $I(\vec{k}, E_{kin})$, which is proportional to the sum of all possible combinations of initial and final states:

$$I(\vec{k}, E_{kin}) \sim \sum_{i,f} \frac{2\pi}{\hbar} \mid \langle \Psi_f^N \mid H^{int} \mid \Psi_i^N \rangle \mid^2 \cdot \delta(E_f^N - E_i^N - \hbar\omega) \ . \tag{3.11}$$

If one assumes that the photoelectron leaves the sample quickly enough to avoid post-collisional interaction with the system left behind (*sudden approximation*), the N-particle final state can be factorized into

$$\Psi_f^N = A \Phi_f^k \Psi_f^{N-1} \ , \tag{3.12}$$

where A is the antisymmetric operator which assures the fermionic character of Ψ_f^N. Φ_f^k is the wavefunction of the photoelectron Φ_f^k. If one further assumes that Ψ_i^N is a single Slater determinant, the initial state can equally be factorized into a product of a one-electron orbital Φ_i^k and the remaining $N-1$-particle system Ψ_f^{N-1}, again using the antisymmetric operator A:

$$\Psi_i^N = A \Phi_i^k \Psi_i^{N-1} \ . \tag{3.13}$$

This factorization transforms Eq. (3.11) to

$$I(\vec{k}, E_{kin}) \sim \sum_{i,f} |M_{i,f}^k|^2 \sum_m |\langle \Psi_{f,m}^{N-1} \mid \Psi_i^{N-1} \rangle|^2 \cdot \delta(E_f^N - E_i^N - \hbar\omega) \ , \tag{3.14}$$

where $|M_{i,f}^k| \equiv |\langle \Phi_f^k | H_{int} | \Phi_i^k \rangle$ are the one-electron dipole matrix elements. The second sum runs over all m final eigenstates of the $(N-1)$ final state. It can be shown that this is equivalent to [98]

$$I(\vec{k}, E_{kin}) \sim \sum_{i,f} |M_{i,f}^k|^2 \, A(\vec{k}, E) \, f(E) \ , \tag{3.15}$$

with $E = E_B = \hbar\omega - E_{kin} - \Phi$, the spectral function $A(\vec{k}, E)$ and the Fermi function $f(E)$. The spectral function contains the desired information on the electron system. The photoemission response is thus the matrix element-weighted density of states of the system.

Auger process

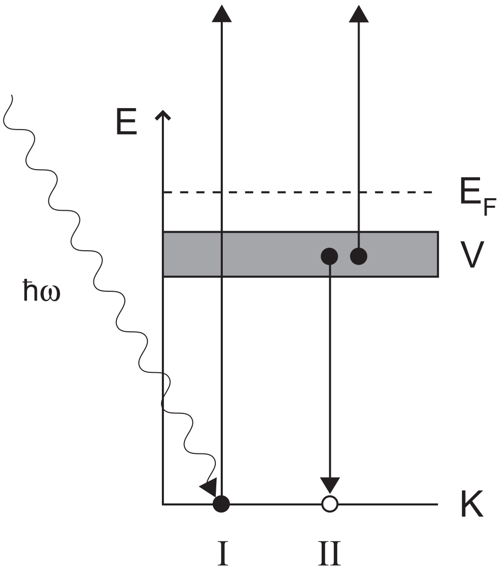

Figure 3.3: Schematic representation of the KVV Auger process. First, an incident photon creates a hole in the K shell (i.e. a 1s state). In a second step this core hole is filled by an electron from the valence band (V) thereby reducing its potential energy. This excess energy is transferred to a second electron in the valence band causing it to leave the sample.

Apart from the photoelectrons, incident light can cause electrons to leave the sample by means of the Auger process. In this process, the incoming light creates a core hole which is subsequently filled by an electron from higher states such as the valence band. The excess energy is transferred to a second electron in a state close to that of the electron filling the core hole, causing the second electron to leave the sample. The kinetic energy of the emitted electron does not depend on the energy of the incident light but only on the level configuration of the Auger process. This means that electrons e.g. from a KVV Auger process (a hole in the 1s state (K) is filled with an electron from the valence band (V)

Light source	Energy
XPS:	
Al Kα X-ray anode	1486.6 eV
Mg Kα X-ray anode	1253.6 eV
UPS:	
Helium discharge lamp (He I)	21.22 eV
Helium discharge lamp (He II)	40.8 eV
Synchrotron radiation	few eV - few keV
BESSY UE52-PGM	90- 900 eV

Table 3.1: Light sources typically used for photoemission spectroscopy.

leading to the emission of a second electron from the valence band (V)) always have the same kinetic energy regardless of the incoming light, provided that the light has enough energy to create the core hole. The Auger process is also a relaxation process of the excited state in the conduction band created by the incoming photon in x-ray absorption spectroscopy (see below).

3.2.2 Instrumentation and experimental setup

There are three experimental requirements crucial for a successful photoemission experiment:

- A monochromatic light source with high intensity and – if only small samples are available – a small spot size.
- An electron energy analyzer with the highest possible energy resolution.
- An ultra-high vacuum (UHV) set-up due to the surface sensitivity of the method.

In addition, if angle-resolved measurements are desired, good control of electron emission angles, i.e. a sample holder (manipulator) which can accurately be moved in as many degrees of freedom as possible, is needed. These requirements can be met, although at times only with considerable effort and will be discussed below. An illustration of the experimental setup is given in Fig. 3.4.

Light sources: XPS and UPS

Photoemission spectroscopy is further classified according to the excitation energy, i.e. the energy of the incoming light. As demonstrated by the above theoretical description of the process, monochromatic light is needed for PES. In x-ray photoemission spectroscopy (XPS), radiation with photon energies of several hundred eV is used. Most often, an x-ray anode is used for its generation. Here, electrons are accelerated at high voltage onto a metallic anode where the electrons ionize core levels which are filled with electrons emitting the characteristic x-ray radiation in the process. The most common anode materials are aluminum and magnesium, where in both cases the Kα emission is the strongest. The respective values of the photon energy are given in Tab. 3.2.2. Its high photon energy makes XPS suitable for core level investigations. The core level binding energies are element-specific which means that XPS is well suited for determining the sample composition. Furthermore, the exact binding energy depends on the binding configuration of the respective atom. Chemical shifts of the core states with respect to their position in the pure (crystalline) material occur if the atom is for example situated in a molecule. The actual amount of the chemical shift depends on the bonding to the neighboring atoms, thus making XPS useful for the investigation of molecules by resolving the bonding configuration.

In addition, some information can be obtained from an analysis of the line shapes of the core level and Auger response as will be discussed in the following chapter on the electronic properties of pristine SWCNTs. In the present experiments, Al Kα radiation ($\hbar\omega$ = 1486.6 eV) was used. It was also monochromatized using a quartz crystal monochromator, which reduces the x-ray bandwidth to 0.4 eV. Nevertheless this leads to a resolution which is too low for a detailed valence band investigation. Since also the cross section with the low binding energy valence band states is rather low, ultraviolet photoemission spectroscopy (UPS) is better suited for high-resolution valence band investigations. Here, the light is produced by a helium discharge lamp. The photons are generated by transitions in the electron cloud of excited helium atoms (ions). Excitation and ionization are caused by the impact of highly energetic electrons. Depending on the helium pressure inside the discharge lamp, the spectrum is dominated by $He\ 2p \rightarrow He\ 1s$-transitions ($\hbar\omega$=21.22 eV) or $He^{+}2p \rightarrow He^{+}1s$-transitions ($\hbar\omega$=40.8 eV). The desired energy is chosen by rotating a plane-grating mirror in front of the lamp. The bandwidth of the monochromatized light from the He discharge lamp is less than 1 meV at 21.22 eV excitation energy.

Synchrotron facilities can produce light over a wide energy range, from the soft x-ray range of several hundred eV down to light with only a few eV. It can thus be used for both core level and valence band investigations. It also has a high intensity, a small spot size and can be generated with all kinds of polarizations with nearly continuous variation of the photon energy. A description of how synchrotron radiation is generated is given below in the chapter on x-ray absorption spectroscopy.

Analyzer and detector

There are various methods for determining an electron's kinetic energy [99] e.g. by using resonances in a scattering process or the time-of-flight method. The deceleration of the particles by a retarding field or the change of the orbit of a particle by an electric or magnetic field is better suited for PES. All modern electron energy analyzers rely on the latter principle. Such analyzers are most often constructed from two cylinders or hemispheres with different radii which are arranged as capacitors. A hemispherical analyzer is schematically depicted in Fig. 3.4: The electron enters the analyzer through an entrance slit and if a potential difference ΔV is then applied between the two components, only electrons with a certain range of energies can pass through the capacitor. These are the electrons whose curve radius at this certain voltage matches the radius of the analyzer. By changing the voltage between the analyzer walls, the kinetic energy of the electrons which can pass the analyzer can be varied. The electrons are detected via the photocurrent or by their impact on a micro-channel plate (MCP) detector.

The Gammadata Scienta SES 200 analyzer used in the PES experiments presented in this thesis is a hemispherical deflection analyzer specifically designed for angle-resolved PES. It provides an energy resolution of better than 10 meV in the UPS regime. The electrons are detected with an MCP detector consisting of an array of micrometer-wide miniature electron multiplier channels which register the spatial distribution of the incoming electrons. This

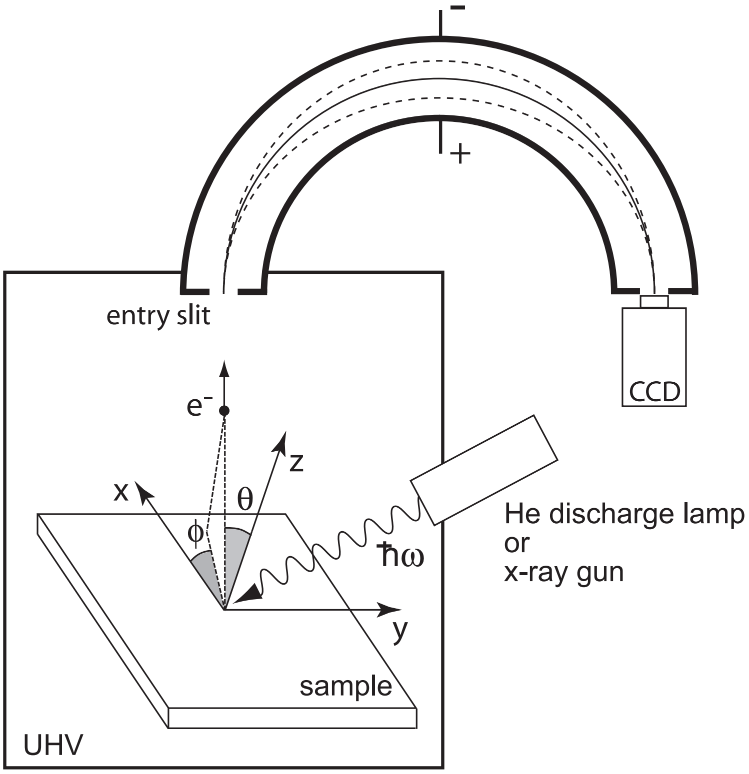

Figure 3.4: Illustration of the experimental setup. The sample is kept in ultra-high vacuum (UHV) and irradiated with high-energy photons from an x-ray source or low energy photons from a helium discharge lamp. The photoelectrons are emitted under a polar angle ϕ and an azimuthal angle θ and enter the analyzer through the entry slit. As a result of the voltage applied between the two analyzer spheres, the electrons describe a curve. Electrons with a certain energy which depends on the voltage between the spheres can pass the analyzer and are detected with a CCD camera.

setup not only allows the measurement of the kinetic energy of the photoelectrons but also their emission angle (angular mode) or their emission location (transmission mode) respectively. Using the latter mode guarantees that no signal from the sample holder or the Tantalum clamps is registered if the light spot and the region from which electrons are detected is bigger than the sample. The sample borders can be identified on the CCD image of the MCP and can be excluded from the measurements by either better adjusting the sample or simply excluding the region from the measurements.

Surface sensitivity and UHV system

As discussed above, the mean free path of electrons with kinetic energies typical for photoemission is only a few Å. Not only does this make PES very surface sensitive concerning the sample, it also means that PES is very sensitive to contaminations of the surface. Such contaminations can also come from atoms and molecules in the air. Therefore PES experiments have to be carried out in vacuum. Given that the sample is clean when transferred into vacuum, the time t in seconds in which one monolayer is deposited on a given surface area at a pressure p in mbar and a sticking coefficient $0 \leq S \leq 1$, is given by [100]:

$$t = \frac{3.8 \cdot 10^{-6}}{p \cdot S} \text{ mbar s} . \tag{3.16}$$

Assuming a sticking coefficient $S = 1$ and a pressure $p = 10^{-6}$ mbar, one monolayer is deposited on the surface within 4 seconds. For the experiments a much longer time frame is required. Thus ultra-high vacuum, with pressures in the range of $1 \cdot 10^{-10}$ mbar is needed.

The UHV system used allows convenient introduction of the sample through a fast-entry lock. The sample can then be transferred in UHV into a manipulator in a preparation chamber where the sample can be heated and into the manipulator used for the measurement.

Sample handling and manipulator

The sample is kept in UHV for the duration of the experiment, including the intercalation steps. The system used in the IFW allows convenient introduction of the sample into UHV through a fast-entry lock. The sample can then be transferred into a preparation chamber under UHV conditions where it can be heated up to 500° C. Heating is necessary to remove contaminations from the sample. The preparation chamber can also be used to evaporate C_{60} on the sample.

For the photoemission experiments, the sample is transferred into the manipulator situated in the measurement chamber. This purpose-built manipulator is specifically designed for angle-resolved photoemission. It has six degrees of freedom (xyz movement as well as polar, azimuthal and tilt rotation). However, all experiments in this thesis are angle-integrated with the electron emission angle normal to the sample surface. Furthermore, the manipulator is equipped with a He flow cryostat allowing the sample to be cooled down to 35 K, the temperature at which the PES experiments in this thesis were carried out.

Determination of the work function

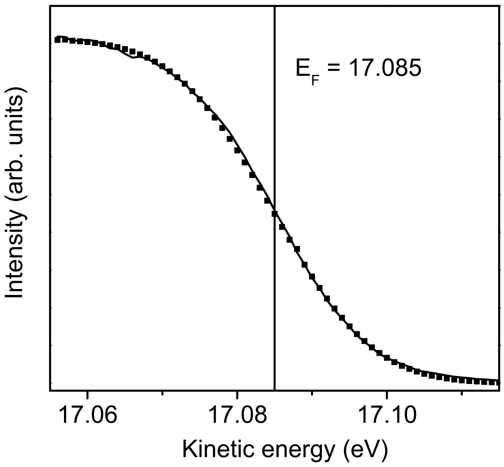

Figure 3.5: UPS spectrum ($\hbar\omega$ = 21.21 eV) of the Fermi edge of Tantalum at T = 35 K (squares) and its fit to a Fermi function including resolution and temperature broadening (solid line).

In Eq. (3.9), all contributions are determined by the energies of the participating particles with the exception of the work function Φ. Φ has to be determined in the experiment.

This can be achieved by measuring the kinetic energy of electrons with zero binding energy, i.e. those at the Fermi level of a metal. Fig. 3.5 depicts such a spectrum for Tantalum at T = 35 K. The Fermi edge can be identified. In order to obtain the Fermi level value, the spectrum was fitted with a Fermi function convoluted with a Gaussian for the finite resolution. The parameters for this fit were the kinetic energy of the Fermi level and the resolution broadening while the broadening of the Fermi function due to finite temperature was fixed with the corresponding value. The resulting resolution is 0.011 eV and the Fermi level was found at 17.09 eV. Incorporating the excitation energy of $\hbar\omega = 21.21$ eV, the work function results as $\Phi = 4.12\,\mathrm{eV}$. Using this value, all spectra obtained in the following chapters can be transferred accurately from the kinetic energy representation into the binding energy scheme. In addition it was verified that a very high resolution can be achieved in UPS.

3.3 X-ray absorption spectroscopy

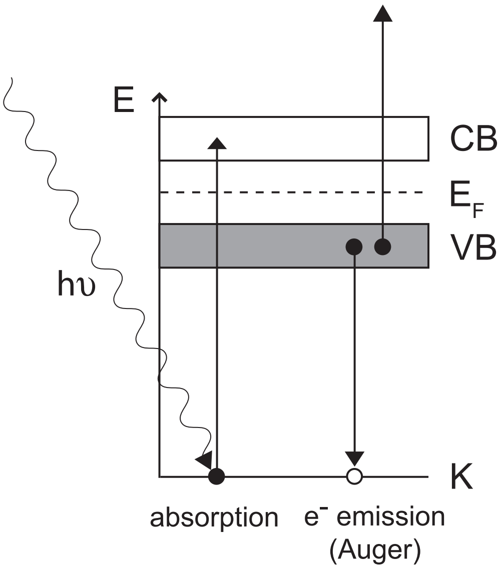

Figure 3.6: Schematic representation of the x-ray absorption process. An electron is excited from the core level into an occupied state in the conduction band if the energy of the incoming photon matches the energy difference between these two states. In the case of carbon, the core hole is predominantly filled via an Auger process which leads to the emission of an electron.

Basic principle

By means of x-ray absorption spectroscopy the matrix element-weighted unoccupied density of states can be probed. Monochromatic light impinges on a sample and excites electrons from the core states into unoccupied states in the conduction band as shown on the left hand side of Fig. 3.3. Absorption takes place when the photon energy matches the energy difference between core state and conduction band. XAS thus measures the convolution of the density of states of the core level with the unoccupied states weighted with the dipole operator under observance of the dipole selection rules ($\Delta l = \pm 1$ with the angular momentum number l) . If the core hole state can be modelled by a δ-function, XAS directly probes the conduction band. However, the final state is strongly influenced by the core hole, leading to a deviation from the ground state conduction band as will be discussed based on the respective spectra.

The absorption process itself is indirectly measured via the decay of the excitation, i.e. via the process which leads to a filling of the core hole created by the incoming light. There are two possible processes involved: First, the excited electron can fall back into its original state in the core level, emitting a photon in the process. These photons are detected in fluorescence spectroscopy. Second, the core hole can be filled by an Auger process (see above) which causes the emission of an electron as depicted on the right hand side of Fig. 3.3. In this thesis, the latter process, which is also the dominant process in lighter elements like carbon, is used. The number of electrons emitted corresponds to the degree of absorption of the incoming light. It can be measured by either measuring the current which flows from the ground to the sample in order to compensate for the electrons which have left the sample (total electron yield, TEY) or by directly detecting the electrons emitted from the sample using a partial yield detector (PYD), which allows the application of a retarding potential to filter out the background from secondary electrons.

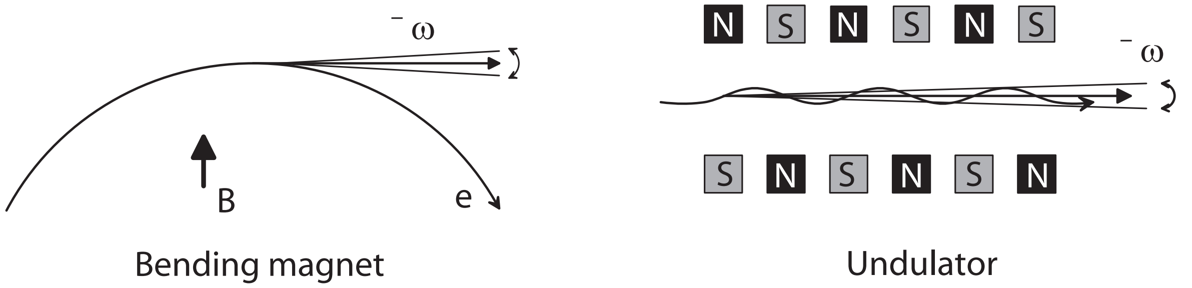

Figure 3.7: Schematic representation of the synchrotron light emission principle. **Left panel:** Emission from electrons on a circular trajectory caused by a magnetic field. **Right panel:** Emission caused by an undulator consisting of permanent magnets of alternating polarization.

Synchrotron radiation

The absorption spectrum is acquired by probing the absorption over a certain range of excitation energies. XAS experiments thus require light sources which are continuously tunable in the required energy range. Such light is produced by synchrotrons. Synchrotron radiation is the electric field emitted from charged particles (e.g. electrons), which travel at relativistic speeds in circular accelerators (see left panel of Fig. 3.7). The light beam is emitted in the direction tangential to the electron path.

Only in the first and second generation was this light actually used for experiments. Synchrotron radiation of the third generation is generated by undulators. The right panel of Fig. 3.7 shows that undulators consist of two sets of permanent magnets, each with alternating directions of the magnetization. The electrons which fly through such an undulator encounter a spatially periodic magnetic field which causes them to “wiggle” perpendicular to their moving direction and in this process leading to the emission of light in the direction tangential to the accelerator ring. The wavelength and polarization of the emitted light can be adjusted by changing the vertical gap between the sets of magnets and by shifting the magnets in the horizontal direction.

The emitted light requires monochromatization which is done by a plane grating monochromator (PGM). The energy of the reflected light can be set according to Bragg’s law by rotating the grating. Synchrotron radiation has significant advantages compared to conventional laboratory light sources. The emitted light has a much higher brilliance and photon flux, and most importantly, the photon energy can be tuned over a wide range of energies with any polarization. The XAS experiments presented in this work were performed at the UE-52 PGM beamline at BESSY II. The specifications for this beamline are given in Tab. 3.2.

Beamline	Monochromator	Energy range	Resolving power $\Delta E/E$	Polarization	Spot size
UE52-PGM	Plane grating mirror	90 - 900 eV	$> 1 \cdot 10^4$	circular or linear	$< 1\,\text{mm}^2$

Table 3.2: Specifications of the UE52-PGM beamline at BESSY.

3.4 Sample preparation and characterization

The samples investigated in this work were produced and purified by H. Kataura using the laser vaporization method and a NiCo catalyst. This method allows the SWCNT mean diameter to be controlled to a certain extent by varying the furnace temperature. Samples with a narrow diameter distribution are usually obtained [33].

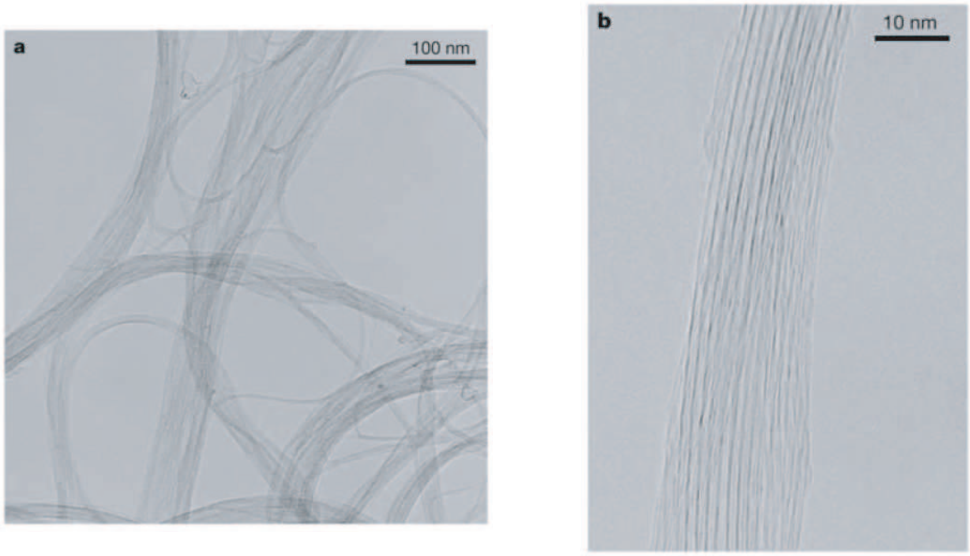

Figure 3.8: High-resolution TEM micrographs of the SWCNT samples provided by H. Kataura. **Left panel:** Random arrangement of SWCNT bundles. **Right panel:** A SWCNT bundle. Figures from [55].

Sample characterization

Before the SWCNTs are prepared for the photoemission experiments, their structural properties have to be determined. An apparent way to investigate SWCNT samples is high-resolution transmission electron microscopy (TEM), which provides atomical resolution. Nanotubes were indeed discovered by electron microscopy [3]. Fig. 3.8 shows two TEM micrographs. The left panel shows a SWCNT sample at a scale of tens of nanometers. Individual tubes can be observed and it becomes apparent that they are arranged in bundles. In these bundles the tubes are held together by van der Waals interactions. In the right panel of Fig. 3.8 this becomes even clearer. The bundles have a hexagonal structure perpendicular to the tube axis. This has been verified by diffraction experiments [41]. However it is very difficult and time-consuming to obtain macroscopic properties of the nanotube sample such as purity, mean diameter and diameter distribution width from electron microscopy since only small sections of the sample can be analyzed and a large number of tubes has to investigated for statistically reliable information.

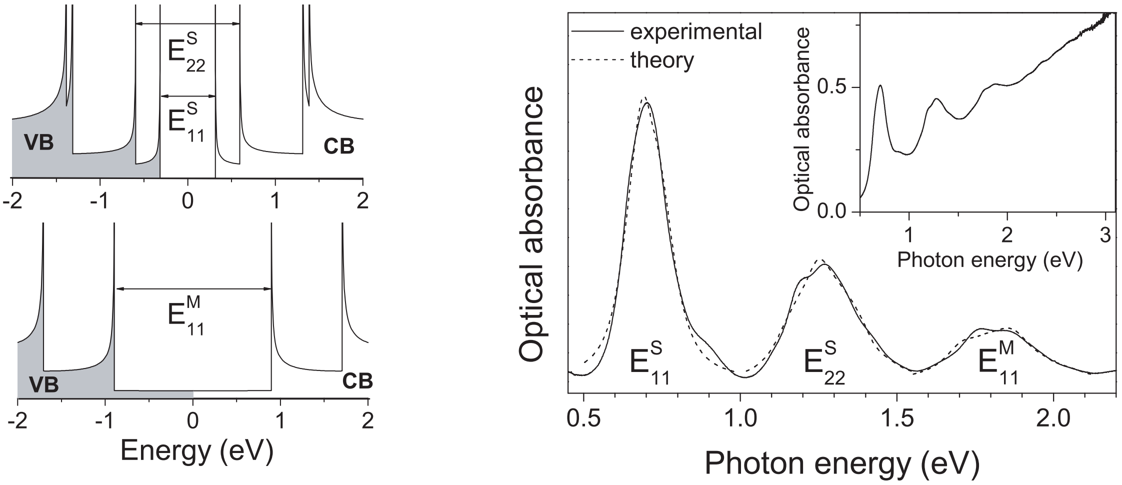

Figure 3.9: Left panel: Density of states of a semiconducting (upper) and metallic (lower) tube. The arrows between the van-Hove singularities in valence and conduction bands indicate the transitions which lead to strong absorption and are labelled correspondingly. **Right panel:** Measured optical absorption of a SWCNT sample with an already subtracted background. The solid line is the measured curve, the dashed lines are theoretical simulations of the respective peaks based on a tight-binding model. The inset shows the spectrum as-measured, i.e. without background subtraction [62].

An easier way to characterize a SWCNT sample in terms of mean diameter and diameter distribution is optical absorption spectroscopy (OAS). In this method, the wavelength-dependent absorption of a thin SWCNT film is measured. The absorption is dominated by the transitions between two corresponding van-Hove singularities in the valence and conduction band as shown in the left panel of Fig. 3.9. The inset in the right panel of Fig. 3.9 shows a typical absorption spectrum of a sample very similar to those used in this work. Three peaks originating from absorption between the vHs can easily be identified.

Quantitative information on the sample can be obtained if the background is subtracted (right panel of Fig. 3.9). The gap energy, i.e. the distance between the corresponding vHs in the valence and conduction band, is inversly proportional to the tube diameter as

$$E_{ii}^S = \frac{2ia_0\gamma_0}{d} \quad \text{and} \quad E_{ii}^M = \frac{6ia_0\gamma_0}{d}. \tag{3.17}$$

Assuming realistic experimental conditions and a Gaussian diameter distribution, the absorption profile of a bulk SWCNT sample can be expressed as

$$I(E) = f \sum_{n,m} \exp[\frac{-(d_{n,m}-\bar{d})^2}{2(\Delta d)^2}] \frac{w}{(E-E_{ii})^2+(w/2)^2}, \tag{3.18}$$

where f is an arbitrary scaling factor and w (Approx. 40 meV) describes the broadening of each single transition due to finite lifetime of the interband transitions and the finite resolution of the spectrometer [62]. The E_{ii} are the energy separation between corresponding vHs of tubes with the diameter $d_{n,m}$. The absorption spectrum (with background subtracted) can now simply be fitted using the mean diameter $\bar{d}$ and the distribution width Δd as parameters. The dashed line in the right panel of Fig. 3.9 depicts the absorption profile obtained from this model using a mean diameter of 1.37 nm and a distribution width $\bar{d} = 0.08\,\text{nm}$.

Sample preparation

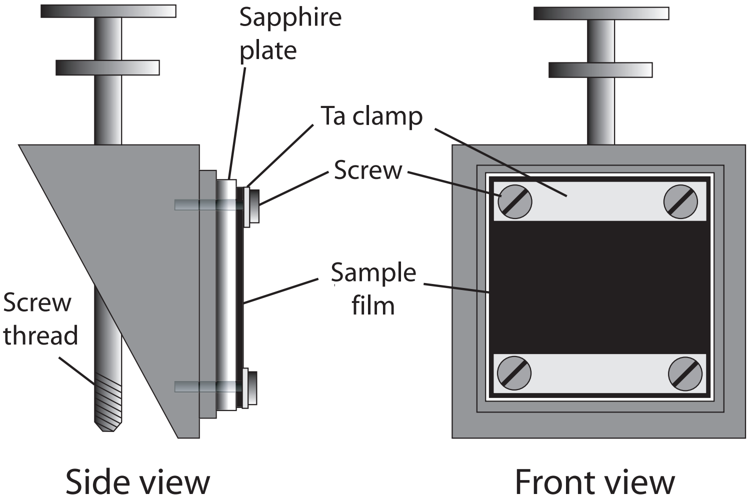

Figure 3.10: Schematic representation of the sample mounted on a PES and XAS sample holder. The sample film is situated on a sapphire plate. Electric contact between sample and sample holder is established via the Tantalum clamps and the screws.

The sample is provided as buckypaper, which is the result of filtration of the nanotube material after purification. Initial doping experiments revealed that the highest doping levels cannot be reached with a bucky-paper sample. The amount of nanotubes is simply too big and potassium which is evaporated on the sample diffuses into the bulk upon equilibration. In order to prevent this, we produced films similar to those used for optical absorption and electron energy loss spectroscopy only thick enough to prevent a signal from the substrate in photoemission experiments. The sample material was sonicated in acetone and then subsequently dropped on an NaCl crystal on a hot plate. The film was then floated off in distilled water. The water bath was changed several times in order to avoid contaminations with NaCl. Finally, the film was captured with a sapphire plate of 7x7 mm^2 size, dried and mounted on a sample holder. For photoemission experiments electrical contact between sample and sample holder is needed to prevent charging of the sample which is caused by the electrons leaving the sample due to the photoelectric effect. Fig. 3.10 shows a schematic representation of the sample holder. It illustrates how electrical contact is established by mounting the sample with two tantalum clamps which at the same time fix the sample to the sample holder. The sample holders can be heated either in a heatable manipulator situated in a different chamber of the vacuum system or with an electron beam gun. The latter allows the sample to be flashed, i.e. quickly heating it up to high temperatures for a short time by electron bombardment. Heat treatment is required to obtain clean samples as will be discussed below.

Potassium Doping

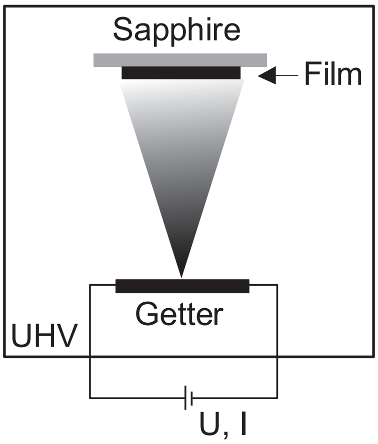

Figure 3.11: Schematic illustration of the potassium doping process. A current through the getter activates the alkali metal evaporation onto the sample which is situated on a sapphire substrate. The whole process takes place under UHV conditions.

Intercalation with alkali metals is a common method to modify the electronic structure of materials, in particular with carbon compounds. Often the sample is put into a quartz tube together with the intercalant and the doping is done by heating the intercalant. In this thesis the samples were doped with potassium. In this case it is much easier to use commercial SAES getters which can be installed inside the UHV chamber so that a series of doping steps can be carried out without exposing the sample to air. The getters consist of a chromate and reducing agent mixture which is kept within a nichrome metal container which has a slit to allow evaporation of the alkali metal. Heating by applying a bias of several amperes activates the alkali metal dispensers and causes the potassium to evaporate. Fig. 3.11 schematically illustrates the setup. The amount of evaporated potassium can be controlled by the bias current, the distance between sample and getters and the time of evaporation which is typically several minutes. Right after the evaporation the potassium is mainly situated on the sample surface. Upon heating, it diffuses into the sample. An equilibration of at least one hour at 150°C ensures homogeneous distribution of potassium over the probed region.

Fabrication of C_{60} peapods

For the fabrication of a C_{60} peapod sample, a SWCNT film was prepared in the same way as described above and transferred into UHV. The C_{60} material was filled into a crucible which was put in an evaporator mounted to the UHV preparation chamber. The C_{60} material was degassed in the vacuum chamber for several hours. It was then evaporated onto the SWCNT film at approximately 500°C until a film of C_{60} was visible on the sample surface. The sample was then equilibrated at 300°C for 12 h, and finally the remaining C_{60} was removed by heating the sample to 500°C. In order to guarantee an optimum filling, this procedure was repeated once.

Overall, this *in situ* method enables the preparation of C_{60} peapods using the established preparation of clean SWCNT samples and then filling them efficiently with C_{60} in UHV without exposing the sample to air. This results in very clean C_{60} peapod samples. In addition, a very high filling ratio close to the optimum can be reached, as can be judged from Raman measurements on double-wall carbon nanotubes (DWCNT) from identically prepared C_{60} peapods. In order to estimate the filling ratio, double-wall carbon nanotubes are prepared on the basis of the C_{60} peapods by simply annealing them for several hours at 1100°C. The C_{60} molecules coalesce and form an additional inner tube inside the original nanotube [101]. The radial breathing mode response from the outer and inner tubes can easily be distinguished and their intensity ratio holds as an estimate for the amount of C_{60} molecules inside the nanotube before annealing.

4 Electrons in one and three dimensions

One central point of this thesis is the nature of the metallic ground state in bundles of single-wall carbon nanotubes and C_{60} peapods. Since carbon nanotubes are ideal one-dimensional systems, their properties should deviate from classical three-dimensional systems. This was already revealed by the emergence of the van-Hove singularities, a fingerprint for one-dimensional systems. Another point concerns the metallic ground state. In a macroscopic sample approximately one third of all tubes are metallic. Furthermore, electron-electron interactions play an important role in SWCNTs [102]. Voit [103] summarizes the major difference between a three-dimensional and a one-dimensional metallic electron system as follows:

- The correlations in a **three-dimensional** electron system are weak although the interactions may be strong.
- In a **one-dimensional** electron system correlations are strong, even for weak interactions.

This already implies that Landau's Fermi liquid theory does not apply in one dimension. A one-dimensional metal can instead be described as a Tomonaga-Luttinger liquid (TLL) whose properties differ importantly from those of a 3D metal. The aim of this chapter is not to reproduce the respective theories of one- and three-dimensional electron liquids but rather to explain the resulting phenomenology.

Therefore, the main features of both, a free and an interacting Fermion system in three dimensions will be discussed in this chapter. It will be explained how the quasiparticle-picture for interacting electrons in 3D breaks down in 1D and how the problem is treated instead by TLL theory. Previous results on SWCNTs and MWCNTs dealing with this issue are reviewed.

4.1 Fermi gas and Fermi liquid

The problem of electrons in a solid can be treated at various levels of difficulty. Interestingly, even the simplest models are rather successful in describing some of the properties of metals. The Drude model, for example, is based on kinetic gas theory of free electrons and was developed without the knowledge of quantum mechanics with its important consequences like the Pauli principle. Still it describes the thermal conduction of metals and the Wiedemann-Frantz law well, primarily because some of its main failures cancel each other out. Other aspects, such as the specific heat, could not be explained [104].

Sommerfeld model

The next step in the evolution of the theory of electrons in a solid was Sommerfeld's model. It still relies on the assumption that the electrons neither interact with the lattice potential nor with the other electrons but includes quantum-mechanical considerations, i.e. is only semi-classical. The potential is modelled by a three-dimensional box with the volume $V = L^3$. The solutions of the Schrödinger equation for a single particle are thus plane waves $\Psi(\overrightarrow{r}) \sim e^{i\overrightarrow{k}\overrightarrow{r}}$ with the free electron dispersion $E = \hbar k^2/2m$. Due to the periodic boundary conditions imposed by the finite length of the potential box the allowed k-states are

$$k_x = \frac{n_x 2\pi}{L} \quad , \quad k_y = \frac{n_y 2\pi}{L} \quad \text{and} \quad k_z = \frac{n_z 2\pi}{L}, \qquad n_x, n_y, n_z \in \mathbb{N}. \tag{4.1}$$

The allowed states in reciprocal space are those whose coordinates along the three axes are given by multiples of $2\pi/L$. The Pauli principle now allows only two electrons per state to be occupied, one for each spin projection. The ground state can be constructed by successively filling two electrons in the unoccupied states with the lowest energy. The highest occupied state thus has a wave vector denoted with k_F and a corresponding energy E_F, the Fermi energy. For a sufficient number of electrons, the highest occupied states form a sphere in reciprocal space, the so-called Fermi sphere on which the electrons have the energy E_F. The total number of states in this sphere is given by the volume of the sphere divided by the volume one state ($(2\pi/L)^3$) multiplied by two, the number of electrons allowed in one state:

$$N = 2\,\frac{4/3\pi k_F^3}{(2\pi/L)^3}. \tag{4.2}$$

The resulting density of states is

$$D(E) = \frac{\mathrm{d}N}{\mathrm{d}E} = \frac{V}{2\pi^2}\left(\frac{2m}{\hbar^2}\right)^{3/2}\sqrt{E}\ . \tag{4.3}$$

In order to account for finite temperatures, the step-function which was assumed for the occupation of states for the construction of the Fermi sphere has to be replaced by the Fermi-Dirac distribution

$$f(E) = \frac{1}{e^{\frac{E-\mu}{k_B T}} + 1}, \tag{4.4}$$

where μ is the chemical potential. At $T = 0$ and in good approximation also at temperatures up to room temperature the chemical potential is equal to the Fermi energy [104] and the expressions "Fermi level" and "chemical potential" will be used synonymously in this thesis.

The central point in this theory is the introduction of the Fermi-Dirac distribution. Fig. 4.1 shows the sharp division between occupied and unoccupied states in three-dimensional metals which is slightly smeared out at finite temperatures and plays an important role in this thesis. Still it has to be kept in mind, that the model of the Fermi gas, where the electrons interact with neither the lattice nor other electrons, is a major oversimplification. Although it describes some transport and thermal properties well, it cannot account for the actual band structure observed in solids since it includes only the free electron dispersion.

Because of the success of the free electron model it was further enhanced by including more realistic assumptions. The consideration of a weak periodic potential already influences the electron wave function. This is expressed in the form of Bloch's theorem which states

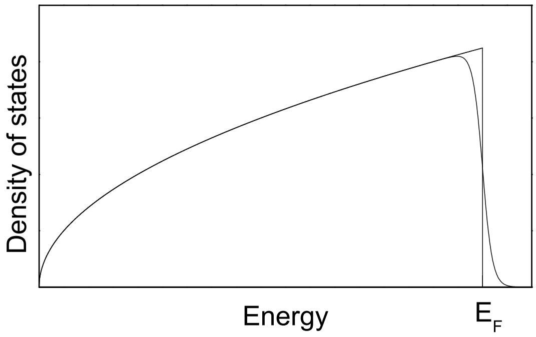

Figure 4.1: Density of states $D(E)$ for a free electron gas according to the Sommerfeld model. The occupation is given by the Fermi-Dirac distribution for $T = 0$ and finite temperature

that the one-electron wave functions are plane waves times a function with the periodicity of the Bravais lattice. It also leads to a modification of the free electron band structure because wave functions at the Brillouin zone boundaries fulfill the Bragg condition and the superposition of incoming and outcoming waves leads to the formation of a gap in the band structure under certain circumstances. Furthermore, the introduction of an effective mass $m^\star$ can account for deviations from the free electron dispersion, i.e. the real band structure. Nevertheless, this way of treating electrons in solids is restricted to a limited number of systems. The explicit inclusion of electron-electron interaction leads to a severe complication of the way the problem can be treated and is presented next.

Interacting electrons in 3D: Fermi liquid

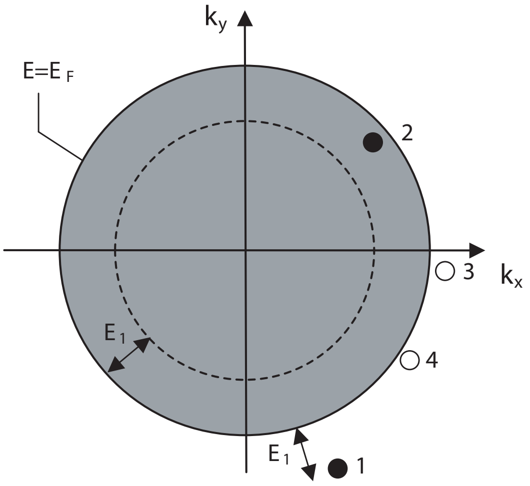

Figure 4.2: Illustration of the reduced scattering probability of Fermions (see text).

The microscopic theory of interacting electrons in three spatial dimensions was developed by Landau [105,106]. It is based on the picture of quasi-particles evolving out of the particles of a Fermi gas upon adiabatically switching on the interaction. These quasi-particles carry the same quantum numbers – spin, charge and momentum – as the original particles, but their dynamic properties are renormalized by the interactions (e.g. by the introduction of the effective mass $m^\star$) and their lifetime is finite. A quasi-particle can be imagined as a particle which disturbs other particles in its vicinity and whose motion itself is disturbed by surrounding particles. This picture holds true because the quasi-particle excitations are low compared to the Fermi energy E_F since in this energy range, the phase space for scattering events is severely restricted by the Pauli-exclusion principle. Fig. 4.2 illustrates this situation: Electron 1 with an energy E_1 above E_F can only scatter with a small number of electrons in the sphere, those with energy $E_2 \leq -E_1$, because the electrons have to be scattered out of the sphere, the only place where free states are available. This is approximately a fraction E_1/E_F of all electrons. In addition, also the final states (3 and 4) are restricted to those within E_1 above the Fermi level, adding another factor $\approx E_1/E_F$ leading to a scattering probability $\sim E_1^2$. At finite temperatures, E_1 is in the range of thermal excitations $E_1 \approx k_BT$ so that the scattering rate is $\sim T^2$.

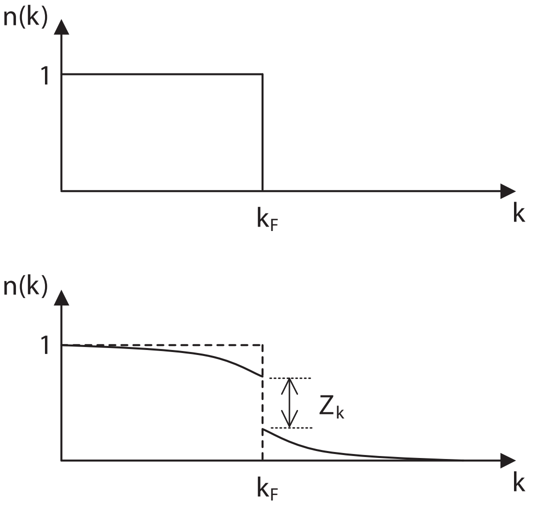

Figure 4.3: Schematic representation of the occupation of a non-interacting Fermion system (upper panel) and a Fermi liquid (lower panel) at $T = 0$. The discontinuity Z_k is a measure of the single particle character of the system.

The interacting Fermion system can be formally described by the one-particle Green's function. Here, the interaction is expressed in the so-called self energy which contains all the many-body effects and results in a shift and broadening of the quasi-particle states compared to those of the noninteracting particles. In this formalism one also obtains the quasi-particle renormalization factor Z_k which is a measure for the discontinuity at the Fermi level as depicted in Fig. 4.3. In the non-interacting case the discontinuity equals 1 and in the interacting case the discontinuity has the value $Z_k \leq 1$. Even at $T = 0$ states above E_F are occupied because particles in the system can be scattered out of their Bloch state by a collision with another electron, leaving the system in an excited state, leading to a finite occupation probability above E_F. However, as long as a finite discontinuity is observed, the system can be described in terms of the Landau quasiparticles [98].

4.2 Tomonaga-Luttinger liquid

Since the Fermi liquid picture breaks down for metals in one dimension, a new model is required. It is provided by the Tomonaga-Luttinger liquid model, describes interacting electrons in one dimension. The Tomonaga-Luttinger model is theoretical concept based on the works by Tomonaga [107] and Luttinger [108] which were later merged into a model which describes interacting fermions in one spatial dimension [109, 110], the so-called Tomonaga-Luttinger liquid (TLL), often simply referred to as Luttinger liquid.

The following section will explain the breakdown of Fermi liquid theory in 1D qualitatively. Then one aspect of the TLL model, the bosonization, will be explained. However, a complete comprehension of the theoretical background would exceed the scope of this thesis by far. Instead, the concept will be introduced in terms of phenomenological considerations. For introductions to the theory of Luttinger liquids, there are various works of varying lengths and approaches, eg. references [103, 111–115]. Another section is devoted to the TLL behavior of carbon nanotubes.

Breakdown of the Fermi liquid in one dimension

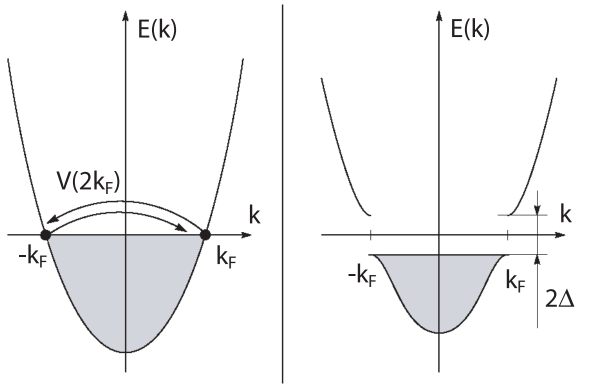

Figure 4.4: In a one-dimensional system of interacting fermions, scattering with a wave vector $2k_F$ leads causes the formation of a gap. Figure adapted from [111].

The Fermi liquid theory as discussed in the previous section does not hold in one dimension. This can be explained in a “rather qualitative and handwaving” way (Voit in [111]) on a microscopic level with the Peierls instability [116]. In general, the Peierls instability describes a metal-semiconductor transition due to coupling with phonons of wave vector $2k_F$. Since in 1D the whole Fermi surface is matched by this transition (in 3D only two points on the Fermi sphere with a measure zero are projected onto each other upon such scattering) a great number of electron-hole excitations take place and lead to an instability of the Fermi surface resulting in the formation of a gap at k_F. This umklapp-scattering with a wave vector $2k_F$ is not limited to phonons, it also appears upon electron-electron interaction. Fig. 4.4 shows this scenario and illustrates that the 1D Fermi gas is unstable towards any finite interaction, it destroys the Fermi surface. The stable excitations in a TLL are collective electron-hole pair modes (plasmons).

In a more accurate approach it can be shown that the self-energy of interacting electrons in one-dimension leads to two poles (i.e. energies of the quasi-particle excitations) in the Green’s function[1] thereby violating the single-pole assumption of the Fermi liquid [111].

Bosonization and phenomenological results

The theoretical development of TLL theory is based on the bosonization of the fermion system, a concept first developed by Bloch [117], who realized the striking similarity of the low-energy excitations of non-interacting fermions (Pauli’s Fermi gas approximation) and a linear harmonic chain, where the excitations are bosonic. This similarity is best illustrated by the specific heat. In contrast to the three-dimensional case, where the lattice contribution yields Debye’s T^3 law. The heat capacity of a linear harmonic chain results in

$$c_{\mathrm{1D}}^{\mathrm{lattice}} = \frac{\pi}{3} k_B \frac{k_B T}{\hbar c_s}, \tag{4.5}$$

---

[1] This is related to the charge-spin separation in 1D metals.

where c_s is the sound velocity. The heat capacity of a one-dimensional non-interacting Fermi gas is

$$c_{\mathrm{1D}}^{\mathrm{electrons}} = \frac{\pi}{3} k_B \frac{k_B T}{\hbar v_F}, \tag{4.6}$$

where v_F is the Fermi velocity. These results are identical apart from the respective velocities, although the standard ways to calculate them are very different, because of the difference in Boson and Fermion occupation rules.

In the case of the linear harmonic chain, fixed boundary conditions are applied so that only discrete k-states (multiples of $\hbar c_s(2\pi/L)$ are allowed. If one then assumes that the energy dispersion is linear for small wave numbers ($\omega_k \approx c_s|k|$), equidistant energy states are obtained. The energy of an excited state $E(n_k) - E_0 = \sum_k \hbar\omega_k n_k$ is then classified by the occupation numbers n_k which can take values from zero to infinity.

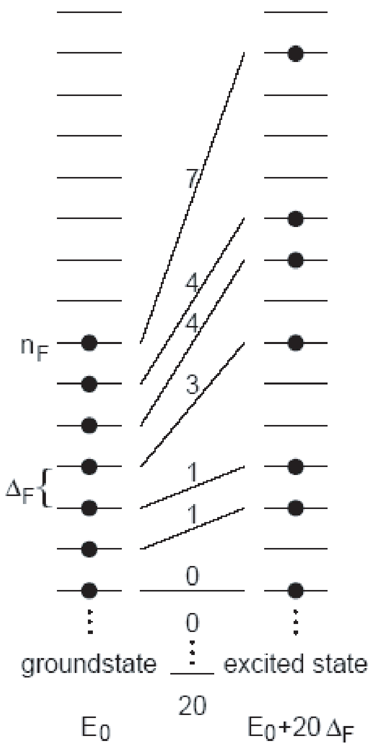

Figure 4.5: Illustration of how the excited states can be classified in terms of upward shifts by Δ_F. In this example the non-zero occupation numbers are $n_7 = 1, n_4 = 2, n_3 = 1$, and $n_1 = 2$. Figure adapted from [112].

The same approach is now used in the bosonization of the 1D fermionic system which is carried out in two steps.

1. The kinetic energy dispersion around the Fermi point $\mathrm{k_F}$ is linearized. Using fixed boundary conditions which result in $\mathrm{k}_m = m\pi/L$, the additional energy of excited states compared to the ground state is a multiple of $\Delta_F = \hbar v_F \pi/L$.

2. The states of the system are classified with respect to the ground state by upshifts of j units of Δ_F. The highest excited state is related to the highest occupied ground state and so forth for the second, third etc. The system is then characterized by the distribution of $\{n_j\}$ upshifts which can take not only values of zero and one like fermions but from zero to infinity like bosons (Fig. 4.5).

Even in a non-interacting Fermion system this procedure allows to rewrite the expression for the total kinetic energy with annihilation and creation operators which obey boson commutation relations: The creation and annihilation of a fermion with $k_n = n\pi/L$ is expressed by c_n^+ and c_n respectively. With a linear energy dispersion relation $\varepsilon_n = \hbar v_F k_n$, the energy of the excited state can consequently be written as

$$T = \sum_{n=1}^{\infty} \hbar v_F k_n c_n^+ c_n. \tag{4.7}$$

Using the so-called "Kronig identity" [114], this can be rewritten as

$$T = \sum_{n=1}^{\infty} \hbar v_F k_n c_n^+ c_n = \frac{\hbar v_F \pi}{L}[\sum_{l=1}^{\infty} l b_l^+ b_l + \frac{1}{2}\mathcal{N}(\mathcal{N}+1)], \tag{4.8}$$

where the b_l are defined as

$$b_l = \frac{1}{\sqrt{l}} \sum_{m=1}^{\infty} c_m^+ c_{m+l} \tag{4.9}$$

and $\mathcal{N} = \sum_{n=1}^{\infty} c_n^+ c_n$ is the fermion particle number operator. It can be shown that the b_l obey boson commutation relations. In a first step it was thus shown, that a non-interacting Fermi gas in one dimension can be expressed in terms of boson annihilation and creation operators and a bosonic distribution of the excited state.

Tomonaga's and Luttinger's achievement was now to transfer this concept of the bosonization of a 1D Fermi gas to interacting fermions. Instead of quasi-particles, the elementary excitations are collective charge and spin modes, leading to charge-spin separation. The physical properties depend on a limited number of parameters, the most important being the coupling constant or Luttinger parameter g. Correlation functions exhibit power law behavior [103]. E.g. the following equation results for the momentum distribution function:

$$n(k) \sim |k - k_F|^{\alpha} , \tag{4.10}$$

leading to a power law renormalization of the single-particle density of states

$$N(\omega) \sim | \omega |^{\alpha} . \tag{4.11}$$

Here, the breakdown of the Fermi liquid becomes manifest again: the discontinuity $Z(k)$ no longer appears at the chemical potential. The power law exponent α is linked to the coupling constant g as

$$\alpha = \frac{g + g^{-1} - 2}{8} . \tag{4.12}$$

It should thus be accessible in experiments which probe the density of states, i.e. in PES. But power laws of the differential conductivity as a function of temperature and bias voltage are also predicted for transport experiments through a quantum wire [118], although in these cases the power law depends differently on the coupling constant.

An interesting point concerns the validity of TLL theory for dimensions larger than one. Castellani et al. found that Fermi liquid behavior is relatively quickly restored upon a continuous transformation from a one-dimensional to a two-dimensional system [119]. Arrigoni obtained a similar result treating a perpendicular hopping between parallel TLL chains [120]. With increasing hopping, the Fermi liquid quasi-particle weight $Z(k)$, in other words the discontinuity at E_F, and as such Fermi liquid behavior, is successively restored.

In conclusion, one-dimensional metals exhibit clearly different properties compared to the three-dimensional case. Most importantly power laws in experimentally accessible quantities arise. Next, the consequences of these results on carbon nanotubes – in their metallic version a paradigm for a one-dimensional metal – will be discussed.

4.3 Experiments on one-dimensional systems

A first claim of the possible observation of a TLL power law renormalization was made from angle-integrated PES of the so-called Bechgaard salt [121], an organic charge transfer complex [122] but serious doubts remained [123]. The same is true for quasi-one-dimensional quantum wires on silicon substrates, where the interpretation of a two peak structure in ARPES spectra as spin-charge separation [124] was questioned [125]. Spin-charge separation was equally found in the quasi-one-dimensional organic conductor TTF-TCNQ but could not be interpreted in terms of a TLL behavior [126]. The main disadvantage of these compounds is that they are not truly isolated one-dimensional systems.

This is not the case for SWCNTs. The one-dimensional structure of SWCNTs and the fact that – depending on the chirality – one third of all tubes is metallic have sparked the interest in SWCNTs as a system of interacting electrons in one dimension. Although one-dimensional systems are generally unstable under a Peierls distortion (see above), the energy gap obtained for metallic nanotubes is found to be greatly suppressed with increasing nanotube diameter and quickly approaches the zero-energy gap of two-dimensional graphite [7,27,127]. Theoretical works predicted TLL behavior in SWCNTs and estimated an interaction parameter $g \approx 0.2$ [128,129].

Furthermore, the power law exponents also depend on the number of conduction channels [130]. The more one-dimensional channels contribute to the conduction, the lower the value of α, making the situation somewhat more complicated for C_{60} peapods where it is unclear wether bands from the C_{60} filling (e.g. the lowest unoccupied molecular orbital, the t_{1u} band) cross the Fermi level.

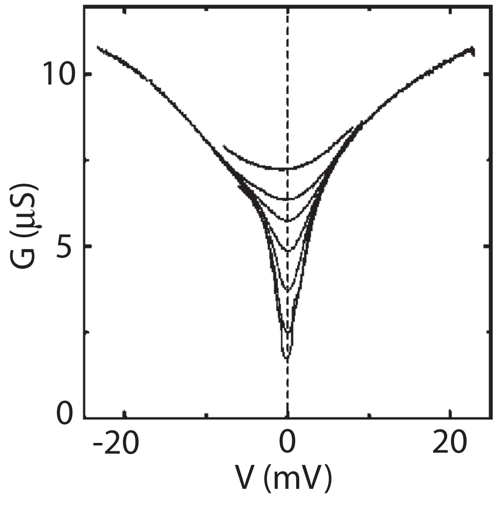

Figure 4.6: The zero-bias anomaly in MWCNTs: The tunneling conductivity G is suppressed at low bias voltages. In addition, the zero-bias anomaly increases with decreasing temperature, i.e. G is temperature-dependent at zero bias. Picture taken from [24].

The achievement of contacting individual tubes enabled the first experiments on TLL behavior of SWCNTs. Transport experiments on metallic nanotubes exhibit a zero-bias anomaly, i.e. a suppression of the electrical conductance at low bias voltages where a constant conductivity would be expected in a conventional (three-dimensional) metal . The zero-bias anomaly is an indication for electron-electron interaction in the tubes and was observed in both SWCNTs and MWCNTs. Fig. 4.6 illustrates its behavior for the case of MWCNTs. Measurements on bundles of SWCNTs revealed a power law scaling of the zero-bias anomaly, or more precisely of the differential conductance $dI/dV \sim V_G^\alpha$ as well as of the temperature-dependent conductance $G(T) \sim T^\alpha$. The actual value of α depends on the contact geometry but similar power law coefficients for the gate voltage- and temperature-dependent measurements were obtained [23] yielding an interaction parameter $g \approx 0.28$. Transport through individual [26] and crossed individual SWCNTs [25] was equally well explained within a framework of tunneling into and between TLL [131].

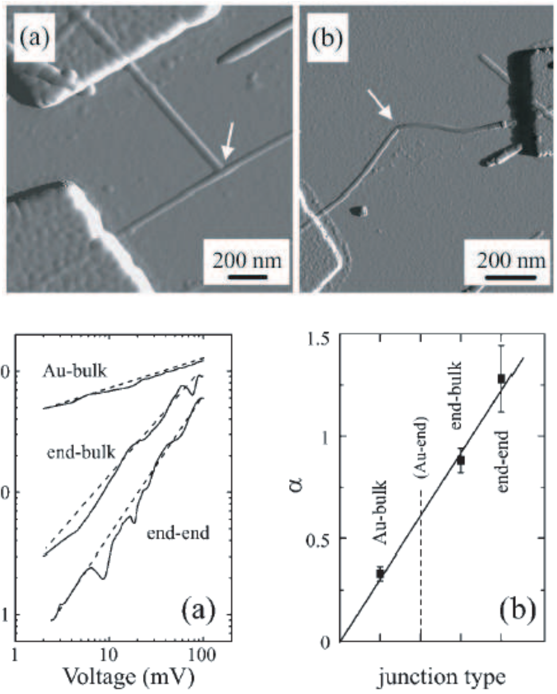

Figure 4.7: Upper panel: AFM images of junctions formed between MWCNTs: a) end-bulk junction and b) end-end junction. The arrows indicate the position of the junction. **Lower panel:** a) Tunneling conductance G as a function of the bias V for the given contact geometries. b) Plot of the power law scaling factor α as a function of the junction type. Figure from [24].

In the same way, tunneling into and between multi-wall carbon nanotubes (MWCNTs) obeys power laws. Fig. 4.7 shows the different contact geometries and the resulting power law scaling from Ref. [24]. Again, the actual power law scaling is hugely dependent on the contact configuration. On the one hand, these results can be explained within a TLL model [130], on the other hand the power law scaling can equally be understood in terms of tunneling into a particularly effective and non-conventional Coulomb blockade [132].

However, these transport experiments suffer from some uncertainties. First, the role of the contacts is not completely resolved and second, the probed energy scale ($\approx$ 50 meV, i.e. much smaller than the expected range for charge carrier interaction as estimated from the exciton binding energy) is relatively small. Especially in regard of the energy scale, photoemission spectroscopy should be much better suited for such investigations. Since photoemission spectroscopy directly probes the electronic density of states it should be an ideal tool to probe the properties of a TLL, especially the power law renormalization at the Fermi level. In this regard, the investigation of SWCNTs using PES promises new insight in this field. In the following chapters, the promising combination of a nearly perfect one-dimensional system – SWCNTs – and the ideal tool to study the renormalizations of one-dimensional systems – PES – will be used to gain new knowledge on the metallic ground state of pristine and functionalized SWCNTs.

4.4 Summary

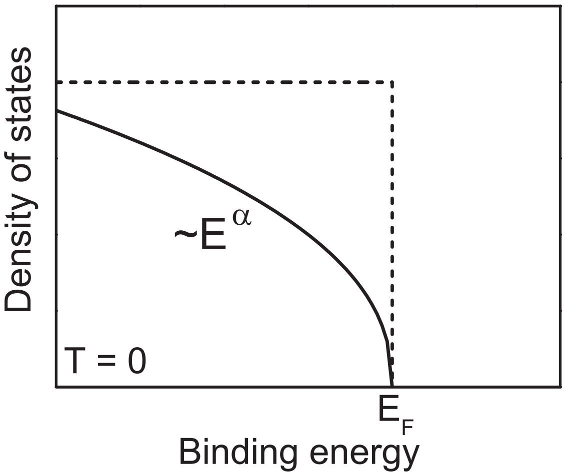

Figure 4.8: Illustration of the different scaling behavior of the density of states in one and three dimensions at T = 0. Dashed line: Fermi edge (3D Fermi gas picture). Solid line: Power law (1D Tomonaga-Luttinger liquid)

This chapter demonstrated that distinct differences exist between the behavior of interacting electrons in one and three spatial dimensions. Three-dimensional metals can be well described by the Fermi liquid theory of interacting electrons and its quasi-particle picture. These quasi-particles evolve out of the original non-interacting particles with renormalized properties. The quasi-particle picture breaks down in one dimension due to the Peierls instability. Instead, interacting electrons in 1D metals are described by Tomonaga-Luttinger liquid theory which results in peculiar properties such as spin-charge separation and non-universal power laws, where the actual scaling depends on the interaction strength. One of those power laws is the renormalization of the electronic density of states. Fig. 4.8 illustrates this scaling in comparison to the sharp Fermi edge of the Fermi gas model. This fundamental difference should be observable in experiments probing the density of states. Thus, photoemission spectroscopy is used in the following chapters in order to probe the nature of the metallic ground state of pristine and functionalized SWCNTs.

5 Electronic properties of pristine SWCNT

This chapter presents the properties of the SWCNT valence and conduction band as well as the core level states as obtained from photoemission and x-ray absorption spectroscopy. On the one hand, these results nicely link the two introductory parts on carbon nanotubes and the experimental techniques, on the other hand they form a starting point for the subsequent doping experiments. After verifying the sample purity, the various features in the XPS and UPS response are studied. The C1s and the carbon Auger line shapes are analyzed. The valence band response is discussed with special regard to the peculiarities of SWCNTs as compared to graphite. These are the so-called van Hove singularities and the renormalization of the electronic density of states due to Tomonaga-Luttinger liquid behavior.

5.1 Core level and XPS

X-ray photoemission spectroscopy (XPS) is a useful tool for studying the core level states of materials in a wide range of binding energies. It allows the sample composition and thus the purity of the SWCNTs to be determined. Additional information can be obtained from the core level line shape – in this case the line shape of the C1s response – and from the Auger electrons.

XPS survey: Sample composition

Information on the purity of the sample is crucial for the photoemission investigation of SWCNTs. Especially the investigation of the metallic ground state could be decisively influenced by metallic catalyst particles remaining in the sample. Furthermore, the SWCNT buckypaper is prone to the adsorption of water and carbon oxides. In order to remove the contaminations, the sample was *in situ* annealed at 450 °C for several hours. The efficiency of this procedure can easily be checked by XPS. Fig. 5.1 shows the core level photoemission spectrum of SWCNTs before and after annealing. The most prominent feature is the C1s peak at 285 eV binding energy. It will be analyzed in more detail below. Another feature related to carbon is the carbon Auger peak, which is found in the spectrum at 1217 eV, corresponding to a kinetic energy of 267 eV which also will be discussed in more detail below. In both cases – before and after annealing – no signal is detected from the NiCo catalysts used for the production of the sample. It would have been expected at binding energies of 870 and 853 eV as well as 793 and 778 eV for the $2p_{1/2}$ and $2p_{3/2}$ of nickel and cobalt

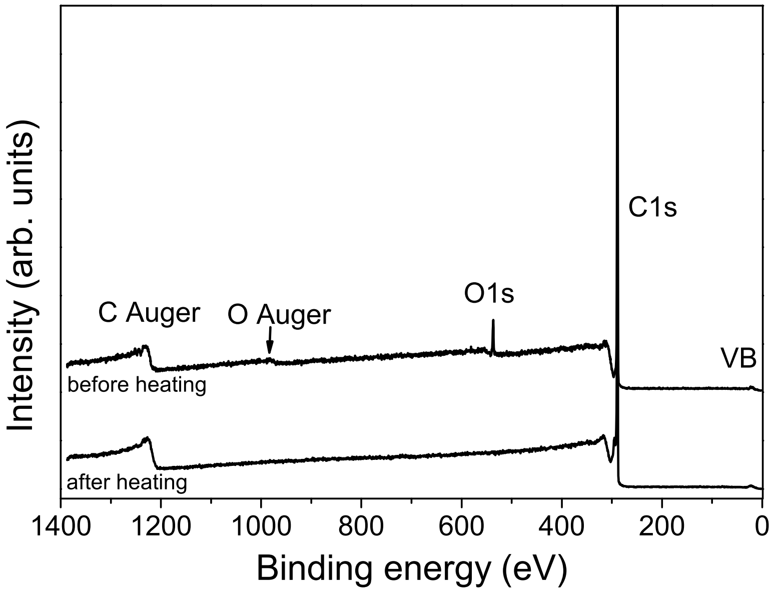

Figure 5.1: XPS survey of SWCNTs before (upper curve) and after (lower curve) heat treatment. The C1s peaks are cut off for better visibility of the other features.

respectively. The purification process is obviously very effective in removing the catalyst particles.

Before annealing, a peak at 537 eV binding energy can be identified in the spectrum of SWCNTs . It stems from the oxygen 1s core level electrons. Since no signal is detected from the metal catalysts, this peak is not related to oxidized catalyst particles. Instead it most probably originates from water or carbon oxides chemisorbed or physisorbed on the nanotube wall. The lower curve in Fig. 5.1 shows that after annealing the O1s peak is no longer visible. The contaminations are thus efficiently removed by the annealing process. A contamination-free sample is important for the valence band investigations, since oxygen also has contributions in this region. The valence band itself can also be seen in the spectrum at low binding energies as indicated in the figure. But investigation of this with XPS is very impractical due to low intensity and an energy resolution of only 0.4 eV. It is preferably done by UPS as reported below. All in all, the survey spectrum reveals a very high sample quality and purity, making it suitable for the following investigations.

C1s core level

The C1s response which is depicted in Fig. 5.2, again excited by Al-Kα x-rays, is now further investigated. The peak position can now be determined more accurately and is found at 284.7 eV with a full width at half maximum (FWHM) of 0.7 eV. These values are in good agreement with values obtained from previous measurements with x-ray radiation [133,134]. The width is considerably greater than that of graphite [135,136]. In addition, the line shape features an asymmetry which can also be observed in graphite while it cannot be observed in C_{60}. This asymmetry is attributed to the metallic tubes in the sample.

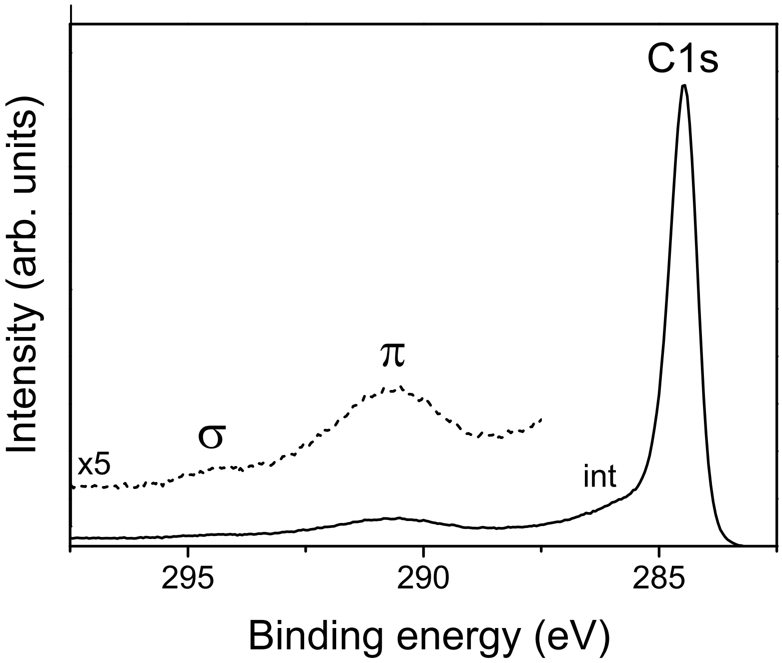

Figure 5.2: XPS spectrum of the C1s core level response of SWCNTs ($\hbar\omega$ = 1468.8 eV, solid line). The dashed line represents the satellite region of the same spectrum magnified by a factor of five.

On the higher binding energy side of the C1s peak, the response exhibits a kink above which the intensity decreases somewhat more slowly. In addition, in the magnification of the higher binding energy region (dashed line in Fig. 5.2), two small humps can be identified at 290.5 and 294.7 eV binding energy. These are the so-called satellites [137]. They do not correspond to actual electronic states of carbon near the C1s level but stem from inelastic scattering of some of the electrons upon leaving the sample. The three features originate from intraband transitions and the excitation of π and σ plasmons as indicated in Fig. 5.2. The excitation of these plasmons and interband transitions causes a loss of kinetic energy of some electrons, making them appear to have a higher binding energy than actually is the case.

Auger line shape

The basic principle of the Auger process was introduced in section 3.2.1: Irradiation with light creates a core hole which is subsequently filled by an electron from an higher-lying state, which transfers the energy gained to another electron, which in turn can leave the sample. In this specific Auger process, the core hole in the C1s state created by x-ray irradiation is filled by an electron from the valence band with the simultaneous emission of another electron from the valence band. The kinetic energy of this emitted electron is now exactly the difference between the C1s and valence band energy of the decaying electron less the binding energy of the emitted electron and the work function (see Fig. 3.3):

$$E_{\text{kin}}^{\text{Auger}} = E_B^{\text{core}} - E_B^{\text{V1}} - E_B^{\text{V2}} - \Phi \tag{5.1}$$

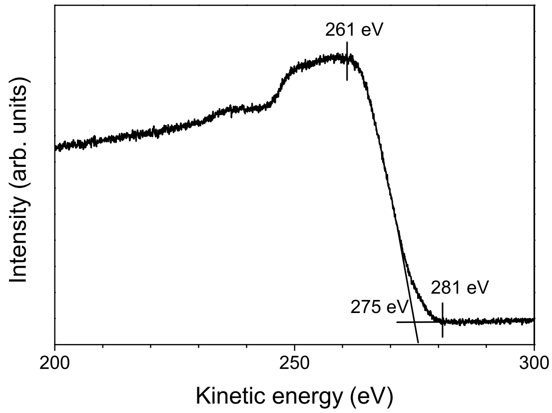

Figure 5.3: Carbon KVV Auger spectrum of SWCNTs as a function of the kinetic energy. The lines denote the features discussed in the text. The respective kinetic energies are specified.

Since C1s (also called K shell) and valence band (V) states contribute to this process, it is called KVV Auger decay. The Auger spectrum is composed of all possible combinations of valence band electrons. The electrons may either both come from the same band, i.e. the π- or the σ-band or one from the π-band and one from the σ-band. The Auger spectrum is thus a self-convolution of the valence band spectrum [138] and can be used to estimate valence band properties.

The Auger response is depicted in more detail in Fig. 5.3 in terms of kinetic energy. It can be used to estimate some valence band properties. In the following the three main features which are indicated in the figure will be discussed.

The Auger electrons with the highest kinetic energy come from processes where both participating electrons come from states with the lowest binding energy. This high binding energy onset is found at 281 eV kinetic energy [1]. It was shown above that the C1s binding energy is $\approx$ 285 eV and that the work function is $\Phi \approx 4$ eV (see section 3.2.2). This means that Eq. (5.1) can only be satisfied if $E_B^{V1} = E_B^{V2} = 0$, i.e. if both participating electrons come from the Fermi level. This indicates that in the SWCNT bundles are indeed metallic tubes.

However, the density of states which participate in the process is low at low binding energies. The Auger process should increase strongly if the electrons come from states with a high density of states which is the case at the maximum of the π-band. The onset of the strong increase of the Auger response towards lower kinetic energies is indicated in Fig.5.3 and a value of 275 eV is obtained. Using eq. 5.1 and assuming both electrons have the same binding energy, the resulting binding energy is $\approx$ 3 eV, which is close to the peak position of the π-band later obtained from UPS. Under the same considerations the electron binding energies corresponding to the maximum of the Auger response at 261 eV result as $\approx$ 10 eV which is close to the binding energy of the σ-band.

The Auger line shape can thus be qualitatively described by the valence band structure of SWCNTs which is discussed below. For a more detailed analysis of the Auger electrons one has to resolve the valence band fine structure. In this case the comparison of the self-convoluted valence band spectrum with the Auger line shape can be used to obtain quantitative information on correlation effects as it was achieved with C_{60}, where the actual amount of the hole-hole interaction was determined [79, 139, 140].

---

[1] All energies used in this part will be rounded to 1 eV because of the estimative character of the reasoning.

5.2 Valence band

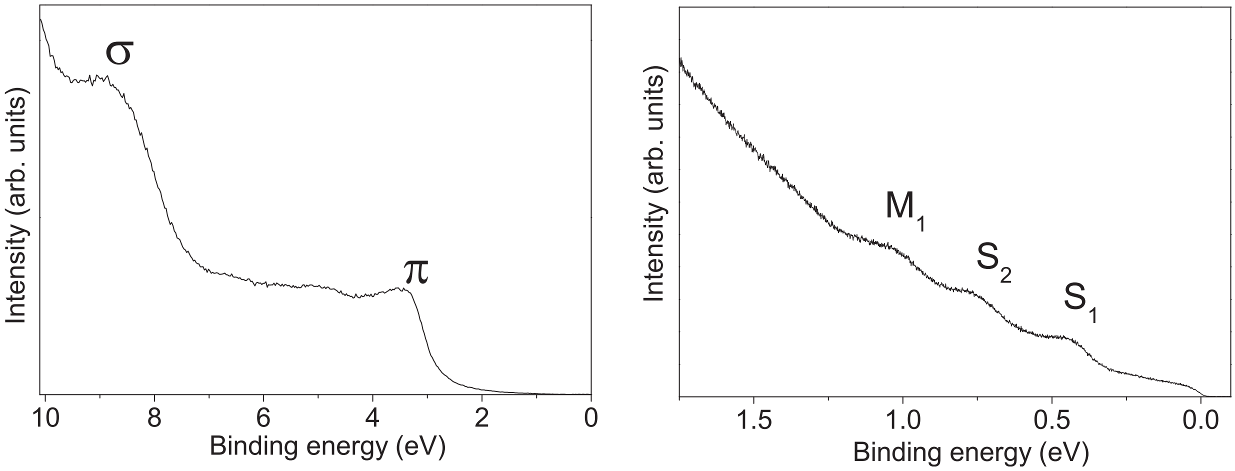

Figure 5.4: Valence band photoemission of SWCNTs. **Left panel:** Region of the π and σ bands which are labelled accordingly. **Right panel:** Photoemission response close to the Fermi level. Three peaks at binding energies of 0.44, 0.76 and 1.06 eV binding energy appear. They are assigned to the van Hove singularities from the semiconducting (S_1, S_2) and the metallic (M_1) tubes.

The right panel of Fig. 5.4 depicts the valence band region of SWCNTs, excited with He Iα radiation (21.21 eV), in the binding energy range up to 10 eV. As expected, the π and σ bands can be identified. The π band is found at 3.1 eV binding energy while the σ band is located at 8.5 eV, in agreement with previous results [141, 142]. In this energy range, the SWCNT spectrum is qualitatively the same as that of graphite. But in the region near the chemical potential, deviations of the SWCNT response from the graphite spectrum are expected due to the one-dimensional character of the SWCNTs. And indeed, features typical only for SWCNTs appear in the spectrum. In the region depicted in the right panel of Fig. 5.4 for binding energies up to 2 eV, three peaks can be observed. They can be ascribed to the spikes in the density of states of SWCNTs, the van-Hove singularities. The two peaks at lower binding energies, situated at 0.44 and 0.76 eV originate from the first two van-Hove singularities of the semiconducting tubes and are labelled S_1 and S_2 respectively. The peak from the first vHs of the metallic tubes (M_1) is found at 1.06 eV. Again, this is in good agreement with previous results [55].

A quantitative analysis of the SWCNT sample, i.e. determination of mean diameter and diameter distribution based on the peak positions and their widths, is not as straightforward as in optical absorption spectroscopy, though. The gap energy which is a measure for the tube diameter cannot simply be estimated from the distance of the vHs peaks to the chemical potential because the valence band vHs S_1 and the conduction band vHs $S_1^\star$ would only be symmetric around the Fermi level of the SWCNT bundle in the simplest picture. In a film of SWCNT bundles on a substrate, the position of the Fermi level is influenced by several factors. First of all, it is well known from scanning tunneling spectroscopy of individual nanotubes that the vHs peaks of semiconducting SWCNTs can be shifted with respect to middle of the band structure due to charge carrier injection from the substrate [57]. In STS this shift amounts to up to 0.1 eV. A similar effect can be expected for the photoemission experiments. Second, within a bundle consisting of a mixture of semiconducting and metallic SWCNTs the actual Fermi level is adjusted by contact potentials. The presence of these

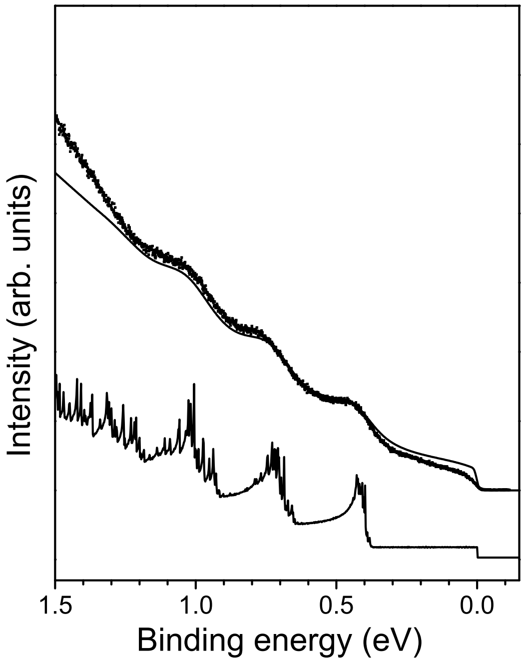

Figure 5.5: Upper curves: Comparison between the experimental (dotted line) and calculated (solid line) photoemission spectra of SWCNTs. The calculated curve was obtained as described in the text and yields a mean diameter of the SWCNT sample of 1.37 nm with a standard deviation of the distribution of $\Gamma_d = 0.06$ nm. Lower curve: Bare calculated density of states (without lifetime and resolution broadening) as obtained from the addition of the single-tube density of states.

effects in the measurements at hand can already be shown in a simple estimation. If one assumes that the Fermi level is symmetrical in the SWCNT band structure, the binding energy of the vHs in the valence band is expressed in the tight-binding model as

$$E_i \sim \frac{i\gamma_0}{d} \ , \tag{5.2}$$

where those vHs in which i is a multiple of three belong to metallic tubes, the others to the semiconducting tubes. In that picture, the binding energy position of the peaks originating from the vHs in the photoemission response should be at multiples of the S_1 binding energy.

The energy distance between both S_1 and S_2 and that between S_2 and M_1 is about the same, namely about 0.3 eV as is to be expected from the TB model. If the Fermi level were situated in the middle of the band structure, its binding energy would be roughly the same as those energy distances, i.e. ~ 0.3 eV. But this is not the case. The binding energy of the S_1 peak is 0.44 eV, indicating a shift of the Fermi level from the middle of the band structure, most probably due to charge carrier injection from the substrate. Using these considerations, the position above the Fermi level of the first unoccupied vHs of the semiconducting tubes, $S_1^\star$, can be estimated. Taking into account the aforementioned Fermi level shift and that in the simple model, the distance between $S_1^\star$ and S_1 is twice the distance between S_1 and S_2, the $S_1^\star$ is expected to lie at least 0.2 eV above the Fermi level. This result will play an important role in the interpretation of the doping experiments.

Taking into account this effect, one should be able to obtain quantitative information about the sample from the peak positions and shapes obtained from the photoemission response in a similar way as it was carried out by optical absorption spectroscopy (see section 3.4). First, the band structure of individual SWCNTs of all possible chiralities is calculated using the tight-binding model and a $\gamma_0 = 2.9$ eV. It is then assumed that the diameter of the nanotubes in the sample is Gauss-distributed with a certain mean diameter

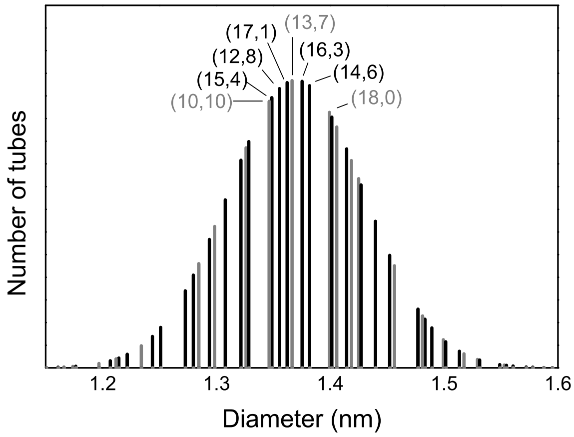

Figure 5.6: Diameter distribution for a nanotube sample with 1.37 nm mean diameter and a standard deviation of the distribution of $\Gamma_d = 0.06$ nm. Grey lines indicate metallic nanotubes, black lines are semiconducting nanotubes. The chiralities are indicated for the most frequent tubes.

and distribution width. The single-tube band structures are added up according to this distribution. Finally, the resulting density of states is smeared out with a Gaussian curve and a Lorentzian curve in order to take into account the spectral lifetime broadening and the finite resolution of the experiment. By adjusting the sample-related parameters for the mean diameter and the distribution width and by including an energy shift due to charge carrier injection as described above, the photoemission spectrum can be fitted. Fig. 5.5 depicts the results of the fit. The upper curves show the photoemission response and its fit. The lower curve represents the bare calculated density of states as obtained from the addition of the single-tube densities of states. Using the experimental resolution of 10 meV and a Fermi level shift of 0.11 eV, the sample characteristics resulting from this fit are a mean diameter of 1.37 nm with a standard deviation $\Gamma_d = 0.06$ nm. These values are in very good agreement with those obtained from OAS in section 3.4. Fig. 5.6 shows the resulting distribution of tube chiralities.

Nevertheless, there is one important discrepancy between calculated and experimental photoemission response: The behavior exactly at the Fermi edge is not well described by the fit. This is due to the fact that the TB model does not take into account the power law scaling of the electronic density of states due to the one-dimensional electronic structure and simply assumes a sharp Fermi edge. This topic is discussed in the following section.

5.3 Tomonaga-Luttinger liquid behavior

Section 4.3 discussed that metallic SWCNTs are a paradigm of one-dimensional metals and as such should exhibit Tomonaga-Luttinger liquid behavior instead of Fermi liquid behavior. TLL behavior is expressed in non-universal power laws. Most importantly, the electronic density of states is renormalized as $N(\omega) \sim \omega^\alpha$ as opposed to the discontinuity of a three-dimensional Fermi liquid at the chemical potential. Transport experiments showed such power law behaviors but uncertainties in the interpretation remained regarding the contacting and, in the case of MWCNTs, also the transport regime. The power law renormalization is directly accessible in photoemission experiments [55]. The value of the power law renormalization of the density of states, α can be obtained by two means: firstly via a fit of the density of states and secondly – in a much simpler way – via a linear fit of the photoemission response near E_F on a double-logarithmic scale. In the following chapters, the latter will be an often-used tool in the study of the TLL behavior on doping and thus this procedure will now be explained in more detail by first elucidating the TLL energy scale, i.e. the region in the photoemission spectra where the power law renormalization is expected.

TLL energy scale

In the previous chapter it was discussed that transport measurements only probe the TLL behavior on a small energy scale. This scale can be expanded using photoemission spectroscopy which covers the whole valence band binding energy range. However, there are no exact predictions of the energy scale on which the power law renormalization takes place. The energy scale of TLL behavior is determined by the strength of the electron-electron interaction which itself is in the same order of electron-hole interaction. Electron-hole interaction can be described in terms of excitons, and the existence of these quasi-particles was recently verified experimentally using two-photon photoluminescence experiments [21, 22]. The measured binding energy of the excitons depends on the tube diameter and range from up to 420 meV for 0.68 nm diameter tubes to 270 meV for 1.08 nanometer tubes. More precisely, the exciton binding energy of an isolated tube scales with the inverse tube diameter [53, 54] and obeys the following relation obtained in Ref. [53]:

$$E_B^{\text{Exciton}} \cong \frac{0.34\ \text{nm}\,\text{eV}}{d_t}\ , \tag{5.3}$$

where d_t is the tube diameter. For tubes with a mean diameter of those used in the experiments, the exciton binding energy can be estimated and it follows that $E_B^{\text{Exciton}} \approx 240\,\text{meV}$. Furthermore, this value is a lower estimate since the exciton binding energy also increases with the dielectric constant of the environment of the the tubes which is higher in bundles [54]. The value of the exciton binding energy can be used as a measure for the electron-electron interaction and thus the TLL power law renormalization is expected to be effective in this binding energy region. Using the experimental setup at hand, this region is well accessible with a high resolution. However, the confirmation of power law behavior of the electronic density of states can be hindered by other factors. Special attention has to be paid to the experimental limitations due to finite resolution and temperature. The energy resolution was set in these experiments to 10 meV. All experiments were carried out at a temperature of 35 K. The temperature broadening can be estimated as $\Delta E \approx 4k_BT$ [100], where k_B is the Boltzmann constant and T is the temperature. The resulting temperature broadening of the occupation distribution is then ≈ 12 meV and thus in the same range as the resolution limit. Accordingly, a potentially pure power law behavior is smeared out in this energy range above the Fermi level.

Another limitation stems from the shape of the actual band structure. Fortunately, metallic SWCNTs have a constant density of states up to the first van-Hove singularity[2] situated about 1 eV above the chemical potential for the SWCNTs used in our studies. On the other hand, the signal of the semiconducting tubes is superimposing that of the metallic tubes, starting with the first vHs situated at 0.44 eV binding energy. The resulting peak is relatively broad due to the diameter distribution. Since the width of this distribution is

---

[2] The density of states is constant in a tight-binding approximation which does not include eventual scaling of the DOS due to TLL behavior

known, energy level above which it has a significant contribution to the PES response can be calculated. As seen above, the diameter distribution is a Gaussian and thus peak shape also reflects this distribution. The peak is centered at 0.44 eV. From Eq. (5.2) the energy width can be calculated from the distribution width of the diameter as

$$\Delta E = \frac{\Delta d}{d} \cdot E = 0.019\,\text{eV} \ . \tag{5.4}$$

The Gaussian distribution is defined as

$$y = \frac{1}{\sqrt{2\pi\sigma^2}} e^{-\frac{(x-x_c)^2}{2\sigma^2}} \ , \tag{5.5}$$

where x_c is the center of the distribution. Therefore the distance from peak center at a given y-value is

$$x - x_c = \sqrt{-\sigma^2 ln(2\pi y^2 \sigma^2)} \tag{5.6}$$

The distance from the peak center to the point where the Gaussian distribution is only 5% of its maximum value can now easily be calculated using $y = 0.05$ and $\sigma = 0.019$ eV. It follows that $x - x_c = 0.14$ eV. The intensity of the Gauss distribution is thus reduced to 5 % of its maximum value at a distance of 0.14 eV from the peak center. It is more than reasonable to assume that here the contribution from the peak to the photoemission response is negligible. We can thus safely say that at about 0.07 eV below the peak center, i.e. at ca. 0.30 eV binding energy in the pristine case, its contribution to the photoemission response can be neglected. This means that there is a region, where an observation of the power law scaling of the density of states is not disturbed by measurement limits or a superimposing signal from the semiconducting tubes. This region is situated between the resolution and temperature broadening limit at 0.012 eV and the beginning contribution from the semiconducting tubes at roughly 0.30 eV. Towards higher binding energies, the determination of the power law behavior is thus only limited by the energy scale of TLL renormalization. At the Fermi level, temperature and resolution broadening has to be accounted for.

Determination of the power law scaling factor

The above considerations enable us to investigate the photoemission response of SWCNTs in the region close to the Fermi level in more detail. The resulting spectrum, taken at a temperature of 35 K, is depicted in the left panel of Fig. 5.7. Although there appears to be a finite intensity up to the Fermi level, the response appears somewhat suppressed and the line shape does not resemble a typical Fermi edge. This suppression of spectral weight can be ascribed to a power law scaling of the density of states due to TLL behavior as it was done in Ref. [55]. In order to verify this behavior and to obtain the power law scaling factor α, the spectrum is simulated. For this, a power law density of states E^{α}, which is occupied according to the Fermi distribution at finite temperature, is assumed. The limited resolution of the measurement is taken into account by convolution with a Gaussian distribution. The photoemission response results then as:

$$I(E) = A \int \varepsilon^{\alpha} \ \frac{1}{e^{-\varepsilon/k_B T} + 1} \ e^{\frac{(\varepsilon - E)^2}{2\sigma^2}} d\varepsilon, \tag{5.7}$$

where σ is the standard deviation of the Gaussian distribution and A an arbitrary scaling factor. The solid line in the figure represents the fit in which the width of the Gauss curve

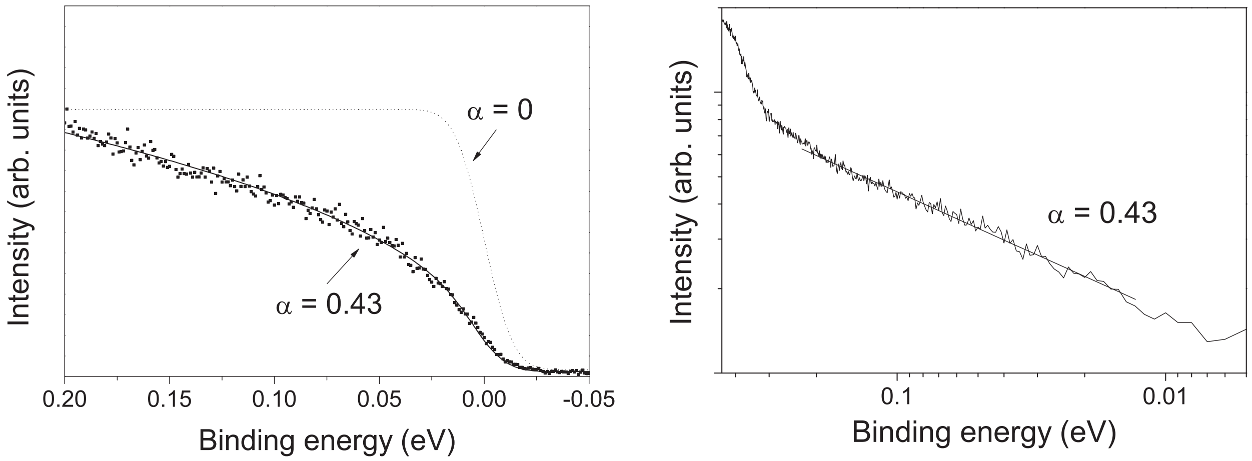

Figure 5.7: Valence band of SWCNTs in the vicinity of the chemical potential. **Left panel:** Fit of the measured curve (dots) with a power law density of states E^α (solid line) with an occupation according to the Fermi distribution at finite temperature (35 K) and smeared out with a Gaussian according to the limited resolution of 10 meV. The fit yields $\alpha = 0.43$. The dotted line corresponds to a constant density of states ($\alpha = 0$) as it would be expected for a Fermi liquid, at the same temperature and resolution. **Right panel:** Linear fit of the photoemission response on a double-logarithmic scale (solid bar). The same α as in the left panel is obtained. The fit was performed between 0.012 and 0.200 eV binding energy.

was set according to the resolution of 10 meV and the temperature was set to 35 K. The measured spectrum is reproduced very well by this function and these parameters in a binding energy region up to 0.2 eV. The resulting power law scaling factor is $\alpha = 0.43$. The TLL coupling constant g which can be obtained from $\alpha = \frac{g+g^{-1}-2}{8}$ is $g = 0.18$. This value is identical within experimental error to that from Ref. [55], where $\alpha = 0.46$ for the power law scaling of the density of states and $\alpha = 0.48$ for the temperature dependence of the photoemission intensity at the Fermi level was obtained. The value of the coupling constant is also in good agreement with theoretical calculations, which predicted a $g \approx 0.2$ [128,129] and consistent with transport experiments through carbon nanotubes (see section 4.2).

Since every power law function results in a straight line on a double-logarithmic scale, such a representation should allow the extraction of the power scaling law factor α as well. The power law coefficient is then simply the slope of the line. In the right panel of Fig. 5.7 the photoemission response is depicted on a double-logarithmic scale. It can clearly be seen, that it forms a straight line which verifies the power law behavior found before with the previous fit method. A linear fit cannot include the deviations from pure power law behavior due to finite resolution and temperature. The analysis therefore has to be restricted to a region where these effects do not play a role. The fit is consequently carried out in the binding energy region from 0.012 to 0.200 eV according to the considerations above. A value of $\alpha = 0.43$ is obtained, which is exactly the same value resulting found in the previous method.

5.4 Conduction band

First experiments on the SWCNT conduction band were carried out by electron energy loss spectroscopy (EELS). The principle is very similar to x-ray absorption spectroscopy as also

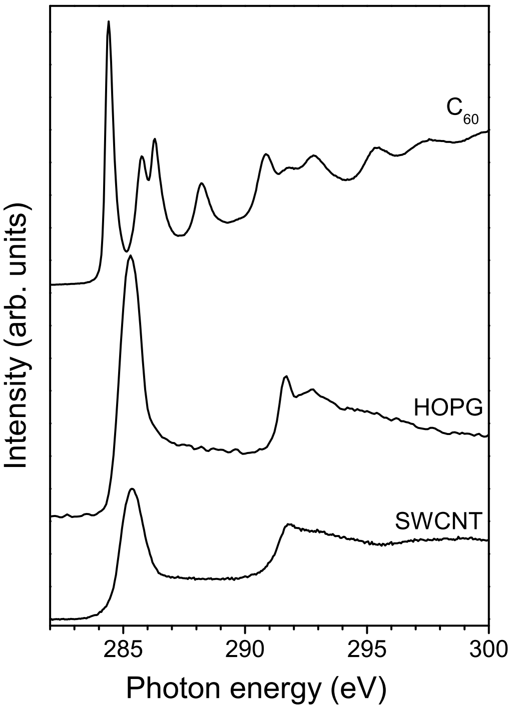

Figure 5.8: Room temperature EELS spectra at the C1s edge from C_{60}, graphite and SWCNTs (From [93]).

excitations into the conduction band are probed. Fig. 5.8 depicts an EELS spectrum of SWCNTs in comparison to graphite and C_{60}. The general shapes of the absorptions from graphite and SWCNTs are very similar. They are determined by absorptions from the $\pi^\star$ and $\sigma^\star$ bands. In both cases, the onset of the $\pi^\star$ absorption can be found at the C1s binding energy of 285 eV, and the maximum absorption is situated approximately 1 eV above the onset. However, the shape of the absorption does not mirror the ground state conduction band, where the $\pi^\star$ band should have a maximum roughly 3 eV above the onset. It is well known from graphite that this discrepancy is due to strong interactions of the final-state electrons with the core hole [143, 144]. These excitonic effects can be accounted for theoretically, e.g. by relaxation of the conduction band states upon the existence of a core hole [145], or by including the electron-hole attraction *ab initio* [146]. Furthermore, the fine structure from the vHs singularities could not be observed in the EELS measurements.

The availability of high-quality samples motivated further investigations. Below, the properties of the SWCNT conduction band studied by x-ray absorption spectroscopy (XAS) are presented. The spectra are acquired at the UE52-PGM beamline at the BESSY synchrotron facility. The SWCNT spectra are not dependent on the angle to the incoming light since the SWCNTs are randomly oriented in the sample. The HOPG spectra were obtained at an angle of 45° to the light beam, ensuring a contribution from both, the π states perpendicular to the surface and the σ states parallel to the surface.

A principal similarity of shape and position of the π and σ bands of the electronic structure of graphite and SWCNTs concerning was found already in the valence band investigation. Significant discrepancies emerged at the low energy side of the π band where peaks originating from the vHs in the electronic density of states were observed. These discrepancies can now also be found in the conduction band. The left panel of Fig. 5.9 depicts the absorption spectra of HOPG and SWCNTs in more detail. In contrast to the HOPG spectrum, the SWCNT spectrum exhibits a clear fine structure on top of the $\pi^\star$ resonance. These peaks are attributed to an increased absorption from the unoccupied vHs in the conduction band, more specifically from the three first vHs of the semiconducting tubes $S_1^\star$, $S_2^\star$ and $S_3^\star$ as well as the first vHs of the metallic tubes $M_1^\star$. In a line shape analysis, the $\pi^\star$ resonance can be deconvoluted into the main peak and four additional peaks. In order to achieve this, the spectrum was fitted with Gaussians, each including a Shirley background proportional to their respective relative intensity.

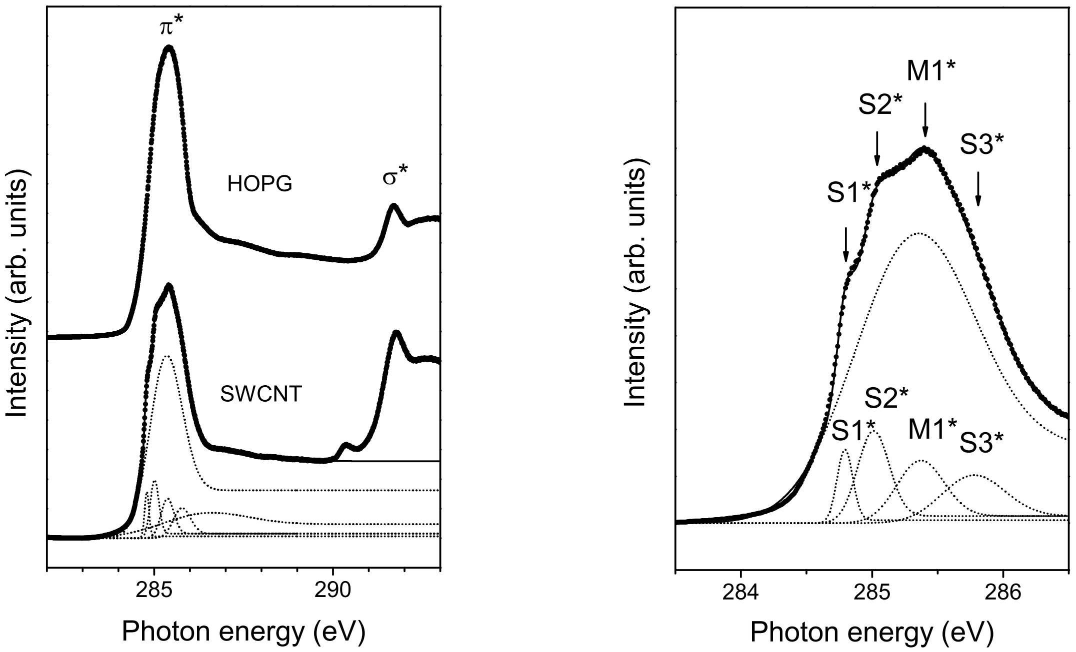

Figure 5.9: X-ray absorption spectrum of SWCNTs at 16 K. Black dots indicate the measured curve, dashed lines represent the fit components. **Left panel:** $\pi^\star$ and $\sigma^\star$ region in comparison to HOPG. **Right panel:**$\pi^\star$ region with fine structure. [147].

The $\pi^\star$ region is depicted in more detail in the right panel of Fig. 5.9. The main peak is situated at 285.3 eV, similar to that of HOPG. The four smaller peaks are assigned to the vHs and labelled accordingly in the figure. They can be found at excitation energies of 284.79 eV ($S_1^\star$), 285.01 eV ($S_2^\star$), 285.36 eV ($M_1^\star$), and 285.76 eV ($S_3^\star$). Considering their relatively low spectral weight compared to that of the main peak, and their location at steep edges of the main peak, a match of their respective relative intensities within a factor of two is satisfactory. Moreover, the width of the peaks increases linearly from 0.14 to 0.60 eV with their location on the conduction band.

5.5 Summary

In this chapter it was shown that the SWCNT sample is well suited for our investigations. The XPS survey showed that no remainders from catalyst particles or other contaminations are present in the sample after heat treatment. Furthermore, XPS measurements of the C1s core level revealed an asymmetric line shape due to the presence of metallic tubes and satellites adjacent to the C1s signal which originate from energy losses of the electrons upon leaving the sample. In addition, the line shape of the carbon Auger electrons was investigated and could qualitatively be explained.

The UPS valence band investigations revealed the π and σ bands typical for carbon materials with sp^2 hybridization. Peaks in the photoemission response, stemming from the van-Hove singularities in the electronic density of states, could also be identified. Finally, the Tomonaga-Luttinger liquid behavior expected for one-dimensional metals was verified by demonstrating the power law scaling of the photoemission response, carefully taking into account experimental limitations. The resulting power law scaling factor $\alpha = 0.43$ and the corresponding Luttinger parameter $g = 0.18$ are in good agreement with previous transport measurements, photoemission experiments and theory.

The valence band structure – including the fine structure related to the van-Hove singularities – is qualitatively well reflected in the conduction band as it is expected for SWCNTs. However, in the conduction band investigations with x-ray absorption spectroscopy, excitonic effects play an important role, leading to a distortion of the response, in particular of the $\pi^\star$ resonance compared to the π band obtained from PES.

6 Electronic properties and metallic ground state of doped SWCNTs

In this section, the electronic properties of intercalated SWCNTs will be investigated with emphasis on the metallic ground state. It was shown above that pristine SWCNTs indeed exhibit properties which can be explained within the model for one-dimensional metals, the Tomonaga-Luttinger liquid. In particular, a renormalization of the electronic density of states at the chemical potential was found. Doping experiments now promise new insight on what happens in the realistic arrangement of SWCNTs – the bundles – upon charge transfer.

EELS measurements discussed in section 2.5 exhibited a charge carrier plasmon in the doped state which was not observed in the pristine state [68]. This hints at a qualitative change in the behavior towards free charge carriers upon doping. The question how such a transition can be explained with the TLL behavior in the pristine state will be discussed in detail. In particular, it will be interesting to see how the TLL behavior evolves upon doping, especially at those dopant concentrations where the Drude plasmon is observed in EELS.

Before this aspect is discussed at the end of this chapter, the influence of the charge transfer on the C1s line shape will be analyzed. The behavior of the main spectral features, the π and σ bands as well as the peaks originating from the vHs in the density of states will be examined in the context of the rigid-band-shift model.

6.1 Core level: C1s

It was shown above that valuable information can be extracted from the C1s line shape even in the pristine state. Upon doping, the investigation of the C1s core level spectra serves two purposes. First, it can be used to determine the actual dopant concentration and second, the line shape contains information on the metallic character of a sample.

6.1.1 Determination of the potassium content

The C1s region can be used to quantitatively analyze the potassium content, or more specifically, the carbon to potassium ratio in the sample. Fig. 6.1 shows that – compared to the pristine case – two additional peaks can be observed in the spectra of the doped SWCNTs, namely at binding energies of 294.7 and 297.4 eV. These peaks are assigned to the potassium states K2p$_{3/2}$ and K2p$_{1/2}$ respectively. The proximity of the C1s and K2p peaks allows them to be measured simultaneously. The actual ratio of carbon to potassium atoms is simply obtained by measuring the areas below the respective peaks. The carbon to potassium ratio can easily be calculated taking into account the different ionization cross sections for the two

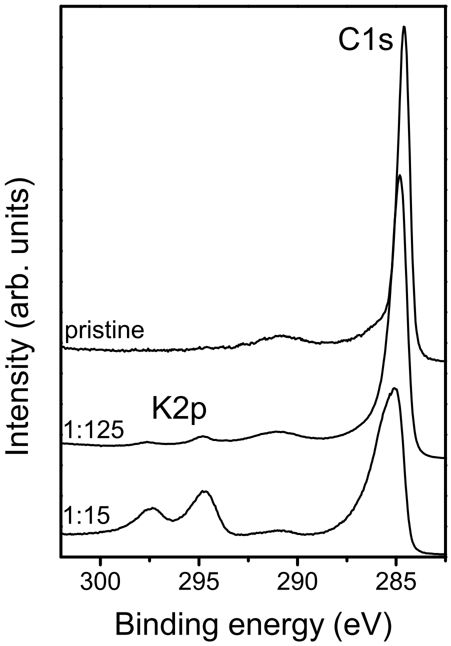

Figure 6.1: C1s core level response of three exemplary doping steps including the K2p region. The K:C values obtained from the quantitative analysis (see text) are given.

elements: 0.0137 for C1s and 0.0537 for K2p . The values given in the figure are obtained by applying this method. However, at the lowest doping steps this method cannot be applied as the K2p response is too weak. Below, a method will be introduced which allows the dopant concentration to be determined at these low doping steps. The dopant concentrations for the doping steps where a K2p peak analysis was possible, are summarized in Tab. 6.2. The highest doping level reached in this thesis is C/K = 15, which is still below the saturation doping found at C/K $\approx$ 7 in SWCNT doping experiments investigated by electron energy loss spectroscopy [68, 148].

6.1.2 Line shape: Increasing asymmetry

Section 5.1 discussed that the slight asymmetry of the C1s XPS response of pristine SWCNTs is caused by the metallic tubes present in the sample. The excitation of low energy conduction electron-hole pairs leads to a low kinetic energy tail of the peak. In this section, the influence of the doping on the C1s line shape will be analyzed in detail. The left panel of Fig. 6.2 shows the doping dependence of the C1s response of SWCNTs as a function of the doping level[1]. The spectra are taken under the same experimental conditions as those of the pristine case in section 5.1. They are normalized to the area below the C1s peak. Two aspects can be observed from the figure. First, the peak position shifts continuously to higher binding energies with increasing doping. The values for the respective doping steps are given in Tab. 6.1. At the highest doping step, the shift amounts to 0.81 eV. The shift can be explained by a Fermi level shift into the conduction band as previously observed by EELS and Raman measurements [68, 89] and similar to the corresponding GICs [149].

---

[1] For clarity only a representative choice of spectra is shown

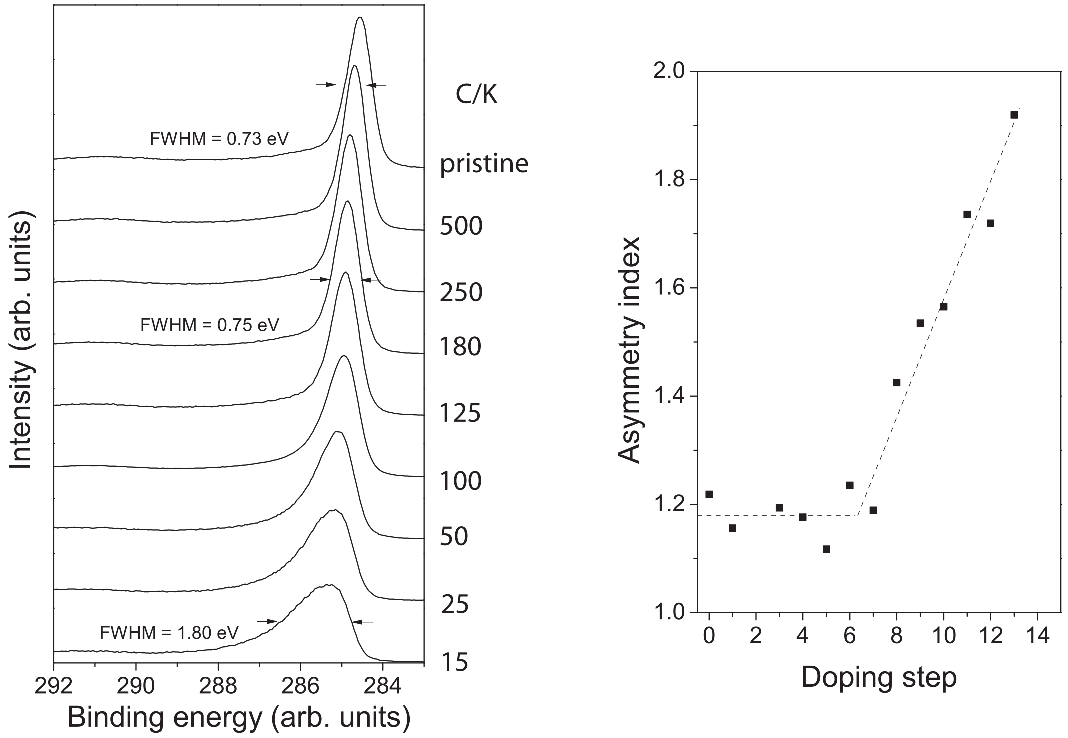

Figure 6.2: Left panel: Doping dependence of the C1s core level response. The numbers denote the doping step. **Right panel:** Variation of the C1s asymmetry index with increasing doping. The dashed lines are guides for the eye. The numbers next to the curves in the left panel and next to the data points in the right panel correspond to the doping steps as they are given in Tab. 6.1.

Second, it is immediately clear that the peak asymmetry at the highest doping steps is much larger than in the pristine state. However, the increase of the asymmetry does not seem to set in immediately on doping. The first four doping steps depicted appear to be very similar as indicated by the similar full width half maximum (FWHM) given in the figure. This aspect can be analyzed in more detail by determining the so-called asymmetry index, which measures the ratio of the distances between the peak maximum and its edge on the high and low energy side of the spectrum respectively. It can be expressed as

$$A = \frac{|E_{1/2}^{\mathrm{high}} - E_{\mathrm{max}}|}{|E_{1/2}^{\mathrm{low}} - E_{\mathrm{max}}|} , \tag{6.1}$$

where $E_{1/2}^{\mathrm{high}}$ and $E_{1/2}^{\mathrm{low}}$ are the energy positions of the peak curve at half the maximum intensity on the high and low energy side of the spectrum respectively and E_{max} is the peak position. The resulting values are summarized in Tab. 6.1 and the right panel of Fig. 6.2 shows them as a function of the doping step. Here, what was already suspected from the examination of the left panel of Fig. 6.2 becomes clear. In the first six doping steps the asymmetry of the C1s peak stays constant within experimental error at values around $A = 1.2$. A only starts to increase significantly at doping step 7. It increases continually from that point until it reaches $A = 1.92$ at the highest doping step.

The peak asymmetry is a measure of the “metallicity” of a material. It depends on the number of low energy electron-hole pairs, which are excited, and it is easily conceivable that the amount of these excitations depends on the DOS near the Fermi level. When it stays

Doping step	C1s peak pos. (eV)	Peak shift (eV)	Asymmetry index	C/K (rounded)
pristine	284.55	0	1.22	-
1	284.61	0.06	1.16	-
2	284.67	0.12	1.19	-
3	284.80	0.25	1.18	-
4	284.80	0.25	1.12	500
5	284.85	0.30	1.23	250
6	284.91	0.36	1.19	180
7	284.95	0.40	1.42	125
8	285.08	0.53	1.53	100
9	285.10	0.55	1.57	75
10	285.21	0.58	1.73	50
11	285.21	0.66	1.73	25
12	285.27	0.72	1.72	20
13	285.36	0.81	1.92	15

Table 6.1: Values obtained from the C1s line shape analysis.

constant, the asymmetry also remains constant. This situation changes upon doping. Very similar to the EELS measurements discussed above (see Fig. 2.10), the sample seems to become more metallic. This further motivates the investigation of the metallic ground state upon doping.

However, there are other possible causes for the peak asymmetry. As discussed for the pristine SWCNTs, the exact position of the respective Fermi levels of metallic and semiconducting tubes is determined by contact potentials between the tubes in the bundles. It is thus not necessarily identical. Similarly, the shift of the Fermi level of the two types of nanotubes does not have to be equal. Indeed, it will be shown below that the binding energy of the vHs shifts differently for the metallic and the semiconducting tubes (see Fig. 6.5 and Tab. 6.2). Then again, this effect is strongest at the first few doping steps, in a range where the asymmetry does not change much. Furthermore, the highest value of the difference in shifts is 0.2 eV (doping step 5). First, at this step, the asymmetry is still unchanged and second, it is expected that the shift difference will not increase much more, if at all, at higher doping steps. If the asymmetry was caused by different binding energies of the C1s state from metallic and semiconducting tubes, this difference would have to be much larger as can be seen from the great width of the C1s response at higher doping steps (e.g. a FWHM of 1.80 eV at the highest doping step).

6.2 Valence band properties at low and medium doping levels

The valence band photoemission response of pristine SWCNTs (section 5.2) was in good agreement with the expected electronic band structure. The π and σ bands were identified at binding energies of 3.2 and 8.6 eV binding energy respectively. Furthermore, peaks originating from the vHs of the metallic and semiconducting tubes in the sample were observed. In the following section, the doping dependence of the SWCNT valence band will be investigated and compared to known results on other carbon compounds such as GICs and FICs.

Valence band region

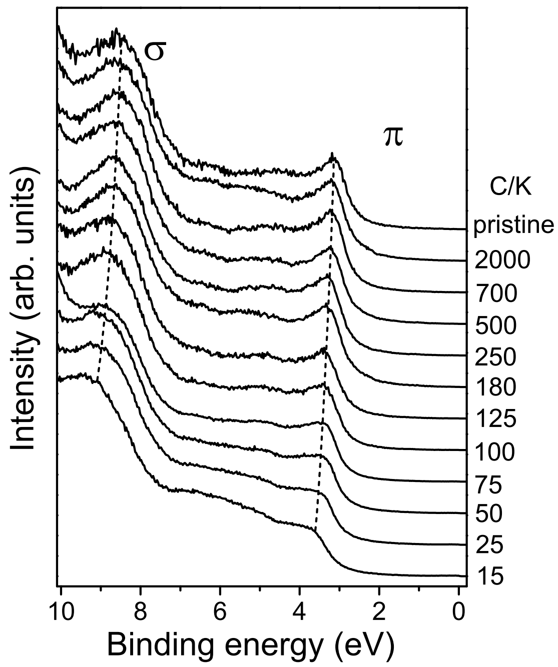

Figure 6.3: Doping dependence of the valence band region of SWCNTs. The doping level increases from top to bottom, starting with the spectrum of pristine SWCNTs. The dashed lines indicate the gradual shift of the π and σ peaks and the numbers correspond to the C/K ratio.

Fig. 6.3 shows the doping dependence of the SWCNT valence band. The π and σ bands can be identified at all doping steps. The overall spectrum remains qualitatively the same. With increasing charge transfer, the π peak becomes broader and shifts gradually to higher binding energies. The broadening can be caused by the increasing number of potassium counter-ions which act as scattering centers. The σ band shifts in the exactly the same way. At the highest doping step (C/K = 15), the shift of both peaks amounts to about 0.8 eV. This is the same shift which was observed for the C1s peak. The doping behavior can thus again be explained within the rigid band shift model. Nevertheless, the σ peak does not broaden significantly. This might be because the peak itself is already considerably broader than the π peak so that effects which cause additional broadening do not play an important role.

SWCNT fine structure

The focus will now be shifted to the region closer to the chemical potential. In the pristine case, three peaks from the van-Hove singularities were observed in the density of states, two from the semiconducting tubes (S_1 and S_2) and one from the metallic tubes (M_1). In Fig. 6.4, their behavior upon doping is depicted for the case of low doping. As it was already the case for the π and σ bands, these peaks shift gradually to higher binding energies. It was discussed above that the exact position of the Fermi level is determined by contact and impurity potentials between the tubes in the bundles. The exact position of the Fermi level

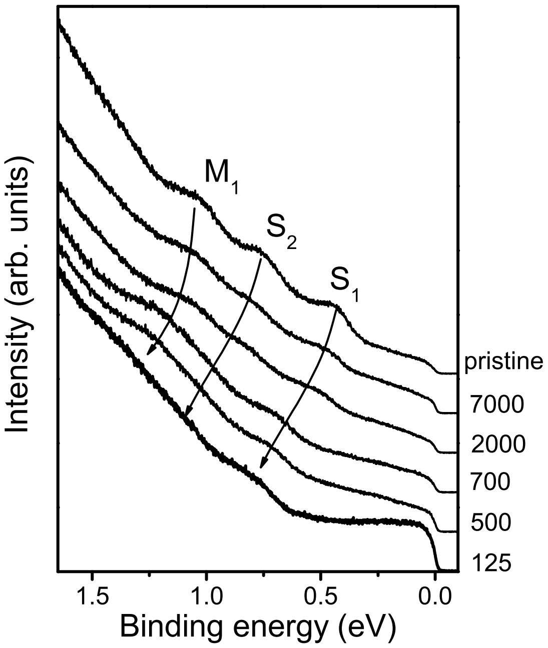

Figure 6.4: Doping dependence of SWCNTs in the region below the π band. The doping level increases from top to bottom, starting with the spectrum of pristine SWCNTs. The numbers indicate the C/K ratio obtained from either the K2p/C1s ratio or the shift of the first vHs of the metallic tubes M_1 as described in the text. The peaks originating from the vHs in the density of states are labelled and the arrows indicate their shift upon doping.

and its evolution upon doping can thus become rather complex. Fortunately the fact that features from both the semiconducting and the metallic tubes can be observed facilitates the analysis. Fig. 6.5 shows a comparison of the vHs peak positions and their behavior upon doping. The amount of the shift is the same for the two peaks from the semiconducting tubes[2]. The shift of the peak from the M_1 vHs is considerably smaller than that of S_1 and S_2 at the first four doping steps. The amount of the shift only becomes similar after this. The different shift of the vHs peaks from the semiconducting tubes causes the S_2 and the M_1 peaks to converge. At the higher doping levels depicted in figreffig:swdop-vhs M_1 cannot be separated anymore from S_2 which is also due to the broadening of the peaks upon doping. In general, the shift of the peaks from the vHs can be explained again by a gradual filling of states in the conduction band which shifts the chemical potential. However, this is a good example that the Fermi level shift is not equal for both types of tubes.

Interestingly, the slope of the shift of peak from the metallic vHs approaches that of the peaks from the semiconducting tubes after the fifth doping step. This is also the point where the asymmetry of the C1s peak increases, which was attributed to an increase of the density of states at the Fermi level, caused by a filling of conduction band states of the semiconducting tubes. At this point we can even relate this doping step to a Fermi level shift of these tubes. Between doping step four and five the vHs shift increases from 0.20 eV to 0.30 eV. At the lower doping steps discussed here, only states of the metallic tubes are filled. States in the conduction band of the semiconducting tubes start with the first unoccupied vHs $S_1^\star$. In the investigation of the properties of pristine SWCNTs in section 5.2, a rough approximation based on the vHs peak positions led to the estimation that the $S_1^\star$ vHs is

---

[2] Since plotting as a function of doping steps is arbitrary, the somewhat linear behavior has no further physical meaning.

situated about 0.2 eV above the Fermi level. It is thus more than reasonable to assume that at least those semiconducting tubes with a smaller diameter are doped highly enough to become metallic between the doping steps four and five. At those doping steps where all tubes in the bundle are metallic the Fermi level obviously shifts equally for all tubes. However, the respective band structures of the semiconducting tubes are not symmetrical to each other at these doping steps as can be concluded from the closeness between S_2 and M_1 as opposed to the greater distance between S_1 and S_2. These distances should be the same in a symmetrical band structure.

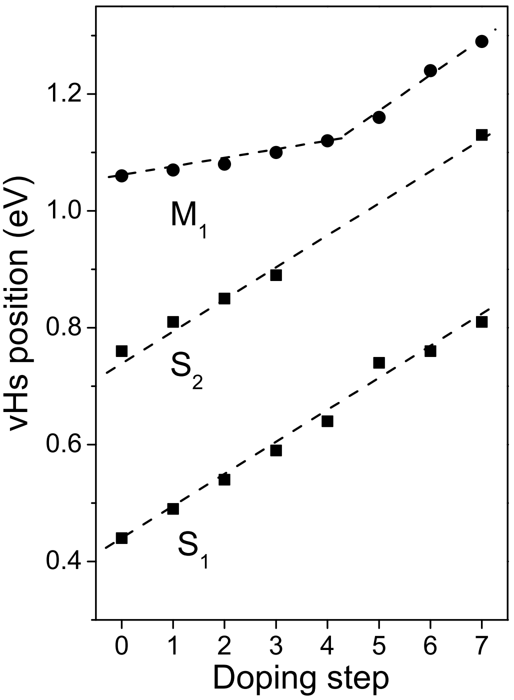

Figure 6.5: Comparison of the shifts of the S_1 and S_2 vHs of the semiconducting tubes and the M_1 vHs of the metallic tube. The dashed lines are guides for the eye.

Determination of the potassium concentration at low doping levels

In section 6.1.2 it was demonstrated how to obtain the potassium concentration in the sample by comparing K2p to C1s responses. At very low doping levels, the potassium concentration cannot be obtained because the K2p peak is too weak. However, the potassium content can be estimated via the shift of the van-Hove singularities in this region. Due to the constant density of states, this shift should be in a linear relation between the charge transfer and the shift of the vHs. This linear relation can be derived from those doping steps where the shift of the vHs and the K2p peak intensity can be obtained at the same time. This is not the case for those very low doping steps, or even for higher doping steps at which the vHs disappear, as will be seen below. Obviously, the M_1 vHs has to be used for this analysis since at first only states of the metallic tubes are filled. All in all, four doping steps meet this condition and the resulting dependence of the charge transfer on the shift of the M_1 peak is depicted in Fig. 6.6. As expected for a constant density of states, the four points exhibit a linear behavior which can then be fitted. The resulting slope of 0.034 e^-/eV allows us now

Step	S_1 / eV	S_2 / eV	M_1 / eV	C/K
pristine	0.44	0.76	1.06	∞
1	0.49	0.81	1.07	7000
2	0.54	0.85	1.08	2000
3	0.59	0.89	1.10	750
4	0.64	-	1.12	500
5	0.74	-	1.16	250
6	0.76	-	1.24	180
7	0.81	1.13	1.29	125

Table 6.2: Overview of the values derived from the respective doping steps of SWCNTs: Position of the first vHs of the semiconducting (S_1 and S_2) and first metallic (M_1) tubes, and the carbon to potassium ratio (C/K) derived from the vHs shift (see text). Empty fields: The values of the S_2 peak position could not be determined at these steps, since the peak cannot be distinguished from the onset of the M_1 peak.

to estimate the charge transfer from the vHs shift for the remaining low doping steps. The results are given in Tab. 6.2.

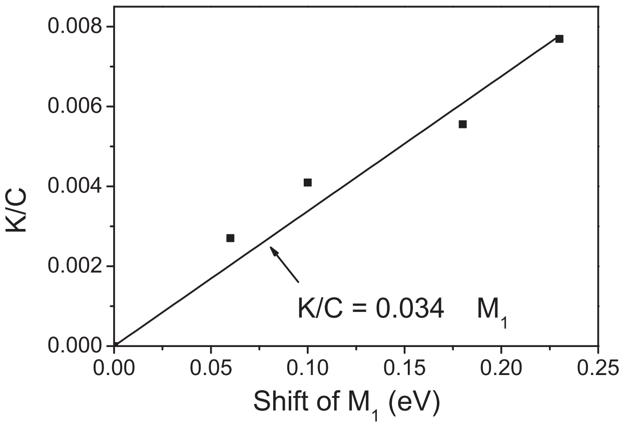

Figure 6.6: Relation between charge transfer obtained from the K2p to C1s ratio and the shift of the first van-Hove singularity of the metallic tubes, M_1. The squares are the measured values, the line represents the linear fit. The slope of the fit, 0.034 e^-/eV, is also the value of the density of states of the metallic tubes.

We can also compare this result to theoretical values. When ionic charge transfer is assumed, this value is also the value of the density of states of the metallic tubes at the Fermi level. As seen in Chapter 1, the density of states of metallic tubes per unit length along the nanotube axis within the simplest tight-binding model is a constant given by

$$N(E_F) = \frac{8}{\sqrt{3}\pi a \gamma_0}. \tag{6.2}$$

For a metallic (10,10) nanotube, which has 40 carbon atoms in a unit cell of a length of 2.46 Å and a $\gamma_0 = 2.5$ eV, we obtain $N(E_F) = 0.025\ e^-$/eV. This value is in relatively good agreement with our experimentally obtained one and thus allows an estimation of the lowest doping levels by measuring the shift of the vHs.

Another observation concerns the spectral weight at the Fermi level. As was discussed for the pristine case, it is suppressed to a certain extent due to the power law scaling of the electronic density of states. In Fig. 6.4, this suppression of spectral weight seems to be retained at the next doping steps. The shape of the spectrum only changes at the doping steps corresponding to C/K = 500 and C/K = 125. First, the intensity of the response at the Fermi level increases. This indicates that the region with a constant density of states is being left. Second, the shape of the response also changes. Especially for C/K = 125 the typical shape of the power law can no longer be observed, instead it resembles a Fermi edge. This behavior will be investigated in more detail in the next section.

6.3 Crossover from a Tomonaga-Luttinger liquid to a Fermi liquid

In the following section, the influence of doping on the spectral response in the close vicinity of the chemical potential will be investigated in detail. This investigation will provide insight into several important aspects. The possible existence of a pseudogap and – more importantly – the question as to what happens to a bundle of semiconducting and metallic tubes upon doping, especially when the doping is high enough to also make the semiconducting tubes metallic, are discussed.

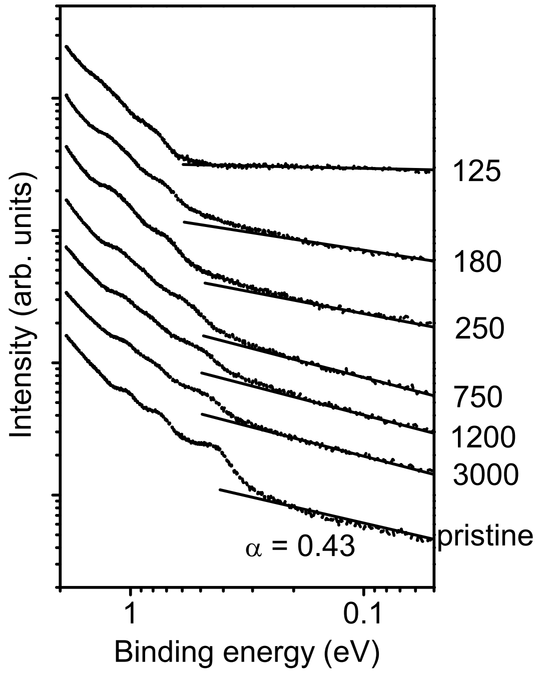

Figure 6.7: Double-logarithmic representation of the spectral response of SWCNTs near the Fermi level (dashed curves). The solid lines represent the linear fit which yields the power law scaling factor α. The numbers beside the graph indicate the respective C/K values.

First principle studies of a bundle consisting of only (10,10) metallic SWCNTs lead to the prediction of a pseudogap,[3] caused by the interaction between the tubes in the bundle [150–152]. Scanning tunneling spectroscopy experiments on armchair and zigzag tubes in bundles do show such a pseudogap of 0.03 - 0.08 eV, depending on the tube diameter, which was not observable in the isolated tubes [153]. However, more realistic calculations for a SWCNT bundle with a random composition of metallic and semiconducting tubes of varying diameters [154] lead to the conclusion that the effect on the density of states is

---

[3] The term *pseudogap* is used because the density of states does not vanish completely but remains at a finite value, although strongly suppressed.

negligible. The doping experiments presented here can serve to remove remaining doubts by shifting the Fermi level beyond the pseudogap region and investigating the consequences on the photoemission response. One important observation in this regard has already been made in the previous section where it was noted that the spectral weight at the Fermi level does not change significantly upon doping.

The second aspect which can be investigated upon doping is the metallic ground state. In the pristine state, a power law scaling factor α of the electronic density of states, typical for TLL behavior, was obtained by a linear fit on a double-logarithmic scale. The same procedure can now be applied to the various doping steps. The results are depicted in Fig. 6.7 where the photoemission response of SWCNTs is represented on a double-logarithmic scale. Here it is clearly evidenced that the linear behavior – indicated in the figure by the solid lines – is stable upon doping on this scale. It is thus concluded that the metallic SWCNTs in the bundle are Luttinger liquids also at low doping. At this point it can also be noted that not only the spectral weight but also the exact shape of the spectrum is retained, while the Fermi level of the metallic tubes in the bundle is shifted by about 60 meV, well beyond the region where a pseudogap was expected. The largest value of the gap measured by STS was 80 meV for a (9,0) tube, so that a Fermi level shift of 40 meV should close this gap. Additionally, this value was obtained for tubes significantly smaller than the ones in our sample, with larger tubes exhibiting a much smaller gap. It can thus be ruled out that the suppression of photoemission spectral weight at the chemical potential is due to a pseudogap caused by interactions between the tubes in the bundle.

Step	ΔS_1 / eV	C/K	α
pristine	0	∞	0.43
1	0.05	7000	0.46
2	0.10	2000	0.45
3	0.15	750	0.47
4	0.20	500	0.46
5	0.30	250	0.37
6	0.32	180	0.30
7	0.37	125	≈ 0

Table 6.3: Overview of the values derived from the respective doping steps of SWCNTs: Shift of the first vHs of the semiconducting (ΔS_1) tubes, carbon to potassium ratio (C/K) and the power law scaling factor α derived from the linear fit on the double- logarithmic scale.

The slope of the linear fit – and thus the value of α – appears to be the same for the first few doping steps. However, at the highest doping step depicted, the line is nearly horizontal. In order to analyze this observation in more detail, the exact values of α are obtained by the linear fit and are summarized in Tab. 6.2. Fig. 6.8 depicts these values as a function of the charge transfer K/C which is the inverse of the C/K ratios given in Tab. 6.3. For doping levels ≤ 0.002 e^-/C (steps 1-4), indeed no change is observed in the TLL parameter within experimental error. At the highest of these doping steps, the peak from the first vHs of the semiconducting tubes, S_1 is already shifted by 0.20 eV. Upon increasing doping α, starts to decrease (steps 5 and 6) until it finally reaches zero at doping step 7. At this doping step S_1 is shifted by 0.37 eV.

This behavior can be further interpreted by taking a closer look at the band structure of the SWCNTs. A simple sketch of both the band structure (left panel) and the elec-

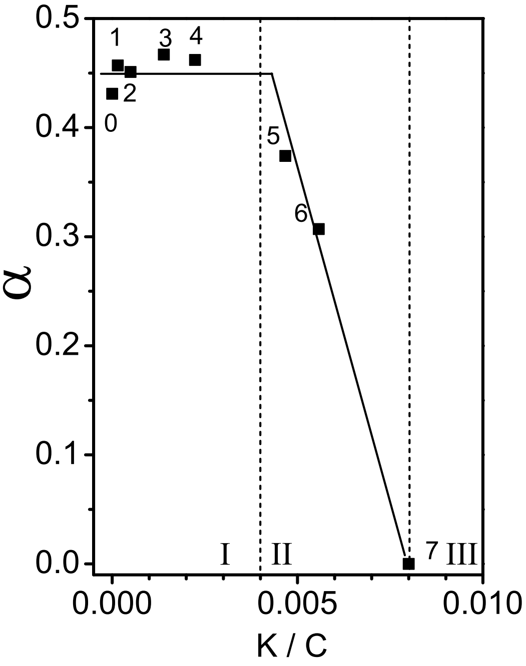

Figure 6.8: Dependence of the TLL power law scaling factor α on the charge transfer. The numbered black squares represent the values obtained from a linear fit of the spectra on a double-logarithmic scale of the respective doping steps. The black lines are arbitrary guides for the eye. The numbers denote the doping steps as given in Tab. 6.3. The dashed vertical lines separate the three doping regions labelled with roman numerals (see text and compare Fig. 6.9).

tronic density of states (right panel) of metallic and semiconducting SWCNTs derived from tight-binding calculations is given in Fig. 6.9. In both cases, the black lines represent the semiconducting tubes and the grey lines represent the metallic tubes. As shown above, that the doping behavior of the π and σ bands as well as the shift of the vHs to higher binding energies could well be explained within a rigid band shift model. This model is now applied by assuming that the doping leads to a shift of the Fermi level into the conduction band (indicated in the figure by the arrow) without substantially changing the band structure itself. The doping dependence is divided into three parts according to ranges of the Fermi level shift in the electronic structure. These parts are labelled with roman numerals in the Figs. 6.8 and 6.9.

At the first four doping steps, α is basically unchanged. In this region, the first vHs of the semiconducting tubes S_1 is shifted by 0.20 eV. This regime is indicated in the band structure representation in Fig. 6.9 by the lightly shaded region labelled with I. Only states in the conduction band of the metallic tubes are filled, the semiconducting tubes remain semiconducting and the metallic SWCNTs in the bundle remain Luttinger liquids. This also means that the long range Coulomb interaction is essentially unaffected by the potential of the counter-ions. The results are in good agreement with predictions which show that for a TLL in metallic nanotubes the power law scaling parameter α is not affected until the first vHs of the conduction band of the metallic tubes, $M_1^\star$, is reached so that additional conduction channels are possible [130]. Furthermore, this behavior is consistent with the observations on the C1s asymmetry which also did not change at these low doping steps.

At intermediate doping steps 5 and 6, α starts to decrease. The corresponding range in the band structure is given by region II, shaded darkly in the figure. In this region, the Fermi level is shifted highly enough to also fill states in the conduction band of the semiconducting tubes. This can be substantiated by two facts. First, the shift of the S_1 peak amounts to only 0.07 eV, while the additional charge which is transferred in this region is only slightly

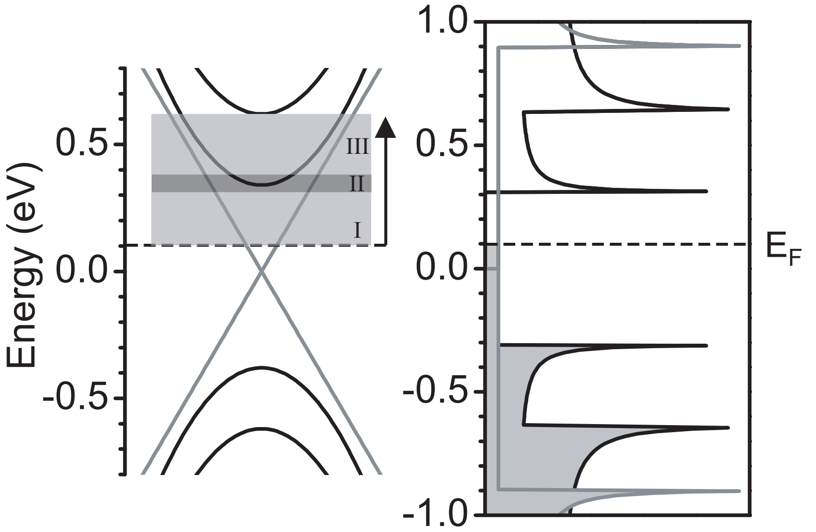

Figure 6.9: Schematic view of the SWCNT electronic structure. Grey lines indicate contributions from the metallic SWCNTs and black lines are contributions from semiconducting SWCNTs. The dashed lines represent the Fermi level in the pristine case. Note that in this illustration the Fermi level shift already caused by charge carrier injections from the substrate in the pristine case has been taken into account. **Left panel:** Band structure of SWCNTs. The three different doping regimes described in the text are indicated by different shading. The direction of the Fermi level shift is given by the arrow. **Right panel:** Density of states of SWCNTs. The shaded area indicates filled states in the pristine case.

less than in region I, where the charge transfer led to $\Delta S_1 = 0.30$ eV. This means that with roughly the same amount of charge more states have to be filled which consequently leads to a lower shift of the Fermi level. Since metallic tubes have a constant density of states up to $M_1^\star$ which is expected about to be approximately 1 eV above the Fermi level, the increase of states can only be ascribed to the semiconducting tubes. Second, this increase of states can also be monitored simply by the increase of photoemission spectral weight at the Fermi level. Since the tubes in the sample have a finite diameter distribution and thus slightly different positions of the vHs (see above), the charge transfer leads to the filling of states in the conduction band of the semiconducting tubes with the largest diameter first. Thus, some of the tubes which are semiconducting in the pristine state are made metallic but the sample remains a mixture of semiconducting and metallic tubes, but with a greater proportion of the metallic tubes.

Finally, at doping step 7, corresponding to a C/K = 125, α reaches zero. The electronic density of states is thus a constant ($E^0 = 1$), which is exactly the density of states of a Fermi liquid. Fig. 6.4 shows that at the same time, the shape of the photoemission response around zero binding energy resembles a Fermi edge, an observation which is supported by the higher doping steps presented below. The drop of α to zero and the evolution of a Fermi edge happen at a shift of the S_1 vHs of 0.37 eV, which is the point where the vast majority of tubes which were semiconducting in the pristine state have been made metallic by filling states in their conduction band (region III in Fig. 6.9). At this point, the striking analogy to the evolution of the C1s peak asymmetry upon doping as discussed above, should be noted. As illustrated by Fig. 6.2, the asymmetry, which is an approximate measure for the amount of metallic tubes in the sample, starts to increase at the same doping levels where α starts to decrease, further supporting the conclusion that the decrease of α can be attributed to making previously semiconducting tubes metallic.

Obviously, the behavior of a bundle of now only metallic tubes no longer exhibits the power law scaling typical for one-dimensional metals. Instead, a Fermi liquid behavior, typical for metals in three dimensions, is observed. This signifies that – although every individual nanotube in the bundle is still a one-dimensional object – the overall one-dimensional behavior is destroyed in favor of a three-dimensional Fermi liquid behavior. Possible explanations can be found in an increasing hopping between the tubes in the bundle, which, according to theoretical works [120], leads to a crossover from a TLL to a FL. In addition, the long-range Coulomb interaction between the charge carriers can be screened by neighboring tubes.

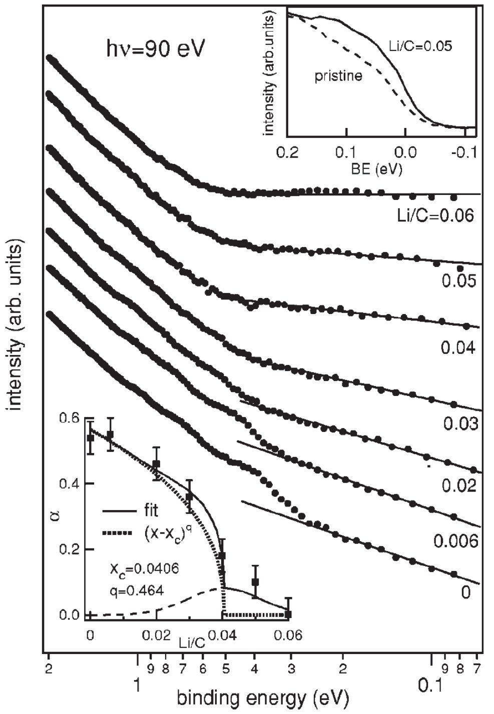

Figure 6.10: Double-logarithmic representation of the photoemission spectra measured near the Fermi energy on pristine and Li doped SWCNTs. The fits up to 0.2 eV provide the values plotted vs the Li/C ratio in the bottom inset. In the top inset the valence band shapes measured on pristine (rescaled) and doped (Li/C = 0.05) SWCNTs are compared. Figure from [155].

The results can thus be interpreted as a doping-induced crossover from a TLL to a FL in bundles of SWCNTs. These results were recently confirmed by Li-doping experiments on mats of SWCNTs [155]. Fig. 6.10 illustrates that a similar transition from TLL to FL was observed as a function of Li-concentration. The power law behavior was confirmed on the double-logarithmic scale and α decreased upon doping although a different slope of α was observed. Very similar behavior was also observed in transport experiments on MWCNTs [156]. The electronic states can be tuned in the sense that the Fermi level is shifted through the band structure, i.e. similar to the chemical doping described above, by applying a gate voltage through a back gate. Transport through MWCNTs is equally characterized by power law behaviors but its origin is still unclear. Both a TLL behavior and a non-conventional Coulomb blockade regime can explain the results (see section 4.2). The power law scaling is obtained by measuring the temperature-dependent conductance which is found to behave as $G(T) \sim T^{\alpha}$. Fig. 6.11 shows the dependence of the power law exponent α on the gate voltage. Without the presence of the gate voltage, $\alpha = 0.64$ is found. α decreases with increasing gate voltage until finally a temperature-independent conductance with $\alpha = 0$ is observed, as expected for a Fermi liquid. This decrease of α

can be explained with an increasing number of conduction channels: Whereas only the outermost shell of the MWCNTs contributes to the conductance at zero gate voltage, an increasing gate voltage leads to a contribution of more shells, thereby effectively decreasing α. Another possible explanation is that more and more shells are rendered metallic and increasing hopping or screening of Coulomb interactions leads to a more three-dimensional behavior.

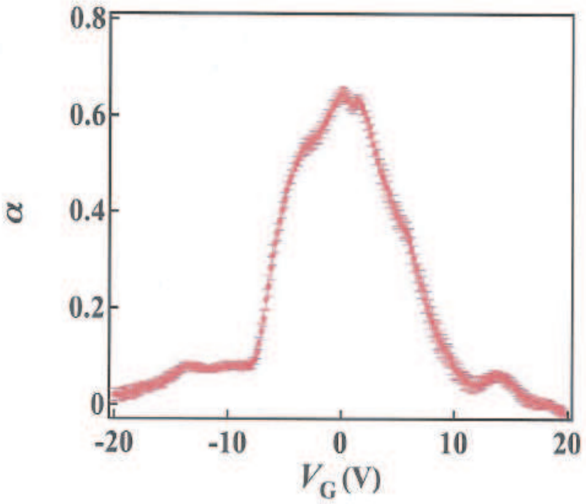

Figure 6.11: Correlation between the power law exponent α and the gate voltage in an end-contacted MWCNTs [156] (see text). The α values were estimated from the slope of log G vs log T plots.

6.4 High doping

The final aspect of the doping behavior of SWCNT bundles to be discussed are the high doping steps. Fig. 6.12 depicts the results of the UPS measurements. Here the spectra from C/K = 180, the last doping step where a finite power law exponent α could be obtained up to a doping level of C/K = 15, the highest achievable doping step, are shown.

The most obvious observation is the significant increase in spectral weight at the Fermi level upon doping. Especially at doping levels C/K = 100 and higher, a clear Fermi edge can be seen. The photoemission response drops rapidly from a finite value to zero at the Fermi level. As an example, the spectrum of the highest doping level was fitted with a Fermi function which was broadened by a Gaussian distribution to incorporate the finite temperature and resolution. The procedure is the same as in section 5.3, where the spectrum of the pristine SWCNTs was fitted with a power law, only that in this case α was set to zero in order to obtain a constant density of states. Fig. 6.13 depicts the resulting fit of the highly-doped SWCNT response. When the actual parameters from the experiment to describe finite temperature and resolution are used, the photoemission response of the highly doped SWCNTs is described very well by the Fermi function fit, further proving the assumption that instead of a one-dimensional TLL, a bundle of only metallic SWCNTs is a three-dimensional electronic system which exhibits Fermi liquid behavior. This is also in very good agreement with the emergence of a free charge carrier plasmon observed in EELS measurements [68] and the strong asymmetry of the C1s response which indicates metallic behavior and a strong density of states at the Fermi level. In addition, the increase of the asymmetry starts at the same doping step where the metallic ground state began with a crossover from a TLL to a FL.

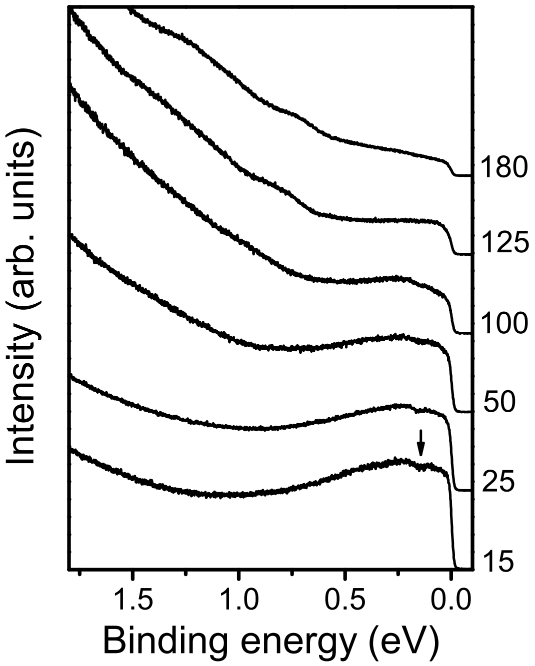

Figure 6.12: Photoemission response near the Fermi level for high doping levels. The numbers give the C/K ratio and the arrow indicates the position of the electron-phonon coupling satellite as described in the text.

The peaks originating from the van-Hove singularities in the density of states can still be identified at the two lowest depicted doping steps, although they are already broadened compared to the pristine state. Upon increasing charge transfer, they broaden even more and finally vanish completely. This can be explained by effects such as an increasing number of scattering centers (K^+ counter-ions) and increasing inter-tube interaction within the SWCNT bundle in the intercalation compound. The overall shape of the spectra of these highly doped samples is also very similar to the corresponding GIC [149].

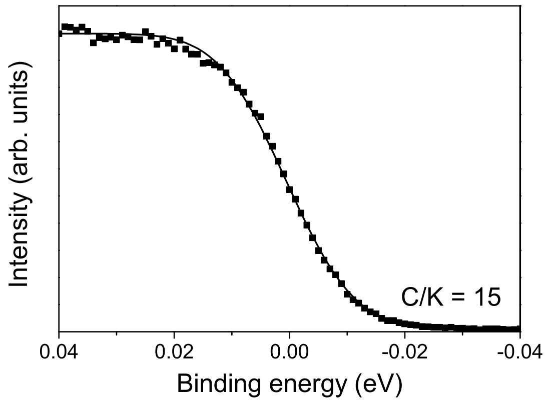

Figure 6.13: Fit of the photoemission response of the highest doping step (C/K = 15, black squares) with a Fermi function broadened by a Gaussian distribution (solid line).

According to our discussion in the previous section, at doping levels of C/K = 125 and higher, states in the conduction band of the previously semiconducting tubes are also filled. Interestingly, no sign of the van-Hove singularities can be observed in the conduction band (especially $S_1^\star$). On the other hand a satellite in the photoemission response occurs at about 200 meV (marked by the arrow in the figure) for all highly doped samples, which is very close to the frequency of the G-Line of the doped SWCNTs[4] [89]. Hence, it is tempting to explain this as a redistribution of the spectral weight by electron phonon coupling. This explanation is also supported by the close analogy of the line shape to the low temperature photoemission spectra of the metallic C_{60} intercalation compound K_3C_{60}, which is dominated by strong satellites due to coupling to phonons and to the charge carrier plasmon [137]. In addition, the strong electron-phonon coupling also explains the absence of the above-mentioned photoemission peaks related to the $S_1^\star$, $S_2^\star$, and $M_1^\star$ vHs. Together with a coupling of the electrons to the aforementioned plasmon it causes a strong broadening of these peaks.

6.5 Summary

The doping behavior of bundles of high purity SWCNTs with a narrow diameter distribution was analyzed in this chapter. Using photoemission spectroscopy, the different spectroscopic features in the valence band and the core level states were analyzed. The results of the n-type doping experiments presented in this chapter can be explained well within the rigid band-shift model, i.e. the charge transfer from the intercalant leads to a filling of previously unoccupied states and the Fermi level shifts continuously into the conduction band without a change in the band structure itself. The shift was monitored by gradual increases of the binding energy of the C1s states and the π and σ bands. The shift of the Fermi level was even be observed individually for the metallic and semiconducting tubes respectively by analyzing the change of the respective vHs binding energies upon doping. It was found that the Fermi level of the two types of tubes does not change synchronously.

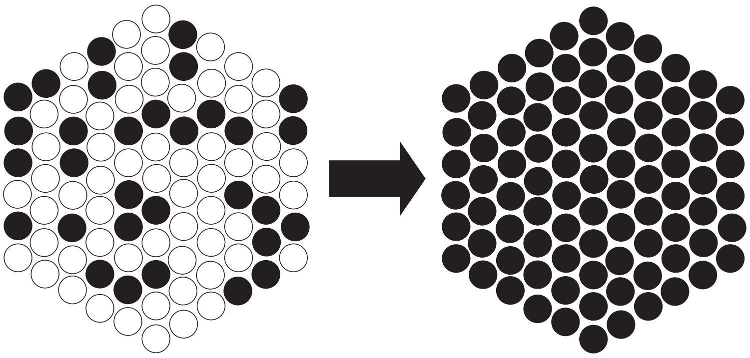

Figure 6.14: Schematic view of an undoped SWCNT bundle (left) consisting of 1/3rd semiconducting (open circles) and 2/3rd metallic (black circles) tubes which is transformed to a bundle consisting only of metallic tubes (right).

The key point of the investigations was what happens if a bundle which consists of a mixture of semiconducting and metallic tubes in the pristine case is doped high enough, that the semiconducting tubes become also metallic. This situation is illustrated in Fig. 6.14. Two important observations were made in this regard, the first of which concerns the asymmetry of the C1s peak. The asymmetry stays constant at the first few doping steps and

---

[4] The G-line is usually found in Raman spectroscopy around 1590 cm^{-1}. 1 eV corresponds to 8086 cm^{-1}, the G-line energy is thus 197 meV.

then increases continuously, indicating an increasing density of states at the Fermi level for the whole system. The second observation concerns the TLL power law scaling factor α which is a fingerprint of whether a metal exhibits a one-dimensional or three-dimensional behavior. Just like the C1s peak asymmetry, it stays constant at first. It then starts to decrease at exactly the doping level, where an initial filling of the semiconducting tubes conduction band is to be expected from the shift of the vHs peak of these tubes. Upon further doping, all semiconducting tubes have finally been made metallic by a filling of states in their conduction band. At this point, α reaches zero, which is synonymous for Fermi liquid behavior in TLL theory. At the same time, the evolution of a clear Fermi edge can be observed. Interestingly this development takes place at the same doping steps where the increase of the C1s peak asymmetry sets in. This further supports our conclusion that both effects are due to a shift of the Fermi level into the conduction band of the semiconducting tubes so that all tubes in the bundle are metallic.

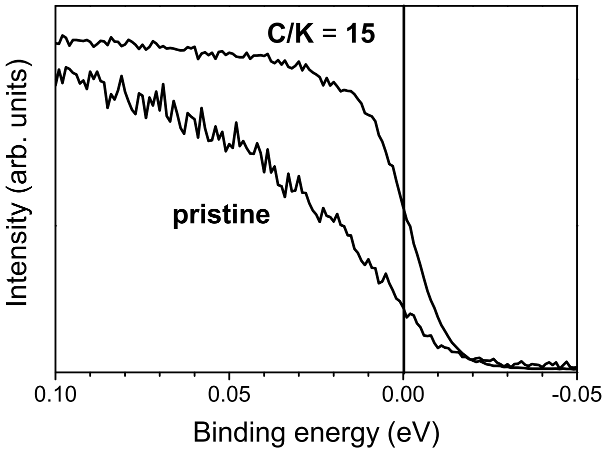

Figure 6.15: Spectral response from SWCNTs in the pristine and highly doped state (C/K = 20). The spectrum according to the pristine state is upscaled for clarity.

The metallic character remains on further doping, the density of states at the Fermi level increases concomitant with the evolution of a charge carrier plasmon observed in EELS and the increasing line width of the C1s peak. Hence the overall behavior can be interpreted as a crossover from a one-dimensional Tomonaga-Luttinger liquid to a three-dimensional Fermi liquid. This transition is caused by a strong screening of the Coulomb interaction between charge carriers in neighboring nanotubes and/or by the fact that in a bundle of metallic tubes only, the hopping matrix element between the tubes is strongly enhanced, thus yielding a more three-dimensional electronic structure. Fig. 6.15 once again illustrates this crossover by opposing the spectra of the pristine SWCNTs which exhibit TLL behavior with the highly doped spectrum which, clearly displays a Fermi edge typical for three-dimensional metals.

7 Electronic properties of pristine and doped C_{60} peapods

The previous chapter showed how a controlled modification of the electronic structure of a bundle of SWCNTs led to a qualitative change in the nature of the metallic ground state. The filling of SWCNTs is another way to modify the properties of SWCNTs. It was shown that new electronic states which originate from the C_{60} filling are introduced in the hybrid system.

In this chapter, the interplay of the respective electronic structures of C_{60} and SWCNTs will be a subject of investigation. Furthermore, the influence on the metallic ground state will be analyzed. This is of particular interest since the properties of the TLL behavior are predicted to change upon the emergence of new conduction bands. The role of these bands will first be studied in the pristine case. A doping series similar to that performed on SWCNTs will give insight into the way the charge transfer modifies the collective electronic structure of the compound. This behavior will be compared to that of its individual constituents. Again, special emphasis is placed on the analysis of the TLL behavior upon doping. In particular, the states of the C_{60} filling in the conduction band have to be considered. The possibility of C_{60} chains forming one-dimensional conduction channels upon doping is discussed.

7.1 Electronic structure of pristine C_{60} peapods

Valence band properties of C_{60} peapods

In order to elucidate the questions raised above concerning the properties of the electronic structure of C_{60} peapods, PES experiments were carried out in the valence band region. Fig. 7.1 shows the UPS spectrum of C_{60} peapods in comparison to those of SWCNTs and solid C_{60}. The spectra are taken at 21.1 eV excitation energy.

As discussed previously, the SWCNT response consists of contributions from the σ- and π-bands which represent the strong in-plane bonding and the weak bonding perpendicular to the graphene plane respectively. These features are observed equally in the C_{60} peapod spectrum and this at exactly the same binding energies as in SWCNTs, i.e. at 3.1 and 8.5 eV respectively. In addition, Fig. 7.1 exhibits some differences of the peapod spectrum from that of SWCNTs. They are evoked by the contributions of the C_{60}-derived molecular orbitals. Peaks according to the six highest occupied molecular orbitals (HOMOs) of C_{60} can be identified in the figure. The h_u-derived band (HOMO) and the h_g+g_g-derived band (HOMO -1,2) can be found at binding energies of 2.3 eV and 3.6 eV respectively while the HOMO-3 and HOMO-4 are located at 5.5 eV and 6.1 eV binding energy. In Fig. 7.1, these

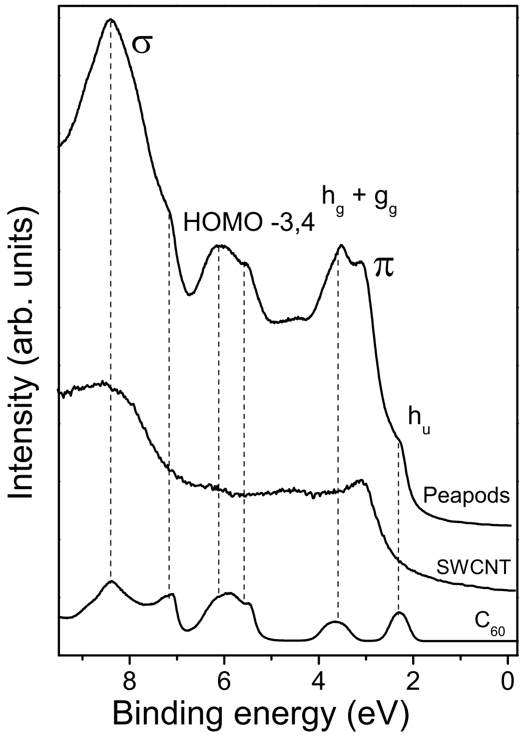

Figure 7.1: Comparison of the UPS Valence band spectra of C_{60} peapods, SWCNTs and C_{60}. The dashed vertical lines denote the correspondence of features in the peapod spectrum with the molecular orbitals of C_{60}.

features which are assigned to the C_{60} filling, are linked to the corresponding peaks in the spectrum of solid C_{60} by vertical lines. It becomes clear that every additional peak in the peapod spectrum finds its equivalent at the same binding energy in the C_{60} spectrum. The C_{60} peapod response is thus assembled from contributions from the SWCNT host and the C_{60} filling, each at the same binding energies as in the individual compounds.

Next, a detailed analysis of the region close to the Fermi level is carried out. The spectrum for the region with binding energies up to 1.7 eV is depicted in Fig. 7.2. Considering that all contributions from the C_{60} filling over the whole valence band region are found at the same binding energy as in pure C_{60}, no contribution from its molecular orbitals is expected in this energy range. And indeed, the spectrum very much resembles that of pristine SWCNTs (compare Fig. 5.4). Similar to SWCNTs, peaks in the photoemission response which originate from the two first van Hove singularities (vHs) of the semiconducting tubes (S_1, S_2) and the first vHs of the metallic tubes (M_1) can be observed. They can be found at binding energies of 0.46 eV (S_1), 0.78 (S_2) and 1.04 eV (M_1). These values are in very good agreement with the vHs positions obtained from SWCNTs where the peaks were found at 0.45 eV, 0.75 eV and 1.0 eV respectively. Note that no notable increase in spectral weight at the Fermi level which could possibly ascribed to a contribution of C_{60} molecular orbitals can be observed in comparison to SWCNTs. This contradicts LDA calculations [72] which predict the t_{1u} band which is completely unoccupied in pure C_{60} to cross the Fermi level if C_{60} is encapsulated by a metallic SWCNTs.

From the valence band photoemission results it can thus be concluded that the interaction between the electronic states of the peapod constituents is very weak. This was also concluded from EELS measurements [94]. Previous photoemission measurements [56] yielded similar values leading to the same conclusion that the respective electronic struc-

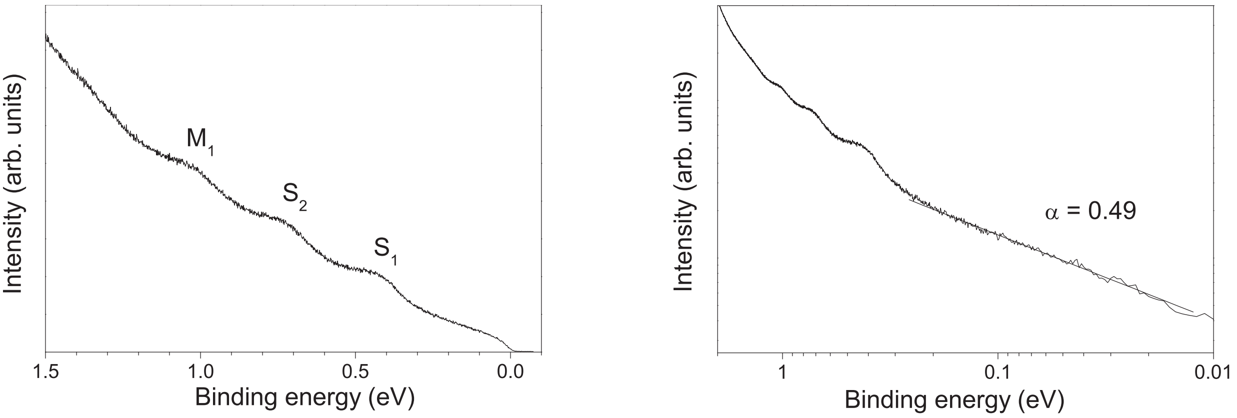

Figure 7.2: Valence band spectrum of C_{60} peapods near the chemical potential. **Right panel:** VHs region. **Left panel:** Double-logarithmic representation. The value for α is obtained from the linear fit (black line).

tures of the SWCNT host and the C_{60} guest remains mainly unperturbed by each other. Below, it will be discussed if the one-dimensional character of the electronic structure of the SWCNT host, i.e. the TLL behavior, is also retained and how it could be influenced by the C_{60} filling.

Tomonaga-Luttinger liquid behavior

In SWCNTs, the electrons in metallic tubes form a Tomonaga-Luttinger liquid which is expressed amongst others in a power law renormalization of the electronic density of states near the Fermi level. Above it was shown that the electronic structures of the peapod constituents are largely unaffected by each other. Therefore, it is also expected that the one-dimensional electronic structure of the SWCNT shell is conserved and that peapods with a metallic SWCNTs encapsulating the C_{60} molecules can also be regarded as Luttinger liquids. In the case of SWCNTs the TLL behavior was demonstrated by a power law behavior of both the electronic density of states and the temperature dependence of the conductance. Similar power law exponents α (0.46 and 0.48 respectively) were obtained [55]. In order to get the power law exponent for the C_{60} peapods, a linear fit of the photoemission response on double-logarithmic scale in the binding energy region from 0.02 up to 0.25 eV was carried out. The result is shown in the right panel of Fig. 7.2. The resulting value of α=0.49 is slightly increased compared to SWCNTs but still comparable enough to conclude that the behavior observed is similar to that of SWCNTs.

Based on the work by Okada *et al.* [72] discussed above, Que calculated the TLL renormalization for the case of C_{60} peapods [157]. The power law scaling factor α depends on the Luttinger parameter g as

$$\alpha = \frac{g^{-1} + g - 2}{8} \ . \tag{7.1}$$

A SWCNT power scaling factor $\alpha = 0.43$ corresponds to $g = 0.18$. The LDA band structure calculation of C_{60} encapsulated in metallic SWCNTs revealed two additional bands – the C_{60} t_{1u} bands – crossing the Fermi level. Under this assumption Que calculated the Luttinger parameter g_p for peapods as

$$\frac{1}{g_p^2} = \frac{2}{g_t^2} - 1 \, , \tag{7.2}$$

where g_t is the Luttinger parameter for SWCNTs. Based on the values derived for SWCNTs, the resulting Luttinger parameter for peapods is $g_p = 0.13$, yielding a peapod power law scaling factor $\alpha_p = 0.73$. This significant deviation from the value obtained from SWCNTs – caused by assumption that C_{60} derived bands cross the Fermi level – is not observed. Together with the fact that the spectral weight at the Fermi level is basically unchanged from that of SWCNTs, this leads to the conclusion that this assumption is most probably not true.

C_{60} peapod conduction band properties

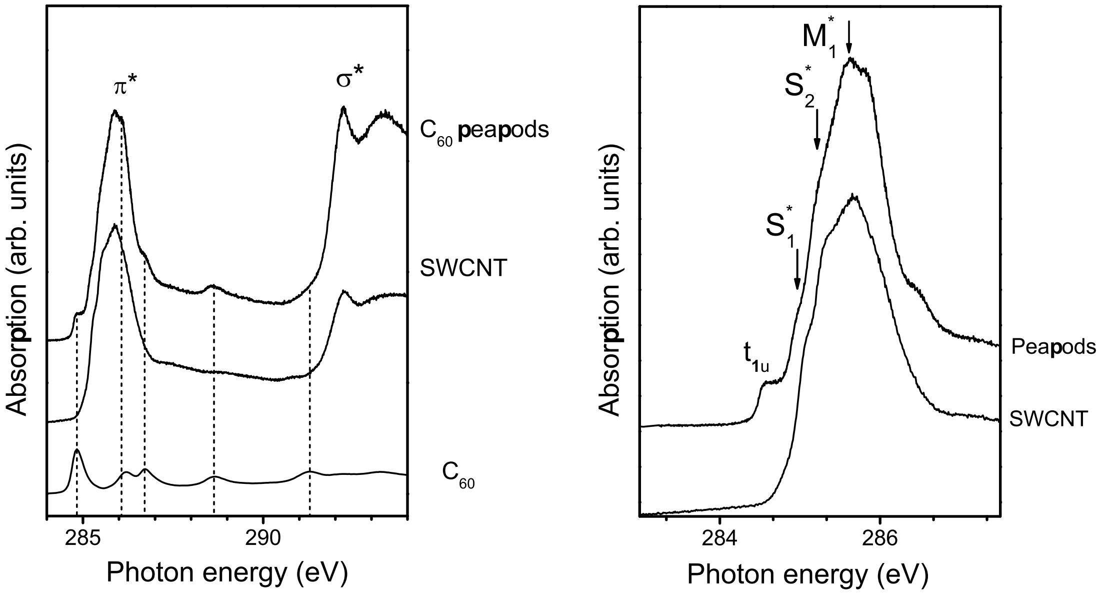

Figure 7.3: X-ray absorption spectra of C_{60} peapods and SWCNTs. **Left panel:** Comparison of the spectra from C_{60} peapods, SWCNTs, the subtraction of the SWCNTs from C_{60} peapods and solid C_{60} (from top to bottom) in the range between the SWCNT $\pi^\star$ and $\sigma^\star$ bands. The vertical dashed lines denote the features which are attributed to the excitation into the unoccupied molecular orbitals of C_{60}. **Right panel:** More detailed representation of the $\pi^\star$ region. The fine structure from the vHs of the SWCNTs is marked with the arrows.

Finally, the conduction band properties of the C_{60} peapods as they are obtained by x-ray absorption spectroscopy are discussed. The partial yield measurements were performed at the BESSY UE52-PGM beamline under the same experimental conditions as those presented in section 5.4. The left panel of Fig. 7.3 depicts the conduction band range of C_{60} peapods in comparison to SWCNTs and C_{60}. The C_{60} spectrum was taken from a C_{60} film evaporated on the SWCNT sample before equilibration led to the formation of the peapods. The C_{60} film was thick enough that no response from the underlying SWCNTs could be detected.

The $\pi^\star$ and $\sigma^\star$ bands of the SWCNT shell are common to the two spectra of C_{60} peapods and SWCNTs, and can be found at respective excitation energies which are identical for SWCNTs and C_{60} peapods. In the C_{60} peapod spectrum some additional features can be identified, eg. at both ends and at top of the $\pi^\star$ peak as well as a peak roughly in the middle between the $\pi^\star$ and $\sigma^\star$ bands. They are marked with vertical dashed lines in the figure. These features are attributed to excitations into the unoccupied molecular orbitals of the C_{60} filling. The lowest curve in Fig. 7.3 shows the XAS spectrum of solid C_{60} which is in good agreement with previous XAS measurements [158,159]. As in the valence band spectrum of C_{60} peapods, every feature in the C_{60} peapod spectrum attributed to the C_{60} filling has a corresponding peak in the C_{60} spectrum. This correspondence is not only qualitative, but the peaks are also found at the same excitation energies as indicated by the vertical lines. Again, just as in the valence band, the conduction band investigations clearly demonstrate that the electronic structure of the hybrid compound consists of the nearly undisturbed contributions of the two constituents.

The right panel of Fig. 7.3 shows the $\pi^\star$ region of C_{60} peapods and SWCNTs. In SWCNTs, a fine structure originating from absorptions from the unoccupied vHs from both, metallic and semiconducting tubes was observed. This fine structure can equally be recognized in C_{60} peapods, although the peaks are somewhat less pronounced. They are again found at the same excitation energies as in unfilled SWCNTs, indicating that the C_{60} filling does not perturb the SWCNT electronic structure on this energy scale either. Three features from the C_{60} filling can be observed in this absorption energy region, one on the lower energy side of the $\pi^\star$ peak, one on the higher energy side and one near the top. These absorptions are assigned to the unoccupied t_{1u} orbital, the h_g orbital and the h_u orbital as indicated in the figure. It was discussed before that particularly the location of the t_{1u} derived band in C_{60} peapods is of importance for the following doping experiments. Due to the excitonic character of the XAS spectra, no assertion can be made concerning the exact location of the t_{1u} band with respect to the Fermi level. However, one important observation can be made: The absorption from the t_{1u} band is well below the absorption of the first unoccupied vHs of the semiconducting tubes, $S_1^\star$ in the pristine state. This contradicts calculations discussed above where the C_{60} bands in C_{60} peapods were shifted rigidly by approximately 1 eV into the conduction band – in order to account for STS results [83,88]. In summary, the XAS measurements reveal conduction band properties of the C_{60} peapods very similar to those of the individual compounds.

Summary: Pristine C_{60} peapods

In this section the valence and conduction band properties of pristine C_{60} peapods were discussed and compared with those of its individual compounds, SWCNTs and C_{60} fullerenes. In both valence and conduction bands, the basic features from the constituents of the C_{60} peapods– i.e. the occupied and unoccupied π and σ bands as well as molecular orbitals derived from C_{60}– are found at the same energies as in the individual compounds. In the same way, the fine structures in the valence and conduction band, originating from the vHs in the electronic density of states of SWCNTs, were reproduced for C_{60} peapods, again at the same binding/excitation energies as in the individual compounds. It can therefore be concluded, that in C_{60} peapods the electronic structure is basically a superposition of the respective electronic structures of the individual compounds, a measurable hybridization does not take place. In addition, a TLL behavior is observed for the C_{60} peapods with a similar power law scaling factor α to that in SWCNTs. This means that the one-dimensional character of the electrons in the metallic SWCNT hosts is unaffected by the C_{60} filling.

The stability of α upon filling with C_{60} together with the unchanged spectral weight at the Fermi level of C_{60} peapods compared to SWCNTs leads to the conclusion that the t_{1u} derived band does not cross the Fermi level, nor is it shifted far into the conduction band as revealed by the XAS measurements. From the fact that the both occupied and unoccupied molecular orbitals are located at the same binding energies or excitation energies as in pure C_{60}, it can instead be concluded that the t_{1u} derived band is located somewhere near the Fermi level, just like in solid C_{60}, as was also predicted by some calculations [85]. We thus expect the t_{1u} band approximately 0.2 eV above the Fermi level, i.e. well below the first unoccupied vHs of the semiconducting tubes. A doping-induced shift of the Fermi level into the conduction band should thus lead to results distinct from those obtained on SWCNTs due to the role of the t_{1u} derived band. In the following sections the doping experiments are carried out and analyzed, focussing especially on the role of the t_{1u} band.

7.2 Doping behavior of the C_{60} peapod valence band

In the following sections, the influence of potassium doping on the electronic band structure of C_{60} peapods will be investigated in a similar way to that of SWCNTs presented in the previous chapter. As in the case of SWCNTs, the doping level was obtained using C1s core level PES by measuring and comparing the response from C1s and K2p electrons. In the low doping regime where the K2p signal was too weak to be analyzed, the doping level was estimated by the shift of the M_1 vHs peak, using the relation between the shift and the charge transfer obtained for SWCNTs.

π band and molecular orbitals

Theoretical calculations for C_{60} encapsulated in both semiconducting and metallic nanotubes predict the lowest unoccupied molecular orbital, the t_{1u}-derived band, close to the chemical potential [85, 160, 161], leaving open the question where exactly this band is located with respect to the Fermi level. In the pristine state of the C_{60}-peapods, no spectral weight in the valence band can be assigned to this band. To further investigate this, first the already well-established doping dependence of the valence band spectrum of bulk C_{60} is discussed. The left hand side of Fig. 7.4 depicts the PES spectra of the C_{60} phases for binding energies up to 5.5 eV. Due to preferential sites of the doping atoms in the fcc lattice, so-called line phases appear in doped C_{60} [61, 162]. They are shown in the figure where the numbers correspond to the x in K_xC_{60}. It is well known that out of all possible phases, only the K_3C_{60} phase is metallic, its metallic nature can easily be identified in the figure. The h_u-derived and the h_g+g_g-derived band are observable in the pristine state. In the α-phase, the sample is doped such that the t_{1u} orbital is pinned to the chemical potential. This results in a shift of the h_u-derived band and the h_g+g_g-derived band to higher binding energies by approximately 0.2 eV. Assuming that at these low doping levels the electronic structure of the α-phase is not drastically changed from that of pristine peapods, the position of the t_{1u} orbital is hence estimated to be approximately 0.2 eV above the chemical potential in the pristine state, in good agreement with inverse photoemission results on C_{60} [77].

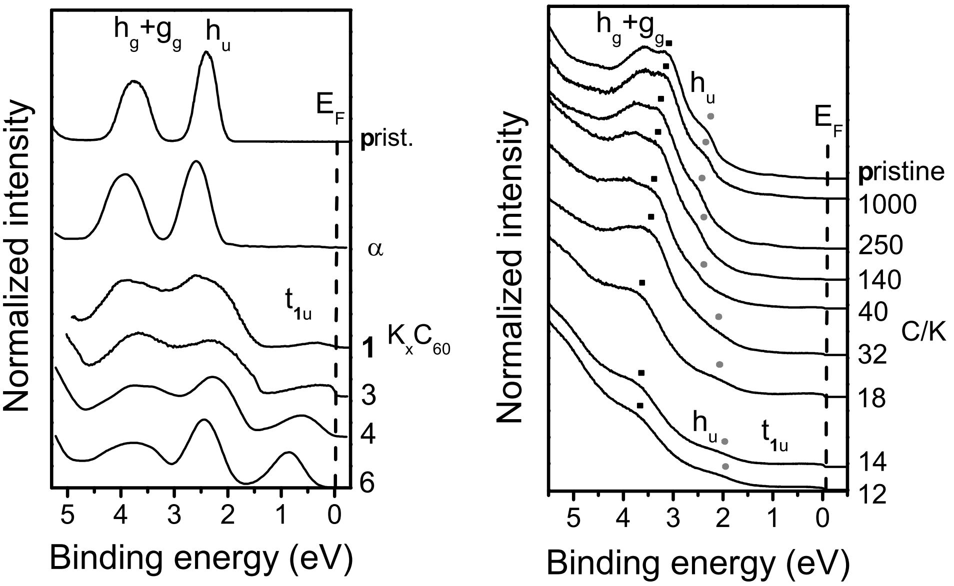

Figure 7.4: Doping dependence of the C_{60} peapod valence band (right panel) compared to solid C_{60} taken from Ref. [76] for the K_xC_{60} ($x = 0$, α, 3, 4, and 6) and from Ref. [163] in the case of the Rb_1C_{60} spectrum (left panel). The numbers in the figures correspond to the x in A_xC_{60} (A = K, Rb) in the case of solid C_{60} and to the C/K ratio in the case of C_{60} peapods.

The right hand side of Fig. 7.4 shows the doping dependence of the C_{60} peapods. One can distinguish between features derived from the SWCNTs - here the π-band - and those derived from C_{60}. In this region, these are the two highest occupied molecular orbitals. The position of the π-peak is marked in the figure by black squares. Upon increasing doping, this peak shifts continually to higher binding energies with a maximum shift of about 0.6 eV for a C/K ratio of 12. This observation is consistent with observations made on SWCNTs in the previous chapter and fits well in a rigid band shift model, where previously unoccupied states in the conduction band are filled, leading to a shift of the chemical potential.

The C_{60}-related features in the figure are the h_u-derived and the h_g+g_g-derived band. On increasing doping, both features start to broaden and smear out. At the two highest doping levels the h_g+g_g-derived band can no longer be identified individually as it merges with the π-band feature from the SWCNTs, while the h_u-derived band (marked in the figure with grey circles) can still be observed. Its position is first shifted gradually to higher binding energies up to 0.25 eV at a doping level of C/K = 40 but then moves back to lower binding energies. It finally settles at a binding energy of 2.1 eV, 0.2 eV lower than in the pristine state. This behavior shows that for the part of the electronic structure which is derived from the C_{60} peas, the simple rigid band shift model cannot be applied as easily as in the SWCNTs. But it is also not suitable to simply transfer the results obtained on solid C_{60} to C_{60} peapods, as there are important differences between solid C_{60} and C_{60} chains inside

SWCNTs. The main difference is that in C_{60} peapods, no line phases are expected due to the fact that the preferential sites do not exist in the chains. This was already observed by Raman measurements where the charge transfer to the C_{60} was monitored by the position of the $A_g(2)$ Raman mode of C_{60} [89,90]. This mode shifts to lower frequencies by about 6.5 cm^{-1} per electron transferred to the C_{60} ball and by 3 cm^{-1} per chemical bond. A continuous charge transfer to the C_{60} peas was observed with the highest doping level corresponding to a ${C_{60}}^{-6}$ single-bonded polymer.

In the case of C_{60}, a new band develops in the vicinity of the chemical potential already at low doping. This band is identified as the t_{1u}-derived band. Upon increasing doping, its spectral weight also increases and it is located at binding energies between the Fermi level (K_3C_{60}) and 0.82 eV (K_6C_{60}). This cannot be observed in the doped peapods. Assuming a homogenous distribution of the additional charge between the tubes and the C_{60}-molecules and an electronic structure of the two components as in the individual compounds (i.e. SWCNTs and solid C_{60}), the t_{1u}-derived band should appear at a C/K ratio of 60. However, no t_{1u} peak can be observed even at C/K = 32 and higher doping levels. Hence the absence of this band in the spectrum cannot be attributed to the competitive charge transfer, i.e. an inhomogeneous distribution of the additional charge between SWCNT hosts and C_{60} peas as it was seen in Raman measurements [89]. Thus the absence of the t_{1u}-derived band can only be explained by a strong broadening so that a clearly different behavior of the C_{60} molecular orbitals upon charge transfer compared to that of solid C_{60} is observed.

VHs fine structure

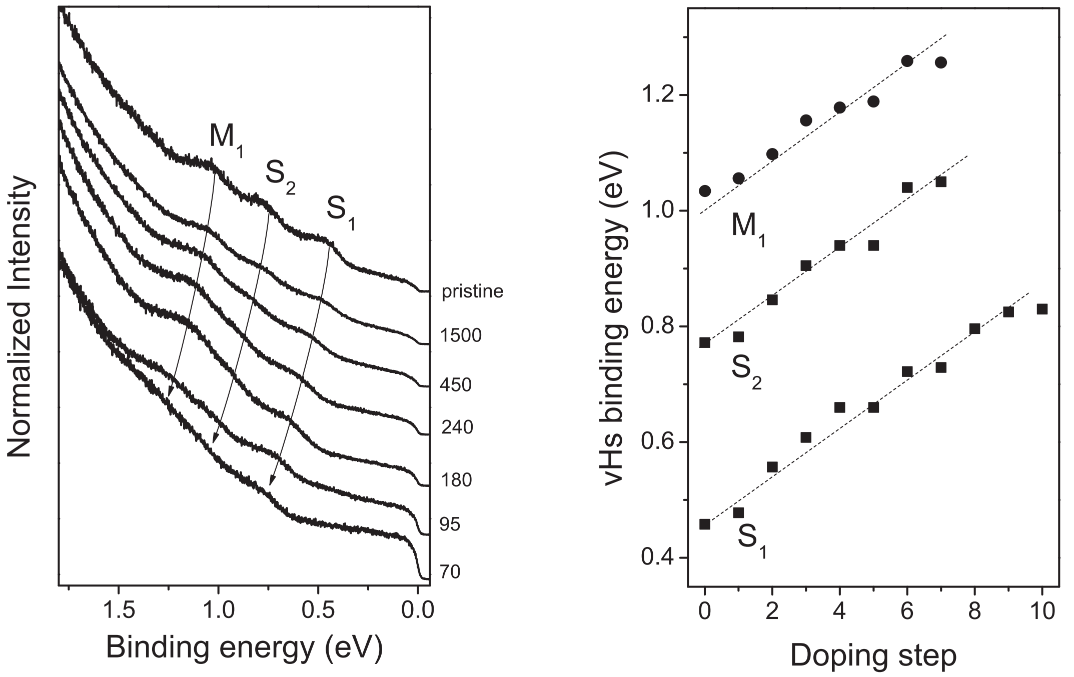

Figure 7.5: Left panel: Doping dependence of C_{60} peapods near the chemical potential. The shift of the vHs derived from the semiconducting (S_1, S_2) and metallic tubes (M_1) is indicated by the arrow (not all spectra shown). The numbers next to the graph indicate the C/K value as derived from the M_1 shift (see text). **Right panel:** Illustration of the vHs binding energies obtained from the valence band spectra.

The left panel of Fig. 7.5 depicts the photoemission response of C_{60} peapods in the case of lower doping levels (up to C/K = 70). It can clearly be seen that with increasing charge transfer, the van-Hove singularities are shifted to higher binding energies. This shift is indicated in the figure by the arrows. The shift of the vHs is caused by a shift of the chemical potential due to the gradual filling of states in the conduction band of the metallic nanotubes within the SWCNT bundles. The right panel of Fig. 7.5 summarizes the peak positions of the first two vHs from the semiconducting tubes, S_1 and S_2 as well as the first vHs from the metallic tubes, M_1. In contrast to SWCNTs, where the M_1 peak shifts significantly less at the first few doping steps (see Fig. 6.5), the peak position evolve nearly parallel.

Interestingly, no clear sign of the C_{60} t_{1u}-derived band can be observed in the spectra at these doping levels. In the case of similar behavior to the weakly doped K_1C_{60}-phase, it would be expected at binding energies around 1.0 eV and indeed an increase in spectral weight is observed in this region, especially at doping levels between C/K = 1000 and C/K = 250. But it cannot be assigned to the t_{1u}-derived band, as exactly the same behavior can be observed in the doping dependence of SWCNTs as shown in the previous chapter. At doping levels above C/K = 250, the spectral weight at the Fermi level increases progressively. This increase cannot be explained with a continued filling of bands of the metallic SWCNTs because these bands have a constant density of states in this region. Nor can a filling of states in the conduction band of the semiconducting tubes serve as an explanation, because the shift of the first van Hove singularity of these tubes is not yet high enough to allow such a conclusion. Therefore it must be attributed to the beginning filling of bands originating from the C_{60} molecular orbitals. The only reasonable candidate is the t_{1u}-derived molecular orbital, although the charge transfer is still far from high enough for to create a phase similar to the metallic phase in solid C_{60}. This would again mark a clearly distinct behavior of the C_{60} chains inside SWCNTs from that of bulk C_{60}.

7.3 Nature of the C_{60} peapod metallic ground state upon intercalation

Valence band photoemission of pristine C_{60} peapods revealed a power law scaling of the spectral weight near the Fermi level which was attributed to a Tomonaga-Luttinger liquid behavior. The scaling factor α was found to be comparable to that obtained on SWCNTs. It was already mentioned that filling with C_{60} molecules should have a certain influence on the doping behavior. In particular, the role of the lowest unoccupied molecular orbital, the t_{1u}-derived band, has to be considered. In order to further investigate the TLL-behavior of C_{60} peapods, the intercalation series is analyzed in analogy to that on SWCNTs in the previous chapter.

In SWCNTs, the renormalization of the spectral weight was demonstrated on a double-logarithmic scale. Here, a linear behavior denotes a power law scaling of the photoemission response. A linear fit on the double-logarithmic representation of the photoemission response in the vicinity of the chemical potential yields the power law exponent α within an experimental error of ± 0.024. In SWCNTs, the fit was carried out in the binding energy region between 0.02 and 0.2 eV since neither limited resolution and thermal broadening nor features in the density of states interfere with the renormalization of an otherwise constant

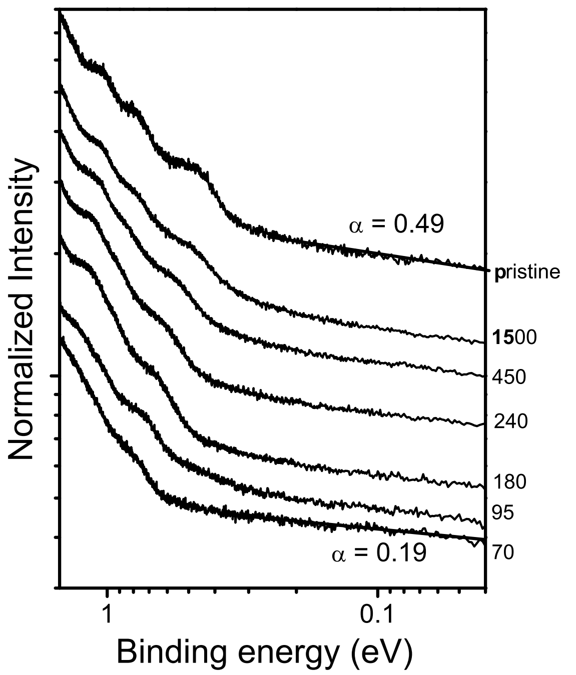

Figure 7.6: Double-logarithmic representation of the spectral response of C_{60} peapods near the Fermi level. For the pristine state and the highest doping level depicted the linear behavior is indicated by a line and the resulting power law scaling factor α is given.

density of states of the metallic tubes in this region. Furthermore, the energy scale of the TLL behavior was estimated to correspond approximately to this region. The same reasoning applies to C_{60} peapods. The highest occupied molecular orbital is situated at 2.3 eV binding energy, well above the Fermi level. The lowest unoccupied molecular orbital does not cross the Fermi level as was shown by the unchanged spectral weight and power law scaling factor in the pristine case.

Fig. 7.6 depicts the double-logarithmic representation of the C_{60} peapod response near the Fermi level at low and medium doping steps. It clearly shows that the power law behavior is retained upon doping and an evaluation of α is justified in the case of the depicted doping steps. Tab. 7.1 summarizes the resulting values together with the dopant concentration C/K and the shift of the first vHs, of the semiconducting tubes, ΔS_1, which is a measure for the Fermi level shift. In order to analyze the TLL behavior upon doping in more detail, Fig. 7.7 depicts the resulting values of α versus the doping level in comparison to those values acquired from the doping of SWCNTs. In the case of SWCNTs the power law scaling factor stayed constant as long as only states of the metallic tubes were filled with doping electrons. Upon increasing charge transfer α rapidly dropped to zero. This drop was attributed to a subsequent filling of the conduction band of the semiconducting tubes, thus rendering them metallic. The overall doping behavior was divided into three regions corresponding to different rigid shifts in the band structure (see Fig. 6.8). In the first region, only states of the metallic tubes are filled, α stays constant. In the second region, states in the conduction band of the semiconducting tubes are filled, starting with those tubes with the biggest diameter leading to a continuous decrease of α. In the third region, all tubes in the SWCNT bundles are rendered metallic. A Fermi liquid behavior where $\alpha = 0$ is observed. It was concluded that a bundle of then only metallic tubes loses its one-dimensional electronic structure due to screening of the Coulomb interaction and/or enhanced hopping between the tubes and consequently a loss of the one-dimensional character.

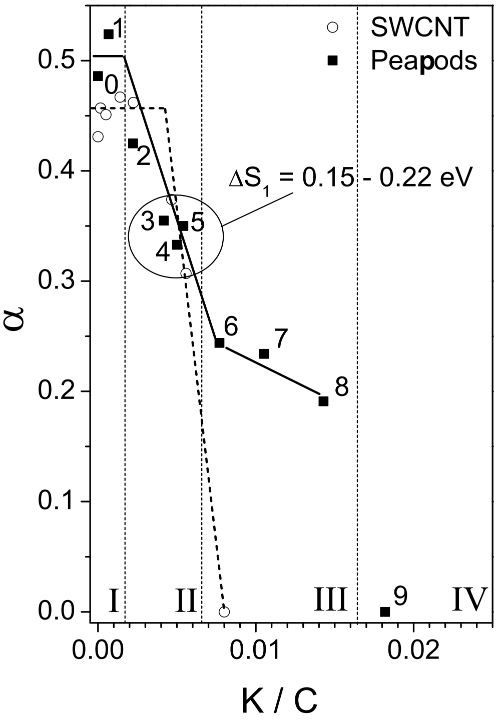

Figure 7.7: Change of the power law scaling factor α as a function of the doping level for C_{60} peapods (black squares) in comparison to previous results on single-wall carbon nanotubes (open circles). The numbers serve to identify the respective doping step in Tab. 7.1 and Fig. 7.8.

Also in C_{60} peapods, the power law scaling factor α stays constant and then starts to decrease. However, this decrease now starts already at C/K values of about 500 (K/C = 0.002). The corresponding shift of the first vHs of the semiconducting tubes is only 0.1 eV, so that the decrease can certainly not be regarded as a result of doping of the semiconducting tubes which is expected to start only at shifts of S_1 around 0.3 eV where the largest diameter tubes with the narrowest distance between vHs become metallic. Not only does the decrease of α start at smaller shifts of S_1, it also does not reach zero rapidly, as was the case for SWCNTs. Instead, it appears to slow down in the region where S_1 is shifted between 0.15 and 0.22 eV. Interestingly, no filling of conduction band states of the semiconducting tubes is expected in this region. A change in the power law renormalization can thus only be attributed to the role of the t_{1u}-derived band of the C_{60} filling. Upon increasing doping, at shifts of S_1 between 0.26 and 0.34 eV, α decreases even more until it can finally no longer be evaluated at $\Delta S_1 = 0.37$ eV where a Fermi edge is observed. A non-zero result of a linear fit of the double-logarithmic representation would have to be ascribed to the particular band shape as well as a redistribution of spectral weight due to electron-phonon coupling as explained further below. This is at the same time the ΔS_1 where in SWCNTs all tubes were driven metallic.

Since neither the filling of metallic states of the SWCNTs nor the filling of the conduction band of the semiconducting tubes can provide an explanation of either the decrease of α or the increase of spectral weight at the Fermi level, the role of the unoccupied molecular orbitals of the encapsulated C_{60} has to be considered. Interestingly, both occurrences happen exactly at the point where - in a rigid band shift model - one would expect to start filling

Step	ΔS_1 / eV	C/K	α
pristine	0	-	0.49
1	0.02	1500	0.52
2	0.10	450	0.43
3	0.15	240	0.36
4	0.20	200	0.33
5	0.22	185	0.35
6	0.26	130	0.24
7	0.27	95	0.23
8	0.34	70	0.19
9	0.37	55	≈ 0

Table 7.1: Overview of the values derived from the respective doping steps: Shift of the first vHs of the semiconducting tubes (ΔS_1), carbon to potassium ratio (C/K) and the power law scaling factor α derived from the linear fit on the double-logarithmic scale.

the t_{1u}-derived molecular orbital of C_{60}. It was expected to lie approximately 0.1 - 0.2 eV above the chemical potential with a band width of about 0.2 eV. The decrease of α starts at $\Delta S_1 = 0.15$ eV.

The situation is now interpreted in the picture of a rigid band shift. Although this model could not be applied to solid C_{60} due to the occurrence of line phases, its application is justified in this case because a) no line phases can be observed in C_{60} peapods and b) the doping levels used for this interpretation are still below a doping corresponding to the K_1C_{60} phase in solid C_{60}. Fig. 7.8 provides a simplified explanation of what is happening upon doping. A schematic view of the combined band structure of SWCNTs and C_{60} around the K point is shown on the left hand side and a sketch of the combined electronic density of states of both components is given on the right hand side. The diagonal grey lines correspond to the metallic bands which cross the Fermi level at the K point while the black parabola correspond to the bands of the semiconducting tubes with a direct semiconducting gap at the K point of about 0.6 eV. The horizontal line and the striped rectangle represent the C_{60}-related t_{1u}-derived band in the respective figures at a position of 0.2 eV above the Fermi level and an estimated width of 0.2 eV [1].

Similar to SWCNTs, the doping dependence is divided into regions, with the exception that in C_{60} peapods four of those region are identified. They are characterized by ΔS_1, i.e. the shift of the Fermi level, and indicated in the figure by differently shaded areas in the band structure representation and denoted with Roman numerals. The same regions are indicated and labelled in Fig. 7.7.

Region I correspond to shifts of S_1 between 0 and 0.10 eV (doping steps 0-2). In this region, α is unchanged within the experimental error and it can be interpreted in the same way as the corresponding region in SWCNT: Only states in the conduction band of metallic SWCNTs are filled, neither the C_{60} t_{1u}-derived band nor the conduction band of the semiconducting tubes is reached. The behavior typical for one-dimensional metals is retained. From this, it can also be concluded that the t_{1u}-derived band is not pinned at the Fermi level for very low doping levels as was expected elsewhere [85, 160, 161].

---

[1] The width of the C_{60} t_{1u}-derived band in peapods is estimated to be lower than in solid C_{60} due to a reduced nearest-neighbor coordination from 12 in fcc C_{60} to 2 for the C_{60} peas.

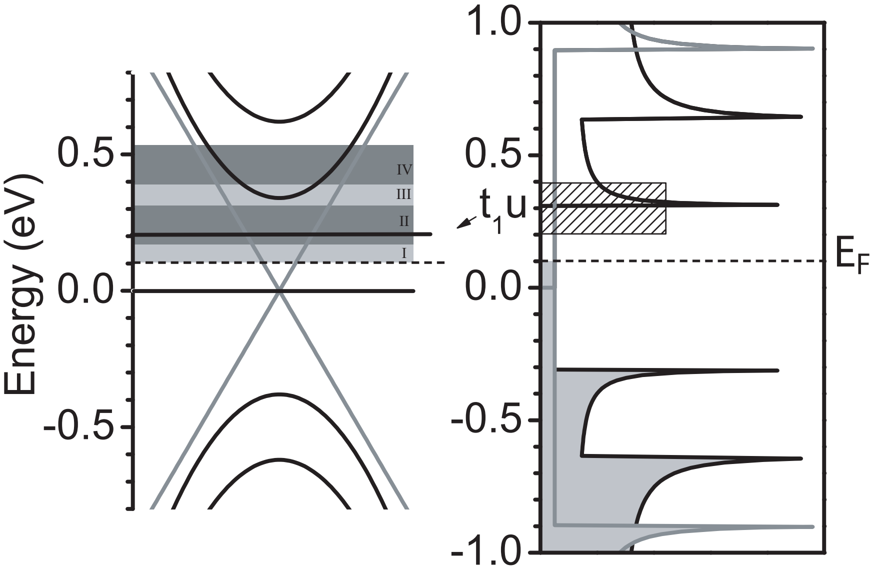

Figure 7.8: Schematic representation of the electronic band structure of C_{60} encapsulated in SWCNTs. In both figures the grey lines represent the metallic bands whereas the semiconducting bands are drawn in black. The horizontal lines in the left figure indicate the Fermi level shift of the different doping levels and are accordingly marked with the numbers which correspond to the values in Fig. 5. The grey area on the right figure indicates filled states in the pristine peapods while the striped rectangle represents the C_{60} t_{1u}-derived band which is not filled in pristine peapods. The latter is marked on the left figure with a horizontal line.

The situation changes with doping steps three to five, corresponding to S_1-shifts between 0.15 eV and 0.22 eV. The Fermi level is now shifted into the t_{1u}-derived band of C_{60} which results in both an increase of spectral weight at the Fermi level and a decrease of α to approximately $\alpha = 0.35$ as can be concluded from Figures 7.5 and 7.7 respectively. It seems that as long as the Fermi level is shifted into the t_{1u}-derived band of all peapods while the conduction band of the semiconducting tubes is still not reached, α stays constant.

Theoretical calculations for multi-wall carbon nanotubes (MWCNTs) predict a dependence of the power law scaling factor α on the number of one-dimensional conduction channels, i.e. the number of bands crossing the chemical potential [130]. With an increasing number of conduction channels a decrease of α is expected and the transport experiments on MWCNTs [156] discussed in section 6.3 could indeed be interpreted in this way. In this light it is tempting to interpret the behavior of α as an opening of additional conduction channels. For this interpretation, the C_{60} chains inside the SWCNTs must become metallic, form a one-dimensional conduction channel and at the same time may not interact with the SWCNT shell strongly enough to destroy overall one-dimensional behavior. This can happen inside both metallic and semiconducting tubes, leading to a superposition of two different systems and thus different power law scaling behavior. Another possible reason for the changed renormalization of the spectral weight at the Fermi level could be the influence of the actual band structure of the t_{1u}-derived band which - unlike metallic SWCNTs - does not have a constant density of states near the chemical potential and thus could have an influence on the evaluation of the power law scaling factor α by a linear fit in the double-logarithmic evaluation. On the other hand, this fit is carried out in the binding energy region between 0.02 eV and 0.2 eV and the width of the band is expected to be around 0.2

eV. This means that the fit region is approximately the same size as the band width and thus an effect on α should be weak.

Region III of the doping regime (doping steps 6-8) is characterized by an increasing drop of α at S_1 shifts between 0.26 and 0.34 eV. This is the same range of ΔS_1 where the rapid drop of α was observed in the case of SWCNTs. It was explained by a beginning filling of the conduction band semiconducting tubes, starting with the largest diameter tubes where the $M_1^\star$ vHs is closest to the Fermi level. Of course, the same interpretation can be applied to C_{60} peapods. However, as a function of the dopant concentration, the decrease appears to be somewhat slower. The reason for this is the fact that with the additional charge the C_{60} conduction band must be also filled.

At vHs shifts $\Delta S_1 \geq 0.37$ (Region IV), α can no longer be evaluated. The photoemission response now resembles a Fermi edge. At this point, the Fermi level is shifted well into the previously unoccupied states of the semiconducting tubes and for SWCNTs, a drop of α to zero was observed which is synonymous for a Fermi liquid behavior. In the case of C_{60} peapods, a clear evolution of a Fermi edge together with an even more increased spectral weight at the chemical potential can also be observed for the higher doping levels (see below). This Fermi edge is a clear indicator for the Fermi liquid behavior typical for three-dimensional metals and as such significantly different from the power law renormalization of the spectral weight which was observed for the pristine and lowly doped state.The conclusion drawn is now that – similar to SWCNTs – a transition from a TLL to a Fermi liquid can be observed, only this time through an intermediate state which is characterized by a decrease of the power law scaling factor α and an increase of spectral weight at the chemical potential due to the influence of t_{1u}-derived bands. One possible explanation for this behavior is the formation of additional conduction channels by one-dimensional metallic chains of C_{60} inside the tubes. However, an influence of the actual shape of the t_{1u}-derived band cannot be excluded.

7.4 High doping

Now the high doping levels which are depicted in Fig. 7.9 are analyzed. The figure shows the photoemission spectra of the region near the Fermi level for the doping levels between C/K = 150 and C/K = 12, which is also the highest doping level achieved in these studies. At the three lowest doping levels depicted (C/K = 150, 75 and 50), the vHs, especially S_1, and their shift to higher binding energies upon intercalation can still be observed. For even further doping, the vHs vanish in the same way as already observed in K-intercalated SWCNTs. Here, the same explanation as in SWCNTs applies where vanishing was ascribed to effects such as an increasing number of scattering centers (K^+ counter ions) and an increasing intertube interaction within the peapod bundles in the intercalation compound. Also the general shape of the spectra at these high doping levels corresponds to those of SWCNTs and GICs. The Fermi level shift can be extracted from the shift of the π-band which lies in the pristine peapods at a binding energy of 3 eV and amounts in our case to 0.8 eV. This shift is lower than in the cases of SWCNTs and GICs, where for similar doping levels values of 1.0 eV and 1.25 eV were observed. This can be explained with a higher number of states in the conduction band of the peapods. With the same number of electrons transferred to the peapods the t_{1u}-derived band of the C_{60} must also be filled, resulting in a lower overall shift of the chemical potential. Nonetheless, the shift of the chemical potential is

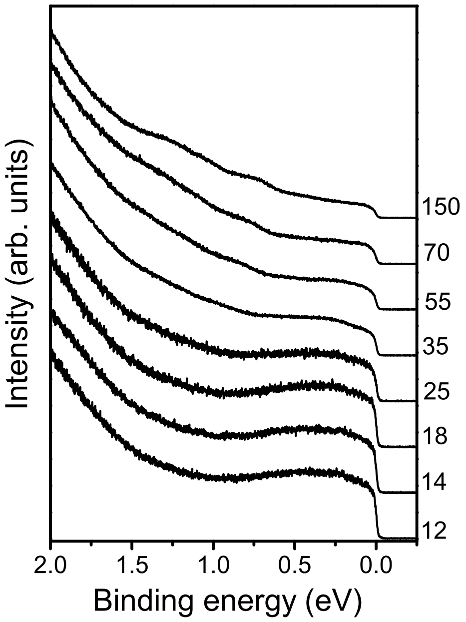

Figure 7.9: Doping dependence of the valence band spectra of C_{60} peapods for higher doping levels. The numbers next to the graph indicate the C/K ratio of the respective doping level. Inset: Comparison of the valence band spectra of pristine (black line, upscaled for clarity) and highly doped (grey line, C/K = 14) C_{60} peapods.

still high enough that the formerly unoccupied S_1^*, S_2^* and M_1^* vHs are also filled. But interestingly, no corresponding peaks can be observed. A redistribution of spectral weight at around 170 meV binding energy appears at the doping level C/K = 35, but it cannot be assigned to previously unoccupied vHs, as it does not shift with increasing doping as would be the case for the vHs. Therefore, it is interpreted in the same way as the similar feature which appeared in highly doped SWCNTs where this satellite in the photoemission response appears at the same binding energy which is also very close to the frequency of the G-line of doped SWCNTs [89]. The feature can be interpreted as a redistribution of spectral weight due to electron-phonon coupling which is also supported by the close analogy of the line shape to the low energy photoemission spectra of the metallic C_{60} intercalation compound K_3C_{60} [137]. This spectrum is dominated by strong satellites due to coupling to phonons and to the charge carrier plasmon which is an effect which would also explain the absence of peaks from the previously unoccupied S_1^*, S_2^* and M_1^* vHs.

7.5 Summary

In this chapter the electronic structure of C_{60} peapods and its evolution upon potassium doping was investigated. In the pristine state the electronic structure of the hybrid compound has been interpreted as a superposition of the respective electronic structures of the individual compounds, i.e. the π and σ bands from the SWCNT host and the molecular orbitals from the C_{60} filling. This is true for the overall behavior as well as for the fine structure. At the same time, the metallic tubes retain their one-dimensional character as indicated by the TLL power law scaling near the chemical potential with a power law scaling factor similar to that obtained from metallic SWCNTs. It was shown that the t_{1u}-derived band of the C_{60} is located above the Fermi level.

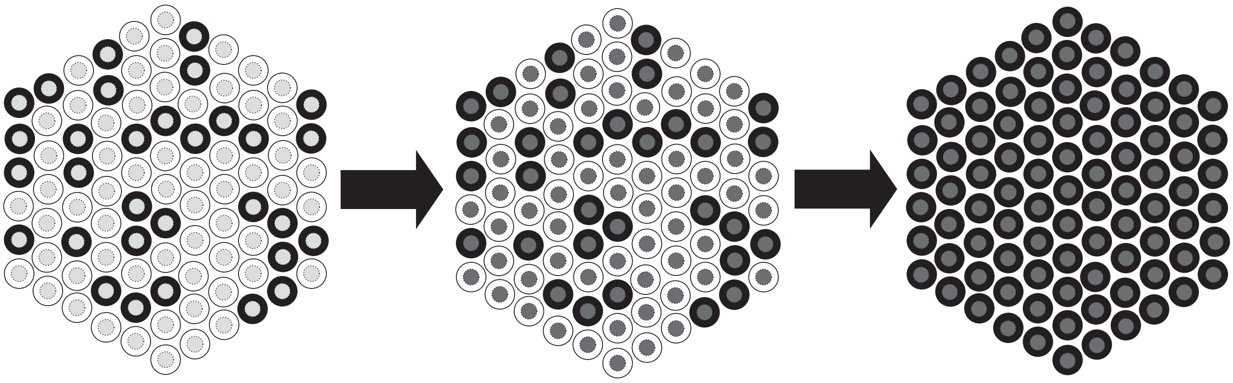

Figure 7.10: Schematic view of an undoped C_{60} peapod bundle (left) consisting of 1/3rd semiconducting (open circles) and 2/3rd metallic (black circles) tubes filled with semiconducting C_{60} molecules (light grey dashed circles inside). During doping this bundle is transformed to a bundle consisting of SWCNT hosts of the same type as in the pristine state but filled with metallic chains of C_{60}, as indicated by the dark grey inner circles. Upon further doping also the previously semiconducting host tubes become metallic. The whole bundle now consists of metallic tubes filled with metallic chains of C_{60}.

Upon doping, the spectral features assigned to the SWCNT host shift continually to higher binding energies as expected in a rigid band shift model which was already successfully applied to SWCNTs. However, this model cannot be used equally for the C_{60}-derived bands. In particular, the highest occupied molecular orbital, the h_u-derived band, exhibits non-continuous behavior, especially at high doping. On the other hand, the development of these features does not also correspond to the doping behavior of solid C_{60}, where line phases were observed.

Nevertheless, at low doping the evolution of the TLL power scaling factor α can be interpreted well in the rigid band shift model. All in all, in this picture a complicated situation emerges which in Fig. 7.10. In the pristine state and at the very first doping steps the peapod bundles consist of a mixture of semiconducting and metallic nanotubes which are filled with semiconducting C_{60} molecules. Upon doping, the conduction band which is estimated to be located close to the chemical potential is filled first. If the doping-induced shift of the Fermi level amounts to ≈ 0.15 eV, a decrease of α is observed and explained by the influence of the t_{1u} orbital of the C_{60} filling. New conduction channels formed by one-dimensional metallic C_{60} chains inside the SWCNTs as they were observed before in Raman spectroscopy [89] would explain this behavior. Upon even further doping all host tubes are rendered metallic so that the sample consists of only metallic tubes filled with metallic C_{60} chains. Although the structure of the tubes and the C_{60} chains is still one-dimensional, a Fermi edge, characteristic for three-dimensional metals, is observed for all those higher doping steps. Similar to SWCNTs this can be explained by a strong screening of the Coulomb interaction between charge carriers in neighboring nanotubes and/or by the fact that in a bundle of metallic tubes only, the hopping matrix element between the tubes is strongly enhanced, thus yielding a more three-dimensional electronic structure.

8 Conclusion

The aim of this thesis was to study the metallic ground state of one-dimensional and three-dimensional systems and a charge transfer-induced transition between these two systems. One- and three-dimensional systems exhibit distinctly different properties, expressed amongst others in different scaling behaviors of the density of states at the Fermi level. Single-wall carbon nanotubes are a paradigm of one-dimensional systems and together with the fact that photoemission is an ideal tool for probing the density of states, this motivates an investigation of SWCNTs with this spectroscopic method. In a first step it was shown by the power law scaling of the photoemission response, that single-wall carbon nanotubes indeed exhibit the electronic properties expected for one-dimensional systems

The main part of this thesis was devoted to the investigation of the metallic ground state of SWCNTs upon functionalization. First, the behavior of the realistic three-dimensional structure of SWCNT bundles upon chemical doping was probed. The overall modification of the electronic band structure can be explained well by a rigid band shift model. The one-dimensional character of the metallic tubes in the bundle is retained at low doping, but when the semiconducting tubes are also rendered metallic by the charge transfer, the overall appearance changes. A Fermi edge emerges out of the power law renormalization of the spectral weight, signifying a transition to a three-dimensional metallic behavior, concomitant with the observed increasing asymmetry of the C1s response at these doping levels. A crossover from a Tomonaga-Luttinger liquid to a Fermi liquid is observed.

The filling of SWCNTs with C_{60} molecules raised questions concerning the role of additional bands in the one-dimensional system. In the pristine state, the states of the C_{60} filling were found to have no influence on the metallic ground state. Upon doping however, the modified band structure leads to a qualitative change in the crossover from a Tomonaga-Luttinger liquid to a Fermi liquid. The evolution of the power law scaling at intermediate doping can be interpreted as an opening of an additional conduction channel of one-dimensional metallic chains of C_{60} inside the tubes in good agreement with transport experiments.

Bibliography

[1] Kroto, H. W., Heath, J. R., O'Brien, S. C., Curl, R. F. & Smalley, R. E. C_{60}: Buckminsterfullerene. *Nature* **318**, 162–163 (1985).

[2] Smalley, R. E. Discovering the fullerenes. *Review of Modern Physics* **69**, 723–730 (1997).

[3] Iijima, S. Helical Microtubules of Graphitic Carbon. *Nature* **354**, 56–58 (1991).

[4] Iijima, S. & Ichihashi, T. Single-shell carbon nanotubes of 1-nm diameter. *Nature* **363**, 603–605 (1993).

[5] Bethune, D. S. *et al.* Cobalt-catalysed growth of carbon nanotubes with single-atomic-layer walls. *Nature* **363**, 605–607 (1993).

[6] Dresselhaus, M. S., Dresselhaus, G. & Eklund, P. *Science of Fullerenes and Carbon Nanotubes* (Academic, San Diego, 1996).

[7] Mintmire, J. W., Dunlap, B. I. & White, C. T. Are fullerene tubules metallic? *Physical Review Letters* **68**, 631–634 (1992).

[8] Hamada, N., Sawada, S.-i. & Oshiyama, A. New one-dimensional conductors: Graphitic microtubules. *Physical Review Letters* **68**, 1579–1581 (1992).

[9] Tans, S. J. *et al.* Individual single-wall carbon nanotubes as quantum wires. *Nature* **386**, 474–477 (1997).

[10] Nygard, J., Cobden, D. H., Bockrath, M., McEuen, P. L. & Lindelof, P. E. Electrical transport measurements on single-walled carbon nanotubes. *Applied Physics A-Materials Science & Processing* **69**, 297–304 (1999).

[11] Dürkop, T., Brintlinger, T. & Fuhrer, M. S. Nanotubes are high mobility semiconductors. *Structural And Electronic Properties Of Molecular Nanostructures* **633**, 242–246 (2002).

[12] Tans, S. J., Verschueren, A. R. M. & Dekker, C. Room-temperature transistor based on a single carbon nanotube. *Nature* **393**, 49–52 (1998).

[13] Bachtold, A., Hadley, P., Nakanishi, T. & Dekker, C. Logic Circuits with Carbon Nanotube Transistors. *Science* **294**, 1317–1320 (2001).

[14] Misewich, J. A. *et al.* Electrically induced optical emission from a carbon nanotube FET. *Science* **300**, 783–786 (2003).

[15] Dresselhaus, M. S. & Dai, H. Carbon nanotubes: Continued innovations and challenges. *MRS Bulletin* **29**, 237–239 (2004).

[16] Dresselhaus, M. S. *et al.* Science and applications of single-nanotube Raman spectroscopy. *Journal of Nanoscience and Nanotechnology* **3**, 19–37 (2003).

[17] Jorio, A. *et al.* Carbon nanotube photophysics. *MRS Bulletin* **29**, 276–280 (2004).

[18] Datta, S. *Electronic Transport in Mesoscopic Systems* (Cambridge University Press, Cambridge, 1995).

[19] Mann, D., Javey, A., Kong, J., Wang, Q. & Dai, H. J. Ballistic transport in metallic nanotubes with reliable Pd ohmic contacts. *Nano Letters* **3**, 1541–1544 (2003).

[20] Bockrath, M. *et al.* Single-electron transport in ropes of carbon nanotubes. *Science* **275**, 1922–1925 (1997).

[21] Wang, F., Dukovic, G., Brus, L. E. & Heinz, T. F. The Optical Resonances in Carbon Nanotubes Arise from Excitons. *Science* **308**, 838–841 (2005).

[22] Maultzsch, J. *et al.* Exciton binding energies in carbon nanotubes from two-photon photoluminescence. *Physical Review B* **72**, 241402 (2005).

[23] Bockrath, M. *et al.* Luttinger-liquid behaviour in carbon nanotubes. *Nature* **397**, 598–601 (1999).

[24] Bachtold, A. *et al.* Suppression of tunneling into multiwall carbon nanotubes. *Physical Review Letters* **87** (2001).

[25] Gao, B., Komnik, A., Egger, R., Glattli, D. C. & Bachtold, A. Evidence for Luttinger-Liquid Behavior in Crossed Metallic Single-Wall Nanotubes. *Physical Review Letters* **92**, 216804 (2004).

[26] Yao, Z., Postma, H. W. C., Balents, L. & Dekker, C. Carbon nanotube intramolecular junctions. *Nature* **402**, 273–276 (1999).

[27] Saito, R., Dresselhaus, G. & Dresselhaus, M. *Physical Properties of Carbon Nanotubes* (Imperial College Press, London, 1998).

[28] Pfeiffer, R. *Dispersion of Raman Lines in Carbon Nanophases.* Ph.D. thesis, University of Vienna (1994).

[29] Saito, R. & Kataura, H. *Carbon nanotubes* (Springer topics in applied physics, New York, 2001).

[30] Reich, S., Maultzsch, J., Thomsen, C. & Ordejon, P. Tight-binding description of graphene. *Physical Review B* **66** (2002).

[31] Popov, V. N. Curvature effects on the structural, electronic and optical properties of isolated single-walled carbon nanotubes within a symmetry-adapted non-orthogonal tight-binding model. *New Journal Of Physics* **6** (2004).

[32] Saito, R., Dresselhaus, G. & Dresselhaus, M. S. Trigonal warping effect of carbon nanotubes. *Physical Review B* **61**, 2981–2990 (2000).

[33] Kataura, H. *et al.* Optical properties of single-wall carbon nanotubes. *Synthetic Metals* **103**, 2555–2558 (1999).

[34] Bachilo, S. M. *et al.* Structure-Assigned Optical Spectra of Single-Walled Carbon Nanotubes. *Science* **298**, 2361–2366 (2002).

[35] Samsonidze, G. G. *et al.* Family behavior of the optical transition energies in single-wall carbon nanotubes of smaller diameters. *Applied Physics Letters* **85**, 5703–5705 (2004).

[36] Guo, T., Nikolaev, P., Thess, A., Colbert, D. T. & Smalley, R. E. Catalytic Growth of Single-walled Nanotubes by Laser Vaporization. *Chemical Physics Letters* **243**, 49–54 (1995).

[37] Yudasaka, M. *et al.* Mechanism of the effect of NiCo, Ni and Co catalysts on the yield of single-wall carbon nanotubes formed by pulsed Nd : YAG laser ablation. *Journal of Physical Chemistry B* **103**, 6224–6229 (1999).

[38] Eklund, P. C. *et al.* Large-scale production of single-walled carbon nanotubes using ultrafast pulses from a free electron laser. *Nano Letters* **2**, 561–566 (2002).

[39] Maser, W. K. *et al.* Production of high-density single-walled nanotube material by a simple laser-ablation method. *Chemical Physics Letters* **292**, 587–593 (1998).

[40] Bolshakov, A. P. *et al.* A novel CW laser-powder method of carbon single-wall nanotubes production. *Diamond and Related Materials* **11**, 927–930 (2002).

[41] Thess, A. *et al.* Crystalline ropes of metallic carbon nanotubes. *Science* **273**, 483–487 (1996).

[42] Ebbesen, T. W. & Ajayan, P. M. Large-scale synthesis of carbon nanotubes. *Nature* **358**, 220–222 (1992).

[43] Ren, Z. F. *et al.* Growth of a single freestanding multiwall carbon nanotube on each nanonickel dot. *Applied Physics Letters* **75**, 1086–1088 (1999).

[44] Duesberg, G. S. *et al.* Growth of isolated carbon nanotubes with lithographically defined diameter and location. *Nano Letters* **3**, 257–259 (2003).

[45] Ren, Z. F. *et al.* Synthesis of large arrays of well-aligned carbon nanotubes on glass. *Science* **282**, 1105–1107 (1998).

[46] Li, W. Z. *et al.* Large-scale synthesis of aligned carbon nanotubes. *Science* **274**, 1701–1703 (1996).

[47] Terrones, M. *et al.* Controlled production of aligned-nanotube bundles. *Nature* **388**, 52–55 (1997).

[48] Murakami, Y. *et al.* Growth of vertically aligned single-walled carbon nanotube films on quartz substrates and their optical anisotropy. *Chemical Physics Letters* **385**, 298–303 (2004).

[49] Hata, K. *et al.* Water-assisted highly efficient synthesis of impurity-free single-waited carbon nanotubes. *Science* **306**, 1362–1364 (2004).

[50] Ogawa, T. & Takagahara, T. Optical absorption and Sommerfeld factors of one-dimensional semiconductors: An exact treatment of excitonic effects. *Physical Review B* **44**, 8138–8156 (1991).

[51] Ando, T. Excitons in carbon nanotubes. *Journal of the Physical Society of Japan* **66**, 1066–1073 (1997).

[52] Ma, Y.-Z. *et al.* Ultrafast carrier dynamics in single-walled carbon nanotubes probed by femtosecond spectroscopy. *The Journal of Chemical Physics* **120**, 3368–3373 (2004).

[53] Dukovic, G. *et al.* Structural dependence of excitonic optical transitions and band-gap energies in carbon nanotubes. *Nano Letters* **5**, 2314–2318 (2005).

[54] Capaz, R. B., Spataru, C. D., Ismail-Beigi, S. & Louie, S. G. Diameter and chirality dependence of exciton properties in carbon nanotubes. *Physical Review B* **74**, 121401 (2006).

[55] Ishii, H. *et al.* Direct observation of Tomonaga-Luttinger-liquid state in carbon nanotubes at low temperatures. *Nature* **426**, 540–544 (2003).

[56] Shiozawa, H. *et al.* Filling factor and electronic structure of Dy3N@C-80 filled single-wall carbon nanotubes studied by photoemission spectroscopy. *Physical Review B* **73**, 205411 (2006).

[57] Wildoer, J. W. G., Venema, L. C., Rinzler, A. G., Smalley, R. E. & Dekker, C. Electronic structure of atomically resolved carbon nanotubes. *Nature* **391**, 59–62 (1998).

[58] Takenobu, T. *et al.* Stable and controlled amphoteric doping by encapsulation of organic molecules inside carbon nanotubes. *Nature Materials* **2**, 683–688 (2003).

[59] Smith, B. W., Monthioux, M. & Luzzi, D. E. Encapsulated C_{60} in carbon nanotubes. *Nature* **396**, 323–324 (1998).

[60] Dresselhaus, M. S. & Dresselhaus, G. Intercalation Compounds of Graphite. *Advances in Physics* **30**, 139–326 (1981).

[61] Gunnarsson, O. *Alkali-Doped Fullerides, Narrow-Band Solids with Unusual Properties* (World Scientific Publishing Co. Pte. Ltd, 2004).

[62] Liu, X. *Electronic structure and excitation states of pristine and intercalated single-wall carbon nanotubes.* Ph.D. thesis, Technische Universität Dresden (2005).

[63] Liu, X., Pichler, T., Knupfer, M. & Fink, J. Electronic properties of barium-intercalated single-wall carbon nanotubes. *Physical Review B* **70**, 245435 (2004).

[64] Guan, L. H., Suenaga, K., Shi, Z. J., Gu, Z. N. & Iijima, S. Direct Imaging Of The Alkali Metal Site In K-Doped Fullerene Peapods. *Physical Review Letters* **94**, 045502 (2005).

[65] Miyake, T. & Saito, S. Electronic structure of potassium-doped carbon nanotubes. *Physical Review B* **65**, 165419 (2002).

[66] Souza Filho, A. G. *et al.* Resonance Raman scattering studies in Br_2-adsorbed double-wall carbon nanotubes. *Physical Review B* **73**, 235413 (2006).

[67] Rao, A. M., Eklund, P. C., Bandow, S., Thess, A. & Smalley, R. E. Evidence for charge transfer in doped carbon nanotube bundles from Raman scattering. *Nature* **388**, 257–259 (1997).

[68] Liu, X., Pichler, T., Knupfer, M. & Fink, J. Electronic and optical properties of alkali-metal-intercalated single-wall carbon nanotubes. *Physical Review B* **67**, 125403 (2003).

[69] Kratschmer, W., Lamb, L. D., Fostiropoulos, K. & Huffman, D. R. Solid C_{60}: A New Form Of Carbon. *Nature* **347**, 354–358 (1990).

[70] Kataura, H. *et al.* Optical properties of fullerene and non-fullerene peapods. *Applied Physics A-Materials Science & Processing* **74**, 349–354 (2002).

[71] Liu, X. *et al.* Filling factors, structural, and electronic properties Of C_{60} molecules in single-wall carbon nanotubes. *Physical Review B* **65**, 045419 (2002).

[72] Okada, S., Saito, S. & Oshiyama, A. Energetics and electronic structures of encapsulated C-60 in a carbon nanotube. *Physical Review Letters* **86**, 3835–3838 (2001).

[73] Liu, X., Pichler, T., Knupfer, M., Fink, J. & Kataura, H. Determination of the filling factor of C_{60} peapods by electron energy-loss spectroscopy in transmission. *Synthetic Metals* **135**, 715–716 (2003).

[74] Kataura, H. *et al.* High-yield fullerene encapsulation in single-wall carbon nanotubes. *Synthetic Metals* **121**, 1195–1196 (2001).

[75] Simon, F. *et al.* Low temperature fullerene encapsulation in single wall carbon nanotubes: synthesis of N@C_{60}@SWCNT. *Chemical Physics Letters* **383**, 362–367 (2004).

[76] Knupfer, M. Electronic properties of carbon nanostructures. *Surface Science Reports* **42**, 1–74 (2001).

[77] Takahashi, T. *et al.* Pseudo-Gap at the Fermi level in K_3C_{60} Observed by Photoemission and Inverse Photoemission. *Physical Review Letters* **68**, 1232–1235 (1992).

[78] Weaver, J. H. *et al.* Electronic structure of Solid C_{60} - Experiment and Theory. *Physical Review Letters* **66**, 1741–1744 (1991).

[79] Lof, R. W., van Veenendaal, M. A., Koopmans, B., Jonkman, H. T. & Sawatzky, G. A. Band gap, excitons, and Coulomb interaction in solid C_{60}. *Physical Review Letters* **68**, 3924–3927 (1992).

[80] Gensterblum, G. *et al.* Experimental Evidence For 400-MeV Valence-Band Dispersion In Solid C_{60}. *Physical Review B* **48**, 14756–14759 (1993).

[81] Saito, S. & Oshiyama, A. Cohesive Mechanism And Energy-Bands Of Solid C_{60}. *Physical Review Letters* **66**, 2637–2640 (1991).

[82] Weaver, J. H., Benning, P. J., Stepniak, F. & Poirier, D. M. K_xC_{60} Nonequilibrium Thin-Film Growth and Spectroscopy Results. *Journal Of Physics And Chemistry Of Solids* **53**, 1707–1711 (1992).

[83] Hornbaker, D. J. *et al.* Mapping the One-Dimensional Electronic States of Nanotube Peapod Structures. *Science* **295**, 828–831 (2002).

[84] Rochefort, A. Electronic and transport properties of carbon nanotube peapods. *Physical Review B* **67**, 115401 (2003).

[85] Dubay, O. & Kresse, G. Density functional calculations for C_{60} peapods. *Physical Review B* **70**, 165424 (2004).

[86] Otani, M., Okada, S. & A., O. Energetics and Electronic Structure of One-dimensional Fullerene Chains Encapsulated in Zigzag Nanotubes. *Physical Review B* **68**, 125424 (2003).

[87] Okada, S., Oshiyama, A. & Saito, S. Nearly free electron states in carbon nanotube bundles. *Physical Review B* **62**, 7634–7638 (2000).

[88] Kane, C. L. *et al.* Theory of scanning tunneling spectroscopy of fullerene peapods. *Physical Review B* **66**, 235423 (2002).

[89] Pichler, T., Kuzmany, H., Kataura, H. & Achiba, Y. Metallic polymers of C_{60} inside single-walled carbon nanotubes. *Physical Review Letters* **87**, 267401 (2001).

[90] Pichler, T., Kukovecz, A., Kuzmany, H., Kataura, H. & Achiba, Y. Quasicontinuous electron and hole doping of C_{60} peapods. *Physical Review B* **67**, 125416 (2003).

[91] Kuzmany, H. *Solid-state spectroscopy* (Springer Verlag, Berlin Heidelberg New York, 1998).

[92] Knupfer, M. *et al.* Electron energy-loss spectroscopy studies of single wall carbon nanotubes. *Carbon* **37**, 733–738 (1999).

[93] Pichler, T. Electron energy-loss studies of pristine and doped nanotubes. *New Diamond and Frontier Carbon Technology* **11**, 375–397 (2001).

[94] Pichler, T., Liu, X., Knupfer, M. & Fink, J. Electronic properties of intercalated single-wall carbon nanotubes and C_{60} peapods. *New Journal Of Physics* **5**, 156 (2003).

[95] Hertz, H. Über einen Einfluss des ultravioletten Lichtes auf die electrische Entladung. *Annalen der Physik* **17**, 983 (1887).

[96] Einstein, A. Über einen die Erzeugung und Verwandlung des Lichtes betreffenden heuristischen Gesichtspunkt. *Annalen der Physik* **17**, 132 (1905).

[97] Berglund, C. N. & Spicer, W. E. Photoemission Studies of Copper and Silver: Theory. *Physical Review* **1360**, A1030 and A1044 (1964).

[98] Damascelli, A., Hussain, Z. & Shen, Z. X. Angle-resolved photoemission studies of the cuprate superconductors. *Reviews Of Modern Physics* **75**, 473–541 (2003).

[99] Ibach, H. *Electron Spectroscopy for Surface Analysis*, vol. 4, Topics Curr. Phys. (Springer, Berlin, Heidelberg, 1977).

[100] Hüfner, S. *Springer Series in Solid State Sciences Bd. 82: Photoelectron Spectroscopy* (Springer Verlag, Berlin, 1995).

[101] Kramberger, C. *et al.* Tailoring carbon nanostructures via temperature and laser irradiation. *Chemical Physics Letters* **407**, 254–259 (2005).

[102] Tans, S. J., Devoret, M. H., Groeneveld, R. J. A. & Dekker, C. Electron-electron correlations in carbon nanotubes. *Nature* **394**, 761–764 (1998).

[103] Voit, J. A brief introduction to Luttinger liquids. *Electronic Properties Of Novel Materials-Molecular Nanostructures* **544**, 309–318 (2000).

[104] Ashcroft, N. & Mermin, N. *Solid State Physics* (Harcourt College Publishers, 1976).

[105] Landau, L. & Lifschitz, E. *Lehrbuch der Theoretischen Physik, Bd. 3* (Akademie-Verlag, Berlin, 1971).

[106] Landau, L. & Lifschitz, E. *Lehrbuch der Theoretischen Physik, Bd. 5* (Akademie-Verlag, Berlin, 1966).

[107] Tomonaga, S. Remarks on Blochs Method of Sound Waves Applied to Many-Fermion Problems. *Progress Of Theoretical Physics* **5**, 544–569 (1950).

[108] Luttinger, J. M. An Exactly Soluble Model of a Many-Fermion System. *Journal of Mathematical Physics* **4**, 1154–& (1963).

[109] Haldane, F. D. M. Luttinger Liquid Theory of One-dimensional Quantum Fluids: Properties of the Luttinger Model and their Extension to the General 1D Interacting Spinless Fermi Gas. *Journal of Physics C - Solid State Physics* **14**, 2585–2609 (1981).

[110] Mattis, D. C. & Lieb, E. H. Exact solution of a many-fermion system and its associated boson field. *Journal of Mathematical Physics* **6**, 304–& (1965).

[111] Voit, J. One-Dimensional Fermi Liquids. *Reports On Progress In Physics* **58**, 977–1116 (1995).

[112] Schönhammer, K. *Electron spectroscopies Applied to Low-Dimensional Materials*, chap. Luttinger Liquids: The Basic Concepts, 501 (Kluwer Academic Publishers, 2000).

[113] Schönhammer, K. The Luttinger liquid concept for interacting electrons in one dimension. *Journal Of Physics - Condensed Matter* **14**, 12783–12791 (2002).

[114] Schönhammer, K. Interacting fermions in one dimension: The Tomonaga-Luttinger model. cond-mat/9710330 v3 (1998).

[115] Schulz, H. J., Cuniberti, G. & Pieri, P. Fermi liquids and Luttinger liquids. *Field Theories For Low-Dimensional Condensed Matter Systems: Spin Systems And Strongly Correlated Electrons* **131**, 9–81 (2000).

[116] Peierls, R. *Quantum Theory of Solids* (Oxford University Press, London, 1955).

[117] Bloch, F. *Helvetia Physica Acta* **7**, 385 (1934).

[118] Giamarchi, T. Umklapp process and resistivity in one-dimensional fermion systems. *Physical Review B* **44**, 2905–2913 (1991).

[119] Castellani, C., Di Castro, C. & Metzner, W. Dimensional crossover from Fermi to Luttinger liquid. *Physical Review Letters* **72**, 316–319 (1994).

[120] Arrigoni, E. Crossover from Luttinger- to Fermi-Liquid Behavior in Strongly Anisotropic Systems in Large Dimensions. *Physical Review Letters* **83**, 128 (1999).

[121] Bechgaard, K. *et al.* Superconductivity in an Organic-Solidsynthesis, Structure, and Conductivity of Bis(Tetramethyltetraselenafulvalenium) Perchlorate, $(\mathrm{TMTSF})_2\mathrm{ClO}_4$. *Journal of the American Chemical Society* **103**, 2440–2442 (1981).

[122] Dardel, B. *et al.* Possible Oservation of a Luttinger-liquid Behavior from Photoemission Spectroscopy of One-dimensional Organic Conductors. *Europhysics Letters* **24**, 687–692 (1993).

[123] Grioni, M. & Voit, J. *Electron spectroscopies Applied to Low-Dimensional Materials*, chap. High resolution photoemission studies of low dimensional systems, 501 (Kluwer Academic Publishers, 2000).

[124] Segovia, P., Purdie, D., Hengsberger, M. & Baer, Y. Observation of spin and charge collective modes in one-dimensional metallic chains. *Nature* **402**, 504–507 (1999).

[125] Losio, R. *et al.* Band splitting for Si(557)-Au: Is it spin-charge separation? *Physical Review Letters* **86**, 4632–4635 (2001).

[126] Claessen, R. *et al.* Spectroscopic signatures of spin-charge separation in the quasi-one-dimensional organic conductor TTF-TCNQ. *Physical Review Letters* **88**, 096402 (2002).

[127] Saito, R., Fujita, M., Dresselhaus, G. & Dresselhaus, M. S. Electronic structure of graphene tubules based on C_{60}. *Physical Review B* **46**, 1804–1811 (1992).

[128] Kane, C., Balents, L. & Fisher, M. P. A. Coulomb interactions and mesoscopic effects in carbon nanotubes. *Physical Review Letters* **79**, 5086–5089 (1997).

[129] Egger, R. & Gogolin, A. O. Effective low-energy theory for correlated carbon nanotubes. *Physical Review Letters* **79**, 5082–5085 (1997).

[130] Egger, R. Luttinger liquid behavior in multiwall carbon nanotubes. *Physical Review Letters* **83**, 5547–5550 (1999).

[131] Komnik, A. & Egger, R. Nonequilibrium Transport for Crossed Luttinger Liquids. *Physical Review Letters* **80**, 2881–2884 (1998).

[132] Egger, R. & Gogolin, A. O. Bulk and Boundary Zero-Bias Anomaly in Multiwall Carbon Nanotubes. *Physical Review Letters* **87**, 066401 (2001).

[133] Suzuki, S. *et al.* Electronic structure at carbon nanotube tips studied by photoemission spectroscopy. *Physical Review B* **6324**, 245418 (2001).

[134] Petaccia, L., Goldoni, A., Lizzit, S. & Larciprete, R. Electronic properties of clean and Li-doped single-walled carbon nanotubes. *Journal of Electron Spectroscopy and Related Phenomena* **144**, 793–797 (2005).

[135] Prince, K. C. *et al.* Core-level photoemission from graphite. *Physical Review B* **62**, 6866–6868 (2000).

[136] Suzuki, S. *et al.* Photoemission spectroscopy of single-walled carbon nanotube bundles. *Journal of Electron Spectroscopy and Related Phenomena* **114**, 225–228 (2001).

[137] Knupfer, M. *et al.* Satellites in the Photoemission Spectra of A_3C_{60} (A = K and Rb). *Physical Review B* **47**, 13944–13947 (1993).

[138] Lander, J. J. Auger Peaks in the Energy Spectra of Secondary Electrons from Various Materials. *Physical Review* **91**, 1382–1387 (1953).

[139] Sawatzky, G. A. Quasiatomic Auger Spectra in Narrow-Band Metals. *Physical Review Letters* **39**, 504–507 (1977).

[140] Brühwiler, P. A., Maxwell, A. J., Nilsson, A., Mårtensson, N. & Gunnarsson, O. Auger and photoelectron study of the Hubbard U in C_{60}, K_3C_{60}, and K_6C_{60}. *Physical Review B* **48**, 18296–18299 (1993).

[141] Chen, P. *et al.* Electronic structure and optical limiting behavior of carbon nanotubes. *Physical Review Letters* **82**, 2548–2551 (1999).

[142] Suzuki, S., Maeda, F., Watanabe, Y. & Ogino, T. Electronic structure of single-walled carbon nanotubes encapsulating potassium. *Physical Review B* **67**, 115418 (2003).

[143] Mele, E. J. & Ritsko, J. J. Fermi-Level Lowering and the Core Exciton Spectrum of Intercalated Graphite. *Physical Review Letters* **43**, 68–71 (1979).

[144] van Veenendaal, M. & Carra, P. Excitons and Resonant Inelastic X-Ray Scattering in Graphite. *Physical Review Letters* **78**, 2839–2842 (1997).

[145] Rosenberg, R. A., Love, P. J. & Rehn, V. Polarization-dependent C(K) near-edge x-ray-absorption fine structure of graphite. *Physical Review B* **33**, 4034–4037 (1986).

[146] Shirley, E. L. Ab Initio Inclusion of Electron-Hole Attraction: Application to X-Ray Absorption and Resonant Inelastic X-Ray Scattering. *Physical Review Letters* **80**, 794–797 (1998).

[147] Kramberger, C. *et al.* Van-Hove Singularities in X-ray Absorption and Photoemission on Single-wall Carbon Nanotubes. submitted to Phys. Rev. Lett.

[148] Pichler, T., Sing, M., Knupfer, M., Golden, M. S. & Fink, J. Potassium intercalated bundles of single-wall carbon nanotubes: electronic structure and optical properties. *Solid State Communications* **109**, 721–726 (1999).

[149] Oelhafen, P., Pfluger, P., Hauser, E. & Güntherodt, H. J. Evidence for an Alkali-like Conduction Band in Alkali Graphite-Intercalation Compounds. *Physical Review Letters* **44**, 197–200 (1980).

[150] Delaney, P., Choi, H. J., Ihm, J., Louie, S. G. & Cohen, M. L. Broken symmetry and pseudogaps in ropes of carbon nanotubes. *Nature* **391**, 466–468 (1998).

[151] Delaney, P., Joon Choi, H., Ihm, J., Louie, S. G. & Cohen, M. L. Broken symmetry and pseudogaps in ropes of carbon nanotubes. *Physical Review B* **60**, 7899–7904 (1999).

[152] Kwon, Y. K., Saito, S. & Tomanek, D. Effect of intertube coupling on the electronic structure of carbon nanotube ropes. *Physical Review B* **58**, 13314–13317 (1998).

[153] Ouyang, M., Huang, J. L., Cheung, C. L. & Lieber, C. M. Energy gaps in ”metallic” single-walled carbon nanotubes. *Science* **292**, 702–705 (2001).

[154] Maarouf, A. A., Kane, C. L. & Mele, E. J. Electronic structure of carbon nanotube ropes. *Physical Review B* **61**, 11156–11165 (2000).

[155] Larciprete, R., Petaccia, L., Lizzit, S. & Goldoni, A. Transition from one-dimensional to three-dimensional behavior induced by lithium doping in single wall carbon nanotubes. *Physical Review B* **71**, 115435 (2005).

[156] Kanbara, T., Iwasa, T., Tsukagoshi, K., Aoyagi, Y. & Iwasa, Y. Gate-induced crossover from unconventional metals to Fermi liquids in multiwalled carbon nanotubes. *Applied Physics Letters* **85**, 6404–6406 (2004).

[157] Que, W. Luttinger parameter g for metallic carbon nanotubes and related systems. *Physical Review B* **66**, 193405 (2002).

[158] Terminello, L. J. *et al.* Unfilled Orbitals Of C_{60} And C_{70} From Carbon K-Shell X-Ray Absorption Fine-Structure. *Chemical Physics Letters* **182**, 491–496 (1991).

[159] Chen, C. T. *et al.* Electronic States and Phases of K_xC_{60} from Photoemission and X-ray absorption Spectroscopy. *Nature* **352**, 603–605 (1991).

[160] Okada, S., Otani, M. & Oshiyama, A. Electron-state control of carbon nanotubes by space and encapsulated fullerenes. *Physical Review B* **67**, 205411 (2003).

[161] Miyake, T. & Saito, S. Electronic Structure of C_{60}-encapsulating Semiconducting Carbon Nanotube. *Solid State Communications* **125**, 201–204 (2003).

[162] Poirier, D. M., Owens, D. W. & Weaver, J. H. Alkali-Metal-Fulleride Phase-Equilibria. *Physical Review B* **51**, 1830–1843 (1995).

[163] Poirier, D. M., Olson, C. G. & Weaver, J. H. Electronic States and Stability of the Insulation RbC_{60} Dimer Phase. *Physical Review B* **52**, 11662–11664 (1995).

List of publications

Journal papers

1. Simon, F., Kuzmany, H., **Rauf, H.**, Pichler, T., Bernardi, J., Peterlik, H., Korecz, L., Fulop, F., and Janossy, A.
   Low temperature fullerene encapsulation in single wall carbon nanotubes: synthesis of N@C_{60}@SWCNT
   Chemical Physics Letters **383**, 362 (2004)
2. **Rauf, H.**, Pichler, T., Knupfer, M., Fink, J., and Kataura, H.
   Transition from a Tomonaga-Luttinger liquid to a Fermi liquid in potassium-intercalated bundles of single-wall carbon nanotubes
   Physical Review Letters **93**, 096805 (2004)
3. Shiozawa, H., **Rauf, H.**, Pichler, T., Grimm, D., Liu, X., Knupfer, M., Kalbac, M., Yang, S., Dunsch, L., Buchner, B., and Batchelor, D.
   Electronic structure of the trimetal nitride fullerene Dy_3N@C_{80}
   Physical Review B **72**, 195409 (2005)
4. **Rauf, H.**, Shiozawa, H., Pichler, T., Knupfer, M., Buchner, B., and Kataura, H.
   Influence of the C_{60} filling on the nature of the metallic ground state in intercalated peapods
   Physical Review B **72**, 245411 (2005)
5. Pichler, T., **Rauf, H.**, Knupfer, M., Fink, J., and Kataura, H.
   A photoemission study of the nature of the metallic state in single wall carbon nanotube bundles at low potassium doping
   Synthetic Metals **153**, 333 (2005)
6. Shiozawa, H., **Rauf, H.**, Pichler, T., Knupfer, M., Kalbac, M., Yang, S., Dunsch, L., Buechner, B., Batchelor, D., and Kataura, H.
   Filling factor and electronic structure of Dy_3N@C_{80} filled single-wall carbon nanotubes studied by photoemission spectroscopy
   Physical Review B **73**, 205411 (2006)
7. **Rauf, H.**, Shiozawa, H., Pichler, T., Knupfer, M., Buchner, B., and Kataura, H.
   A photoemission study of the metallic ground state of potassium-doped C_{60} peapods
   Physica Status Solidi B **243**, 3013 (2006)

8. Shiozawa, H., **Rauf, H.**, Grimm, D., Knupfer, M., Kalbac, M., Yang, S., Dunsch, L., Buchner, B., and Pichler, T.
   Charge distribution of potassium intercalated $Dy_3N@C_{80}$ observed with core-level and valence-band photoemission
   Physica Status Solidi B **243**, 3004 (2006)

9. **Rauf, H.**, Pichler, T., Pfeiffer, R., Simon, F., Kuzmany, H., and Popov, V.N.
   Detailed analysis of the Raman response of n-doped double-wall carbon nanotubes
   Physical Review B **74**, 235419 (2006)

10. Kramberger, C., **Rauf, H.**, Shiozawa, H., Pichler, T., Knupfer, M., Büchner, B., Batchelor, D., and Kataura, H.
    Van-Hove Singularities in X-ray Absorption and Photoemission on Single-wall Carbon Nanotubes
    Submitted to Physical Review Letters

Conference proceedings

1. **Rauf, H.**, Pichler, T., Simon, F., and Kuzmany, H.
   A Raman Study of Potassium-Doped Double-wall Carbon Nanotubes
   19th International Winterschool and Euroconference on Electronic Properties of Novel Materials 2004, AIP conference Proceedings **723**, 213 (2004).

2. Pichler, T., **Rauf, H.**, Knupfer, M., Fink, J., and Kataura, H.
   A Photoemission Study of Potassium-Doped Single-wall Carbon Nanotubes
   19th International Winterschool and Euroconference on Electronic Properties of Novel Materials 2004, AIP conference Proceedings **723**, 217 (2004).

3. Pichler, T., Shiozawa, H., **Rauf, H.**, Knupfer, M., Fink, J., Büchner, B., and Kataura, H.
   A Photoemission Study of Potassium-Doped C_{60} peapods
   20th International Winterschool/Euroconference on Electronic Properties of Novel Materials 2005, AIP conference Proceedings **786**, 281 (2005)

4. Shiozawa, H., **Rauf, H.**, Pichler, T., Knupfer, M., Kalbac, M., Yang, S., Dunsch, L., Büchner, B., Batchelor, D., and Kataura, H.
   Effective valency of Dy ions in $Dy_3N@C_{80}$ metallofullerenes and peapods
   20th International Winterschool/Euroconference on Electronic Properties of Novel Materials 2005, AIP conference Proceedings **786**, 325 (2005)

Acknowledgement

It is a pleasure for me to thank all the people who supported me during the time of my dissertation and who contributed to the completion of this work.

First of all, I am grateful to Prof. Bernd Büchner for giving me the opportunity to carry out this thesis and the related work at his institute.

Special thanks go to my immediate supervisor, Dr. Thomas Pichler, for first arousing my interest in the world of nanotubes and then spending endless amounts of time measuring and discussing them with me.

Furthermore, I would like to thank all the colleagues and friends at the IFW and the spectroscopy group. Dr. Martin Knupfer always had an open ear for my questions. I also thank all the former and present "nanotube people": Dr. Hide Shiozawa, Dr. Xianje Liu, Dr. Ewa Borowiak-Palen, Dr. Mark Hermann Ruemmeli, Dr. Alexander Grüneis, Christian Kramberger, Paola Ayala, and Daniel Grimm, with whom discussing on and off topic has always been a great pleasure. I also greatly appreciated the technical assistance given by Kerstin Müller, Stefan Leger, Ronny Schönfelder and especially Dr. Roland Hübel.

I thank Prof. Hiromichi Kataura from the AIST, Japan for providing excellent SWCNT samples.

I also thank Brendan Bleheen for his assistance with the English language, especially for getting me out of the excessive use of passive structures in my sentences.

Last but not least I would like to thank my parents Bernard and Elisabeth for their support throughout the years and also my sister Birte and my brother Jan-Dirk for fuelling my interest in physics by telling me about their law studies.

Die Arbeit "Metallic Ground State of Functionalized Carbon Nanotubes", vorgelegt von Hendrik Rauf, wurde unter Betreuung von Prof. B. Büchner am *Institut für Festkörperforschung* (IFF) des *Instituts für Festkörper- und Wekstoffforschung Dresden e.V.* (IFW Dresden) angefertigt.

Versicherung

Hiermit versichere ich, dass ich die vorliegende Arbeit ohne die unzulässige Hilfe Dritter und ohne Benutzung anderer als der angegebenen Hilfsmittel angefertigt habe, die aus fremden Quellen direkt oder indirekt übernommenen Gedanken sind als solche kenntlich gemacht. Die Arbeit wurde bisher weder im Inland noch im Ausland in gleicher oder ähnlicher Form einer anderen Prüfungsbehörde vorgelegt.

Ich erkenne hiermit die Promotionsordnung der TU Dresden an.